KfK 3939
August 1985

In-Pile Vapor Pressure Measurements on UO_2 and $(U, Pu)O_2$

W. Breitung, K. O. Reil
Institut für Neutronenphysik und Reaktortechnik
Projekt Schneller Brüter

Kernforschungszentrum Karlsruhe

KERNFORSCHUNGSZENTRUM KARLSRUHE
Institut für Neutronenphysik und Reaktortechnik
Projekt Schneller Brüter

KfK 3939

In-Pile Vapor Pressure Measurements on UO_2 and $(U,Pu)O_2$

W. Breitung
K.O. Reil[+]

[+] Sandia National Laboratories
Advanced Reactor Research Department 6420
Albuquerque, New Mexico, 87185, USA

Kernforschungszentrum Karlsruhe GmbH, Karlsruhe

Kernforschungszentrum Karlsruhe GmbH
ISSN 0303-4003

In-pile vapor pressure measurements on UO_2 and $(U,Pu)O_2$

Abstract

The Effective-Equation-of-State (EEOS) experiments investigated the saturation vapor pressures (p_{sat}) of ultra pure UO_2, reactor grade UO_2, and reactor grade $(U_{.77}\ Pu_{.23})O_2$ using newly developed in-pile heating techniques. Emphasis was put on the precise determination of the fuel enthalpy ($\pm$ 3%) and avoidance of sample contamination, e.g. from adsorbed water vapor. For enthalpies between 2150 and 3700 kJ/kg (about 4700 to 8500 K) vapor pressures from 1.3 to 54 MPa were measured. The p_{sat}-h curves of all three fuel types were identical within the experimental uncertainties. An assessment of all published p_{sat}-h measurements showed that the p-h saturation curve of UO_2 appears now well established by the EEOS and the CEA in-pile data. Using an estimate for the heat capacity of liquid UO_2, the in-pile results were also compared to earlier p_{sat}-T measurements. The assessments lead to proposal of the following relations:

$$\log(p_{sat}/MPa) = 23.7989(+.1505)-29605.5\ K/T-4.75783\cdot\log(T/K) \qquad (I)$$

$$(h-h_{298})/(kJ/kg) = -221.15 + .5533\ T/K - 1.0945\cdot10^{-5}(T/K)^2 \qquad (II)$$

Relation I, which includes a factor-of-2 uncertainty band, covers all p_{sat}-T equilibrium evaporation measurements. Relation I yields 3817 K for the normal boiling point, 415.4 kJ/mol for the corresponding heat of vaporization, and 1.90 MPa for the vapor pressure at 5000 K. Relations I and II, which represent a parametric form of the p_{sat}-h curve (T = parameter), also give a good description of the EEOS and CEA in-pile data. Thus the proposed equations allow a consistent representation of both p_{sat}-T and p_{sat}-h measurements, they are sufficiently precise for CDA analyses and cover the whole range of interest (3120-8500 K, 1400-3700 kJ/kg). Relations I and II are also proposed for typical LMFBR (U,Pu) mixed oxides.

In-pile Dampfdruckmessungen an UO_2 and $(U,Pu)O_2$

Zusammenfassung

Die Effektive Equation-of-State (EEOS) Experimente untersuchten den Sättigungsdampfdruck (p_{sat}) von hochreinem UO_2, reaktortypischem UO_2 und reaktortypischem $(U_{.77}Pu_{.23})O_2$ mittels neu entwickelter in-pile Techniken. Besonderer Wert wurde auf eine genaue Bestimmung der Brennstoffenthalpie ($\pm 3\%$) und die Vermeidung von Probenkontamination, z.B. durch adsorbierten Wasserdampf, gelegt.

Für Enthalpien zwischen 2150 und 3700 kJ/kg (etwa 4700 bis 8500 K) wurden Dampfdrücke von 1.3 bis 54 MPa gemessen. Die p_{sat}-Kurven aller drei Brennstoffe waren identisch innerhalb der Meßgenauigkeiten. Eine Bewertung aller veröffentlichten p_{sat}-h-Messungen zeigte, daß die p-h-Sättigungskurve nun durch die EEOS und CEA in-pile Daten recht genau festliegt. Mittels einer Abschätzung für die Wärmekapazität von flüssigem UO_2 wurden die in-pile Resultate auch mit früheren p_{sat}-T-Messungen verglichen. Die Bewertungen führten zu folgenden Vorschlägen:

$$\log(p_{sat}/MPa) = 23.7989(+.1505)-29605.5\ K/T-4.75783\cdot\log(T/K) \qquad (I)$$

$$(h-h_{298})/(kJ/kg) = -221.15 + .5533\ T/K - 1.0945\cdot10^{-5}\cdot(T/K)^2 \qquad (II)$$

Gleichung I, die ein Faktor-2-Unsicherheitsband enthält, deckt alle p_{sat}-T-Gleichgewichtsverdampfungsexperimente ab. Gleichung I ergibt 3817 K für den Siedepunkt, 415.4 kJ/mol für die entsprechende Verdampfungswärme und 1.90 MPa für den Dampfdruck bei 5000 K. Gleichungen I und II, die eine parametrische Form der p_{sat}-h-Kurve darstellen (T = Parameter), beschreiben auch die EEOS und CEA in-pile Daten recht gut. Die vorgeschlagenen Gleichungen erlauben somit eine konsistente Beschreibung von p_{sat}-T- und p_{sat}-h-Messungen, sie sind hinreichend genau für CDA-Analysen und decken den gesamten interessierenden Bereich ab (3120-8500 K, 1400-3700 kJ/kg). Gleichungen I und II werden ebenso für typische LMFBR (U,Pu)-Mischoxide vorgeschlagen.

CONTENTS

I. THE RESEARCH GOAL

I.1 EOS Data Required for CDA Calculations

Much attention has been given in LMFBR safety research to detailed mechanistic calculations of Core Disruptive Accidents (CDA's). The result of main interest is the mechanical energy release - ofter termed excursion yield - which is defined as the mechanical work done on the pressure vessel. This mechanical work results from the motion of hot core materials, which in turn depends on Equation of-State (EOS) data of core constituents.

In CDA calculations basically two types of mesh cell situations are encountered (Fig. I.1):

1. The mesh cell is completely filled with liquids.
2. The mesh cell contains free volume which can be filled with vapor.

In the first case, the pressure in the cell is dominated by the most compressible fluid present, which is normally sodium. Any pressure from expanding liquid fuel is largely relieved by compressing the sodium in the cell. Thus the pressure determining material data for liquid filled cells are

a) the thermal expansion coefficient of the fuel $\alpha=1/v\cdot(\partial v/\partial T)$ which determines the sodium volume decrease, and
b) the sodium compressibility $\beta=-1/v\cdot(\partial v/\partial P)$ which links the volume decrease with the corresponding pressure increase.

Liquid phase pressures of the fuel have virtually no influence on calculated excursion yields /I.1/.

In the case of a liquid/vapor mixed phase mesh cell, the prevailing fuel vapor pressure in the free cell volume can be saturated or undersaturated, depending on the vaporization kinetics. Refling,

et al. /I.2/ showed that the maximum possible evaporation rate is almost always one to two orders of magnitude larger than the net evaporation rate encountered during the core expansion. It is therefore justified to assume thermodynamic equilibrium between liquid fuel and fuel vapor. Thus it is the fuel saturation vapor pressure which determines the pressure in a vapor/liquid mesh cell. The vapor pressures of sodium or stainless steel can generally be neglected during the expansion phase because the time for significant energy transfer from the heated fuel is too small.

So, the most important material data for core disassembly and expansion calculations are:
- the sodium compressibility (1000 - 1500 K),
- the thermal expansion coefficient of liquid fuel (3000 - 6000 K), and
- the saturation vapor pressure of the fuel (3000 - 6000 K).

Whereas the sodium compressibility is quite well known, a need exists for the liquid fuel data.

Fuel vapor pressure data are further required for the interpretation and analysis of many nuclear safety experiments in which liquid fuel is generated, e.g. the transient heating experiments on single pins underway in the CABRI reactor at Caderache, France.

I.2 Required Measurement Precision

The necessary effort to be put in an experimental program depends strongly on the required precision of the measured data. Since, only intuitive feelings about the required vapor pressure precision existed - often a factor of two - a quantitative estimate was attempted /I.3/.

The quantity of main interest in core disassembly calculations is the excursion yield Y . Uncertainties in the calculated yield arise from the uncertainty in the vapor pressure as well as from other accident variables like reactivity ramp rate ζ, Doppler coefficient D, etc. The total yield uncertainty δY can be written as:

$$\delta Y = \frac{\partial Y}{\partial p_{sat}} \cdot \delta p_{sat} + \frac{\partial Y}{\partial \zeta} \delta \zeta + \frac{\partial Y}{\partial D} \cdot \delta D + \ldots \text{ terms from other variables} \qquad (I.1)$$

Sensitivity studies show that the dominant term in Eq.(I.1) is that from the ramp rate uncertainty $\delta\zeta$ /I.4,5/. Obviously, the term from vapor pressure uncertainties should be some fraction "a" of this dominant term:

$$\frac{\partial Y}{\partial p_{sat}} \cdot \delta p_{sat} = a \frac{\partial Y}{\partial \zeta} \cdot \delta\zeta \qquad (I.2)$$

Choosing a = .5 and evaluating the partial differentials from existing sensitivity studies on calculated excursion yields /I.1,4-9/ leads to the conclusion that the fuel vapor pressure should be known within a factor of 2 to 4, depending on how well the ramp rate of the considered accident is known. Due to the exponential relationship between pressure and energy the acceptable pressure uncertainties translate into very small acceptable uncertainties in energy. Table I.1 summarizes the acceptable uncertainties.

Table I.1: Acceptable Uncertainties In Pressure-Energy Measurements

Precision level	I	II
Ramp rate uncertainty range ζ/ζ_o	.66 to 1.5	.83 to 1.2
Acceptable pressure uncertainty factor p/p_o	4	2
acceptable energy uncertainty	$\pm$ .06	$\pm$.03

Table I.1 shows that vapor pressure measurements on nuclear fuels must have a very precise energy determination in order to be useful for CDA yield calculations. An energy uncertainty close to $\pm$ 3% should be the goal for EOS measurements.

I.3 Selection of Heating Method

When comparing the different feasible heating methods for nuclear fuels, namely laser, electron beam, and nuclear heating, it appears that in-pile fission heating provides the most promising approach to the determination of p-h relations of nuclear fuels. The reasons are twofold:

- Heating method and heating time are CDA typical. Questions about the applicability of the results to reactor accident analysis - like in laser heating methods- do not exist. Futhermore, unknown or not well understood pressure phenomena will be included empirically in the measurements.

- The technique can be extended in a relatively easy way to irradiated (U,Pu) mixed-oxide, which is the fuel of ultimate interest for CDA analyses.

Examples for unclear pressure phenomena are release kinetics of non-fuel species like fission gases, and the pressure interaction between fuel vapor species and non-fuel vapor species.

In-pile EOS experiments appear therefore as the most direct and reliable way to the desired p-h information on nuclear fuels.

LIQUID PHASE CELL

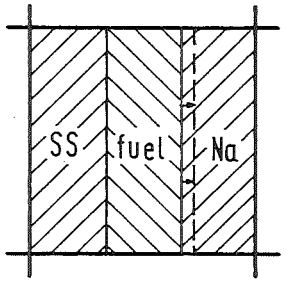

fuel expansion $\alpha = \frac{1}{V}\left(\frac{\delta V}{\delta T}\right)$

sodium compression $\beta = \frac{1}{V}\left(\frac{\delta V}{\delta P}\right)$

LIQUID / VAPOR PHASE CELL

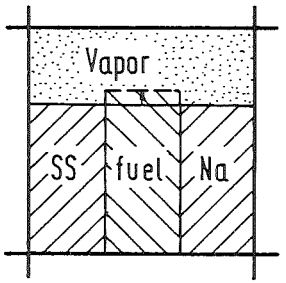

fuel saturation

vapor pressure

p_{sat}

FIGURE I.1 Material Data Important for the Calculation of Mesh Cell Pressures in the Disassembly Phase of CDA's.

II. EEOS EXPERIMENT TECHNIQUE

II.1. Experiment Concept

The basic concept used in the EEOS experiments was developed in the first Equation-of-State series done at Sandia National Laboratories /II.1/. A fuel sample, contained in a closed volume, is fission heated during a reactor power excursion to melt and partially vaporize the fuel. The pressure history p(t) in the pressure cell is measured dynamically during the transient. The time dependent enthalpy h(t) is derived from an in-pile calorimeter and associated calculations. The correlation of p(t) with h(t) yields the section of the p(h)-curve in the respective energy interval, not just a single point on this curve.

The pressure cell assembly, shown in Fig. II.1, is used to measure the transient fuel pressure p(t). The powdered fuel sample fills a volume bounded by a zircalloy crucible and a zircalloy piston. The force acting on the crucible is coupled to the diaphragm of the pressure transducer via an aluminum adapter.

The calorimeter (Fig. II.2),which contains a sample of the same test fuel, provides an absolute and independent measurement of the fuel energy deposition. The calorimeter body is instrumented with one central and four circumferential thermocouples. The measured calorimeter energy is used in the evaluation of the energy deposition into the pressure cell fuel. Differences in neutron flux incident on pressure cell and calorimeter fuel are accounted for by a fission product inventory analysis after the ACRR irradiation (Section II.5).

Due to the intense neutron and gamma fields during a reactor pulse, radiation noise is induced on pressure and temperature signals. These noise signals were accounted for by irradiating each EEOS assembly twice: first without, then with fuel.

II.2 Hardware Design

The hardware in each EEOS experiment consists of three major components:

1. the pressure cell assembly (Figure II.1),
2. the calorimeter assembly (Figure II.2), and
3. the containment and filter structure (Figure II.3).

II.2.1 Pressure cell

The two basic requirements for a meaningfull transient measurement of saturation vapor pressures are sufficiently short response time of the pressure sensor and pressure equilibrium in the test volume.

The pressure transducer used in the EEOS experiments (KAMAN Model KP-1911) has a response time of 25 microseconds. A theoretical study of the transducer response (Section III.1) showed that the coupling of the aluminum adapter and the zircalloy crucible to the membrane does not lengthen the response time noticeably. The pressure measuring system is therefore adequate for resolving pressure excursions which last several milliseconds.

With respect to pressure equilibrium in the measuring volume, hydrodynamic calculations /II.2/ showed that pressure gradients decay very fast compared to the pressure excursion time, and that therefore, a uniform pressure should exist throughout the test volume at any given time[+)]. This pressure should be equal to the equilibrium vapor pressure of the fuel section with the highest internal energy.

The pressure cell design shown in Figure II.1 is the result of an extensive in-pile testing and evaluation program. The main design features are as follows:

[+)] The speed of sound in liquid UO_2 is of the order of 1mm/μs. The fuel sample volume is 2.3 mm thick with a diameter of 10.3 mm.

The pressure generated during a reactor transient acts on the zircalloy crucible which in turn pushes the aluminum adapter upwards against the pressure transducer membrane. By means of a central circular protrusion the adapter loads a precisely defined area of the transducer membrane. The same adapter is used for the calibration of the transducer in a hydraulic press.

The piston and the inner crucible walls are slightly tapered (not shown in Fig. II.1). By this means, the gap thickness between piston and crucible can be zero if there is no fuel powder left on the crucible walls. If there should be some adhered fuel powder, crucible and piston cannot jam (as has been found to happen with a cylindrical piston) since they move slightly away from each other during the pressure measurement. The gap increase due to the movement of the transducer membrane is less than .01 mm, because of the steep tapering angle (3.6 degrees).

The piston-crucible gap is oriented away from the pressure transducer in order to protect the transducer membrane from hot gases which might escape from the crucible. It was found that temperature gradients across the transducer membrane can seriously distort the pressure signal by causing membrane buckling.

The aluminum shim underneath the crucible is manufactured specifically for each pressure cell assembly as the last part in order to remove slack in the system from fabrication tolerances. This also minimizes the free space in the pressure vessel where liquid fuel could escape to during an experiment.

The cadmium filter flattens the energy deposition profiles in the test fuel significantly by shadowing the hot corners of the cylindrical sample. Height and thickness of the cadmium filter was chosen such that the peak-to-average ratio of the fission energy deposition in the sample is minimized (Section III.3).

The pressure cell contained about 1 g of powdered fuel. The fuel density was close to 50% of the theoretical density, which is typical for the fuel smear density in a voided LMFBR core.

II.2.2 Calorimeter

The first in-pile equation-of-state measurements on nuclear fuels were published in 1977 /II.1/. From the refined computer analysis of these experiments /II.3/, it became clear that the determination of the energy deposition into the test fuel is the crucial step in obtaining precise pressure-energy data. Since a factor of two is roughly the precision which is desired for the fuel vapor pressure in CDA codes (Section I.2), the energy deposition in EOS experiments should be determined within $\pm$ 3%. Due to the complex phenomena involved, there is little hope that this level of accuracy can be obtained by computer analysis of experimental raw data. Therefore, an in-pile calorimeter was designed for an absolute and high-precision measurement of the energy deposition into the EEOS test fuel.

The calorimeter consists of the fuel containing calorimeter body, which is attached with a ceramic insulator rod to the vessel lid. The guide pins allow evacuation of the calorimeter in a vacuum system in an open configuration and closing in situ. (Section IV.2). The main design features of the calorimeter assembly are as follows:

- calorimeter body
  - high strength aluminum (Alloy 5086)
  - maximum design pressure 80 MPa
  - proof-tested in hydrostatic facility
- masses
  - calorimeter body 5g
  - test fuel powder .5g
- fuel energy deposition up to 3000 kJ/kg
- temperature increase of Al body up to 500 K
- thermocouples on Al body:

  - one central, .25 mm diameter
  - four circumferential, .12 mm diameter
  - all sheathed, ungrounded junction
  - installed along approximate isotherms to minimize quenching of body by TC leads
- vacuum environment for Al body, below 10^{-3} Pa initially
- cadmium filter
  - .2mm thick
  - extended axially to shield complete fuel sample.

The principle of the energy deposition measurement using the calorimeter, the uncertainties in the energy measurement and the calorimeter test program were described earlier in a seperate report /II.4/.

II.2.3 Containment

The calorimeter and the pressure cell are installed in two independent completely sealed radiological canisters (Fig. II.3). Both canisters were overpressurized to .2 MPa He and leak tested. On the outside of each canister polyethylene moderator can be attached for partial or full thermalization of the ACRR neutron flux. A lead shield consisting of six rings, 37 mm thick, surrounded the containment in order to reduce the gamma heating of the calorimeter body. With the lead rings installed, the gamma heating of the calorimeter could be reduced to about 10% of the fission heating. Space and reactivity considerations prohibited the use of a thicker lead shield. The instrumentation signals are passed out of the primary and secondary containment canisters via hermetically sealed connectors.

II.3 Data Acquisition

On-line signals from the following instrumentation were recorded during an experiment:

- pressure transducer voltage
- two fission chambers currents from
  - in-core position, and
  - reactor pool
- five thermocouple voltages from the calorimeter.

Since the signal height as well as the time scale of interest varied by orders of magnitude during the experiment, some of the signals were multiplexed, amplified with different gains and/or sampled with different frequencies. A total of 18 data channels were recorded in each shot.

A block diagram of the ACRR Data Aquisition System is given in Fig. II.4. As shown, the data may be recorded on FM type recorders (26 channels of data), displayed on a viscorder oscillograph, and digitized by high speed analog to digital converters in the Data Acquisition and Display System (DADS) terminal. The system contains provisions for complete calibration of the instrumentation after loading the test equipment into the core. Pressure transducer electronics, thermocouple reference junctions, and reactor power instrumentation are located at the reactor and are connected to the data acquisition by a permanent cable bus.

The DADS terminal is shown schematically in Figure II.5. The terminal is built around an HP9845 desk top calculator with 449 K bytes of memory. Analog input is via eight high speed ADC channels with a maximum sampling rate of 400 kHz. Each input may be multiplexed 2 or 4 times for sampling rates less than or equal to 40 kHz. Each ADC channel has an associated 32768 word external memory. The calculator may read the external ADC memories, perform limited computation, display the data, store data on a cartridge disc or transmit the data to the central DADS computer. The central DADS computer provides additional computational capability along with digital magnetic tape data storage and a better graphics plotter.

II.4 The ACRR

The Annular Core Research Reactor (ACRR) is a pool-type reactor, using cylindrical BeO-UO_2 fuel elements. The most prominent feature which distinguishes this reactor from many others is the large (23-cm inside diameter), dry irradiation space in the center of the core. The annulus-shaped core is formed by single fuel elements, arranged in a hexagonal grid around the central cavity. The core is located in an open pool 3.0 meters in diameter and 8.5 meters deep. The top of the core is approximately 6 meters below the surface of the pool water, which affords more than adequate radiation shielding. Access to the central irradiation cavity is by a nominally 25-cm diameter loading tube which extends vertically upward from the center of the core. Neutron streaming up to loading tube is prevented by a shield plug which, except for special experiments, is in place during operation of the reactor.

The ACRR fuel section is about 35 mm in diameter by 0.52 mm in length. The fuel is contained in a fluted niobium liner and sealed in an 0.5 mm thick smooth stainless steel cladding. The flutes in the liner maintain helium filled insulating gaps between the fuel and liner, and between the liner and the clad. At the ends of the fuel stack are short BeO reflector-insulators followed by the end pieces. The overall length of the fuel element is 0.74 m.

The operational characteristics for pulse and steady-state mode are summerized in Table II.1. Most important for the EEOS experiments is the large pulse fluence which allows filtering of neutrons to obtain very flat energy deposition profiles.

Table II.2 gives an idea about the absolute energy deposition capabilities in the ACRR.

Table II.1 ACRR Central Cavity Radiation Levels for Routine Maximum Operations (at Cavity Horizontal and Vertical Centerline) /II.5/

Steady-State Operation

Power		2.0 MW
Neutron Flux	(>3 MeV)	2.0×10^{12} n/cm^2/sec
	(>10 keV)	2.4×10^{13} n/cm^2/sec
	(total)	4.1×10^{13} n/cm^2/sec
Gamma Dose Rate		2.2×10^{4} rad/sec

Pulse Operation

Reactivity		3.00
Energy Yield		310 MJ
Neutron Fluence	(>3 MeV)	3.1×10^{14} n/cm^2
	(>10 keV)	3.7×10^{15} n/cm^2
	(total)	6.4×10^{15} n/cm^2
Gamma Dose		3.4×10^{6} rad

Table II.2 Calculated ACRR Core Capabilities for Single Pins

Fuel Enrichment	Poly Thickness (inch)	Released Reactor Energy (MJ)	Energy Deposited in Test Pin (J/g)
A. Configurations to achieve 3000 J/g:			
12%	1/4"	300	3000
12%	3/4"	175	3000
B. Maximum Energy Deposition:			
20%	3/4"	300	6850
93%	3/4"	300	16000

The data in Table II.2 were essentially confirmed in the EEOS experiments, for instance experiment EEOS-05 had the following neutronic configuration:

- 15% fuel enrichment
- 3/8 inch poly
- 300 MJ reactor energy release
- 3700 J/g total energy deposition in the test fuel.

II.5 Data Evaluation

The data evaluation scheme of EEOS experiments is outlined in Fig. II.6. The data evaluation consists of three steps:

1. on-line data aquisition,
2. fission product inventory analysis of pressure cell and calorimeter, and
3. numerical data analysis, using codes described in Section V.

To measure the radiation noise signals on pressure transducer voltage, fission chamber current, and calorimeter temperatures, the on-line data aquisition is first performed for a background experiment which contains no fuel. Then the same data are recorded for a fueled experiment.

After unloading the fueled pressure cell and calorimeter from the containments (Fig. II.3), the fission product inventory in both cells is measured in a gamma counting facility, using the 1.6 MeV line of the fission product La-140. This analysis, which is described in more detail in Section III.5, yields the ratio in the number of fission events in both cells.

The third step in data evaluation comprises two parts: determination of pressure and determination of energy.

The time dependent net pressure is simply the difference of the pressure transducer readings with and without fuel, including a correction in the time scales to synchronize the reactor pulses. The energy evaluation starts with calculation of the total net fission energy deposition into the calorimeter fuel, using the measured thermocouple traces of background and experiment shot. Multiplication of this total (time integrated) energy with the ratio of fissions, gives the absolute total fission energy deposition into the pressure cell fuel. From this total value, the time dependent energy deposition of the pressure cell fuel is derived using the fission chamber signal i(t). (The relevant equations are given in Section V.) Finally, the correlation of time dependent net pressure with calculated enthalpy yields the desired pressure-enthalpy curve.

It should be emphasized, that the described transient technique results in a continuous measurement of a certain section of the p-h curve, not in just a single point on this curve.

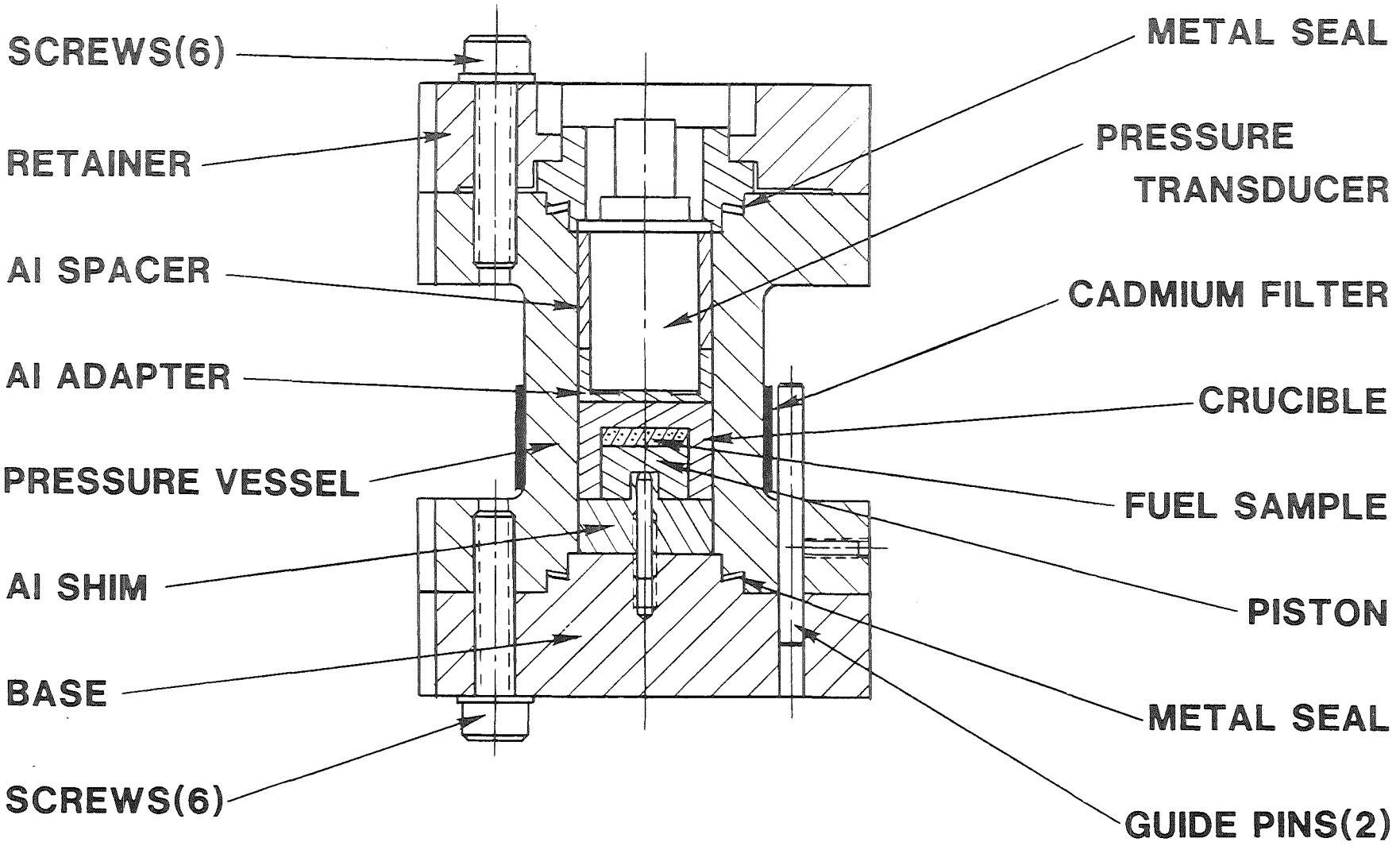

FIGURE II.1 Design of EEOS Pressure Cell

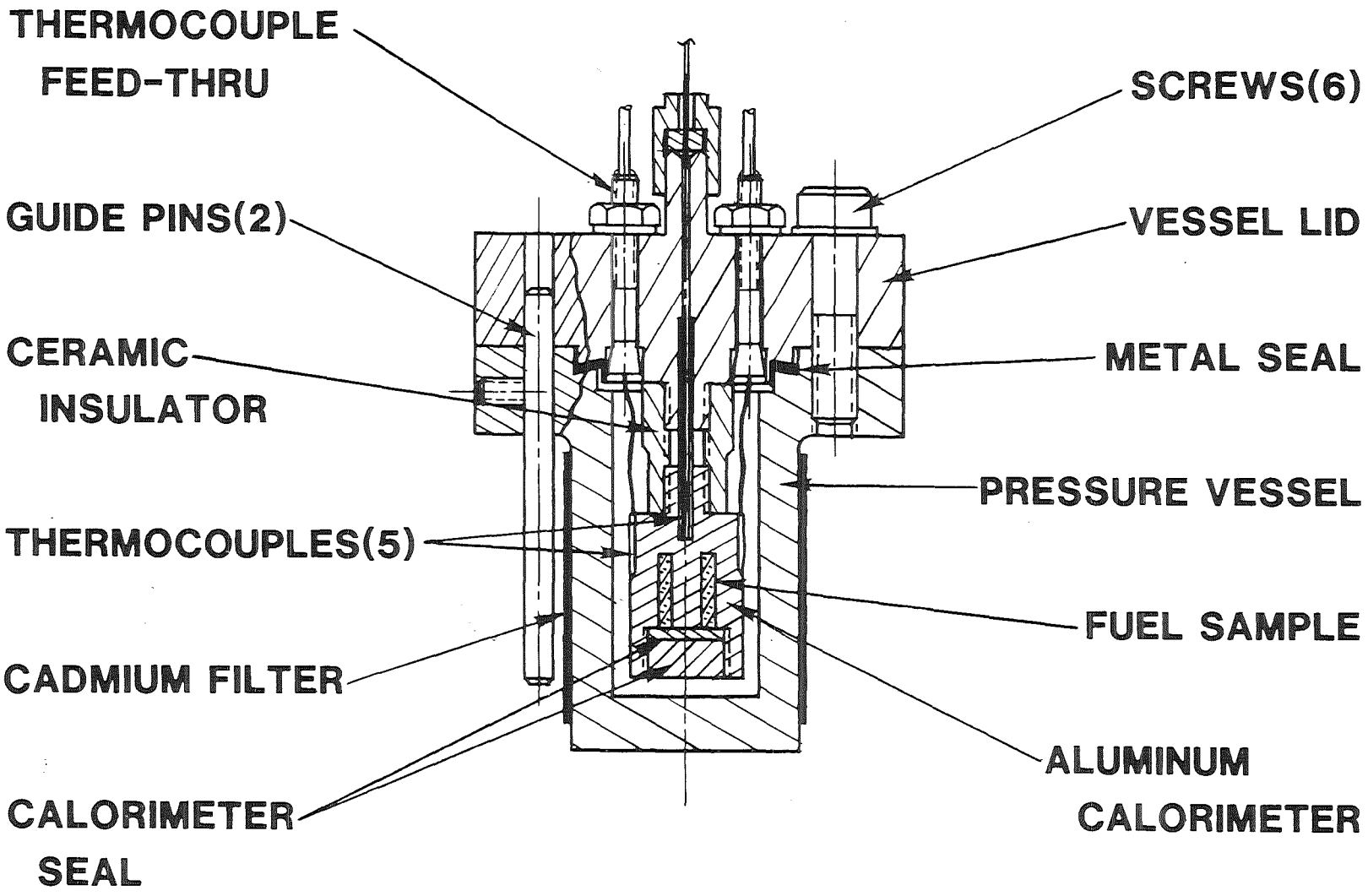

FIGURE II.2 Design of EEOS In-pile Calorimeter

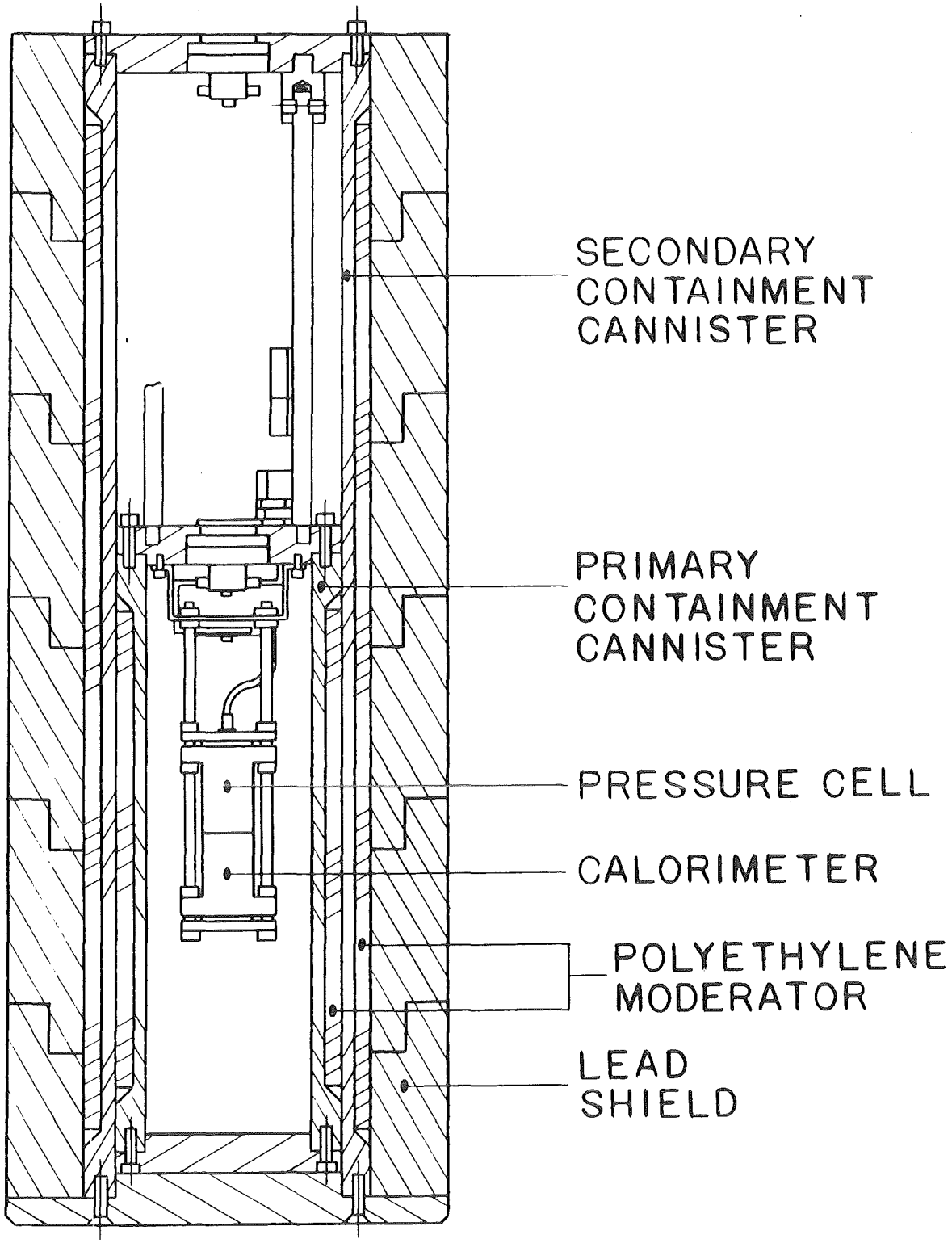

FIGURE II.3 Containment and Filter Structure for EOS Experiments

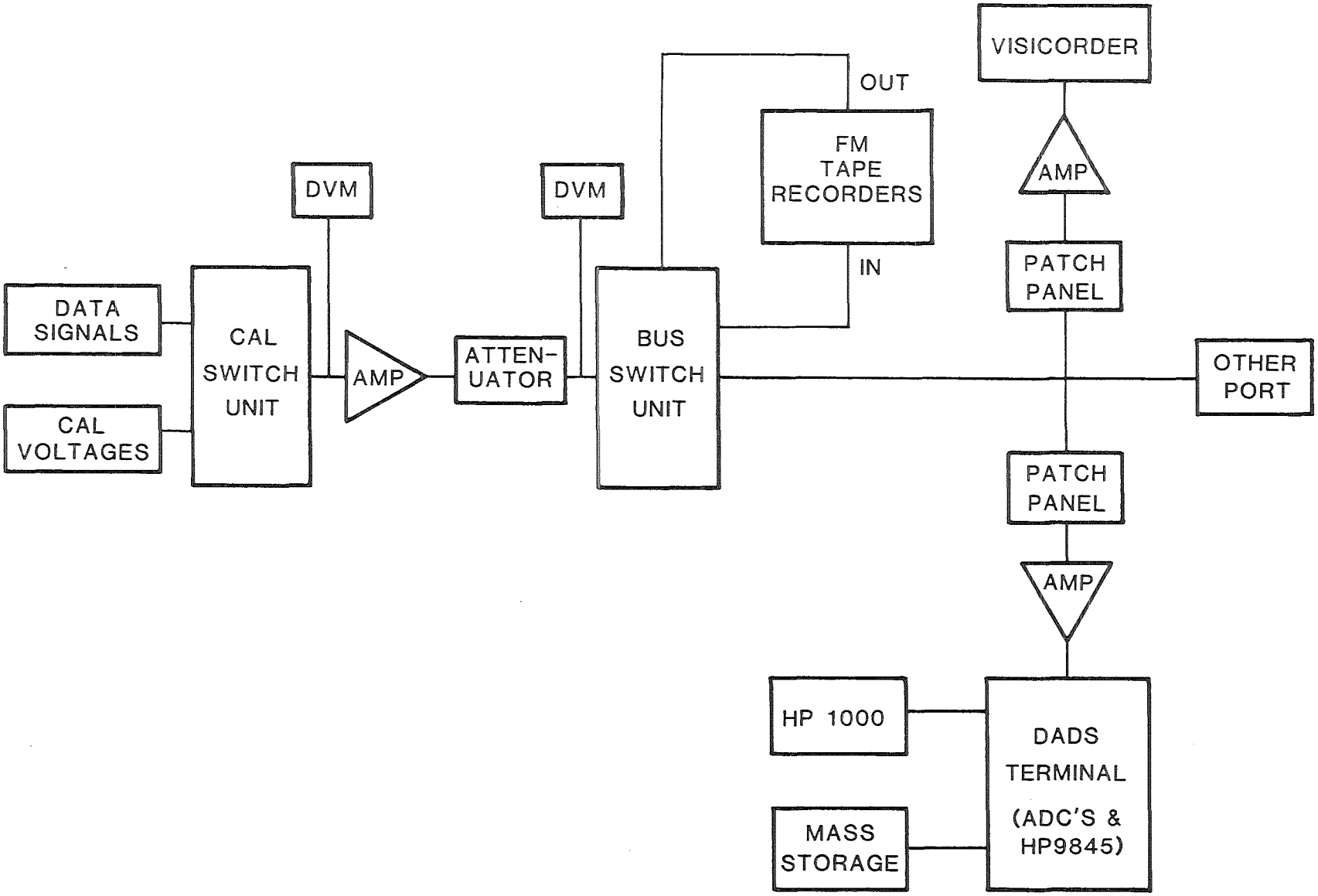

FIGURE II.4 Block Diagram of ACRR Data Aquisition System

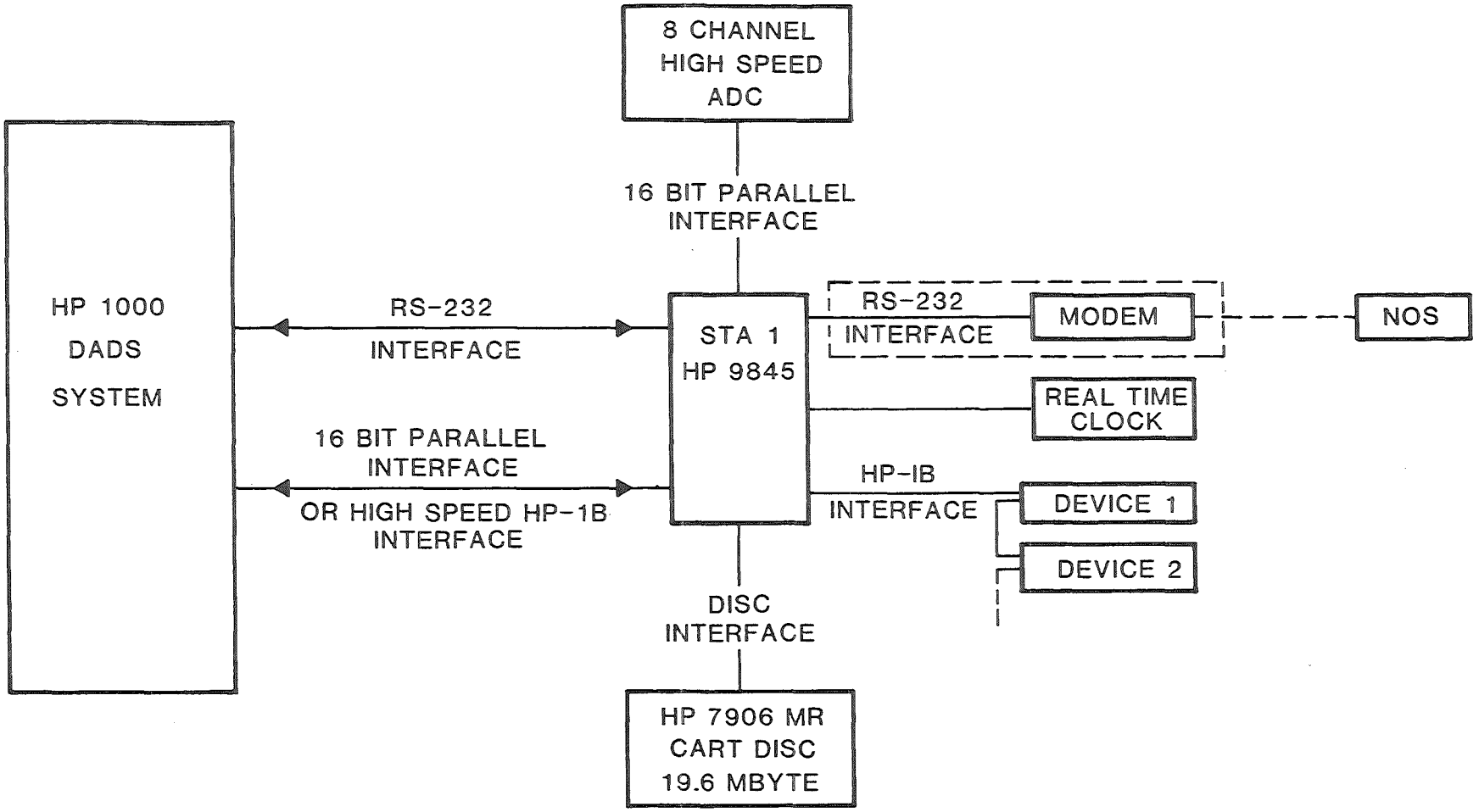

FIGURE II.5 Configuration of DADS Terminal (Items in dashed box were not used in EEOS work)

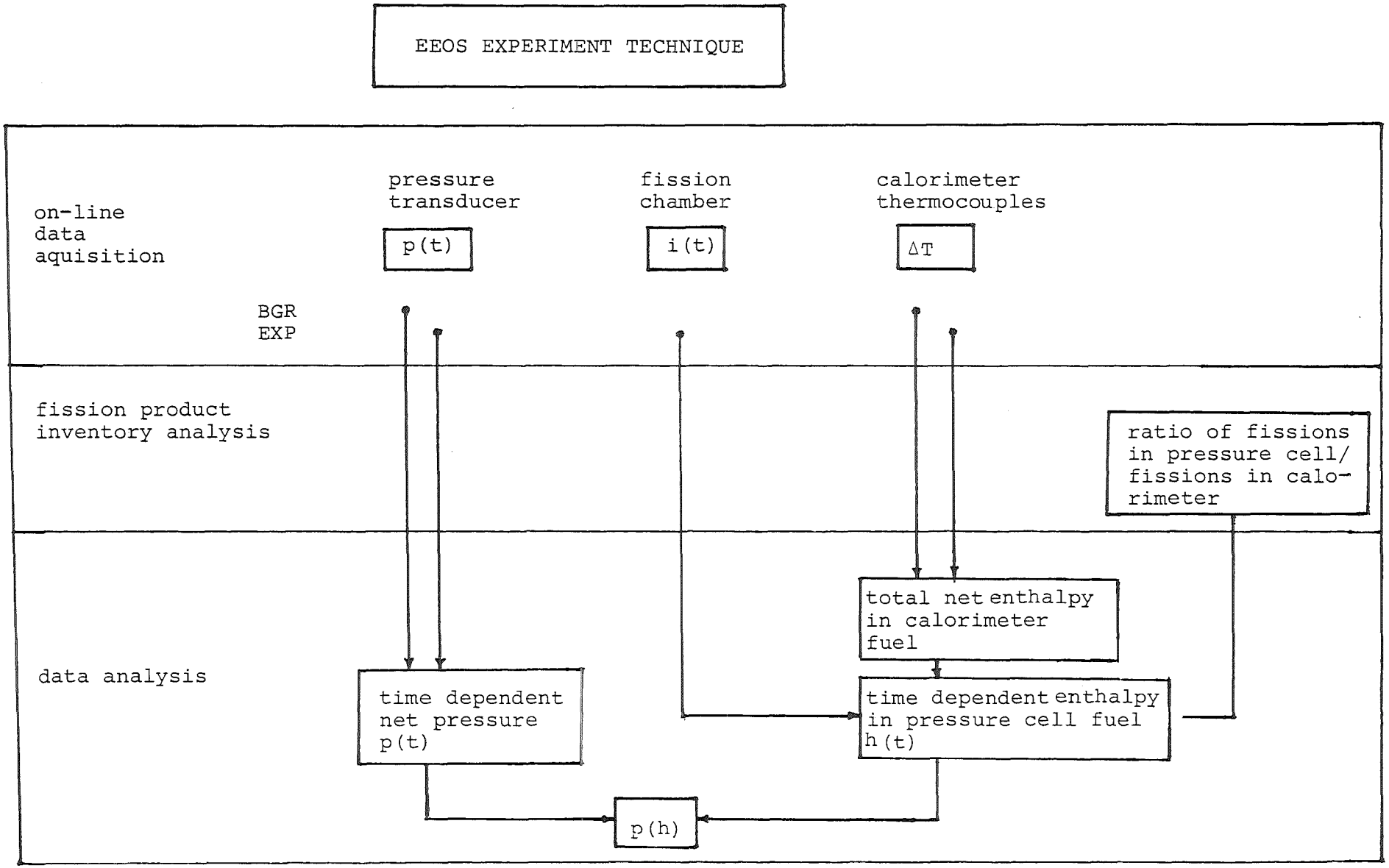

FIGURE II.6 Data Evaluation in the EEOS Technique

III. EVALUATION OF EEOS TECHNIQUE

Chapter II gave a brief outline of the EEOS technique as used in the vapor pressure measurements on liquid reactor fuels. However, there were quite a number of experimental and theoretical investigations necessary to design proper functioning equipment. To document this work, and to demonstrate the presently existing understanding of the physical phenomena involved, this chapter discusses in more detail some important aspects of the EEOS technique.

III.1 Pressure Transducer Dynamics

In the EEOS pressure cell (Fig. II.1) the fuel vapor pressure acts on the pressure transducer by moving the Zr crucible and the Al adapter upwards against the transducer membrane. For proper pressure measurement it must be assured that the coupling of these additional masses to the transducer does not deteriorate the time response of the pressure transducer. A detailed analysis of the dynamic behaviour of the modified transducer was therefore performed /III.1/.

The dynamic response of the modified transducer system was evaluated in three steps:

1. Find the transfer function of the bare pressure transducer from available shock tube data.
2. Construct from this the transfer function of the modified system, including the additional masses.
3. Calculate the dynamic response of the modified system to typical EOS-pressure excursions using the transfer function found in step 2.

III.1.1 Bare Pressure Transducer

The transfer function G of a linear system having lumped and constant parameters is defined as /III.2/:

$$G = \frac{\mathcal{L}\{\text{output}\}}{\mathcal{L}\{\text{input}\}} \qquad \text{(III.1)}$$

where $\mathcal{L}$ is the Laplace operator. For the bare pressure transducer system, input and output signals are known from shock tube experiments /III.3/. Figure III.1 shows the rectangular shock tube pressure and Figure III.2 the response of the 5000 psi-pressure-transducer. In order to calculate G, it is necessary to obtain an analytical fit of the response.

The response closely resembles a damped frequency beat, which results from the superposition of two damped oscillations having slightly different natural frequencies. The Fourier analysis of the output signal shows indeed two dominant peaks at ν_1 = 35.4 kHz and ν_2 = 42.6 kHz (Figure III.3). It should therefore be possible to describe the transducer mathematically by two coupled differential equations of second order. ($M\ddot{x} + B\dot{x} + kx = F(t)$, with x = membrane displacement, M = mass, B = friction constant, k = spring constant, F = force.)

From the exponential decrease of the output signal maxima in Figure III.2 ($\sim e^{-bt}$) the damping factor b can be derived. The smaller transducer amplitudes during the first beat (t = .9 to 1. ms) indicate that the transducer oscillation is not yet fully developed during this first .1 ms, possibly due to the finite rise time of the shock tube signal. Therefore, only the exponential decrease at times greater than 1.0 ms was fitted. Use of b, ν_1 and ν_2 results in the analytical fit function depicted in Figure III.4. Comparison with Figure III.2 shows that this function represents the measured signal quite well for times greater than 1.00 ms. Especially noteworthy is the good agreement of the absolute pressure amplitudes which are not used in finding the fit parameter b. Insertion of this fit function and of the shock tube step function into Equation III.1 yields the required expression for the transfer function G of the bare pressure transducer.

III.1.2 Modified Pressure Transducer

The bare pressure transducer is modified in the EEOS experiments by coupling additional masses to the transducer membrane (about 10 g). The transfer function of this modified system G^+ was found by replacing the oscillating mass in the bare transducer transfer function G by:

$$M^+ = R \cdot M$$

where M = osciallating mass of bare pressure transducer = .6 $\pm$ .2 g
R = ratio of oscillating masses in bare and modified transducer

Due to the uncertainty in M, the oscillating mass ratio of interest for the EEOS experiment design is 5 to 20. In the above approach it is assumed that the modified system is also a linear system of second order ($M^+\ddot{x} + B\dot{x} + kx = F(t)$).

III.1.3 Dynamics of The Modified System

The dynamic response of the modified system $p_{out}(t)$ to a specified input pressure $p_{in}(t)$ was calculated in three steps.

1. Find the Laplace transformation of $p_{in}(t)$

$$P_{in}(s) = \mathcal{L}\{p_{in}(t)\}$$

2. Multiply $P_{in}(s)$ with the transfer function G^+. This yields the Laplace transformation of the response $P_{out}(s)$

$$P_{out}(s) = G^+(s) \cdot P_{in}(s)$$

3. Backtransform $P_{out}(s)$ to find the response $p_{out}(t)$

$$p_{out}(t) = \mathcal{L}^{-1}\{P_{out}(s)\}$$

The reponse of the modified system was calculated for several input pressures, e.g. step function of Fig. III.1 (p(t)=2.45 MPa), an exponential pressure increase typical for the first EEOS-series, and a pressure increase with a 10 times faster characteristic rise time.

Figure III.5 shows as example the calculated response to a 2.45 MPa pressure step (R=10). Comparison with Fig. III.2 shows that adding masses to the transducer membrane has two effects:

- the oscillation frequency decreases, and
- the damping is reduced.

Without an initial pressure step at t=0 only very minor oscillations occur. For the two investigated exponential pressure rises, the calculated response was practically identical with the input pressure. Even for the extremely fast pressure rise, which corresponded to about 20 MPa in 5 ms only minor oscillations occured. This means that the modified system should still have a sufficiently short response time and an adequate damping for resolving the transient pressure in EEOS experiments correctly.

III.2 Pressure Cell Development

The first in-pile test (ACRR Shot 1057) - which used the initial design with upwards moving piston, revealed that liquid fuel extruded from the crucible during the prompt reactor pulse. This caused one-sided heating of the pressure transducer membrane and an early distortion of the pressure signal. Both the magnitude and the frequency of the observed disturbance could be explained by transient heat conduction through the transducer membrane and associated buckling, caused by the different thermal expansion in the membrane. X-ray photographs confirmed that significant amounts of liquid fuel had escaped from the crucible.

As a consequence, the pressure cell design was changed to an inverted crucible (Figure II.1) and the gap between piston and crucible was made as small as possible (about .05 mm). In this geometry, any extruding fuel would be directed away from the temperature sensitive transducer, instead of towards it as in the initial design. However, in the next experiment (ACRR Shot 1227), piston and crucible did not separate. It is believed that some fuel powder adhered to the crucible wall, and when the cell was closed in the UHV-system, a tight fractional bond was created in the narrow gap between crucible and piston.

In order to overcome this problem, the cylindrical piston was replaced by a tapered one. The advantage here is that the gap thickness can be zero indeed, if there is no fuel powder on the crucible walls. If there should be some fuel powder, crucible and piston cannot jam since they move slightly away from each other during the pressure measurement. The gap increase due to the movement of the transducer membrane is less than .01 mm, because of the steep tapering angle (3.6^{o}). Using this design in Shot 1264 resulted in a pressure signal which was free of disturbances and had the expected timing and shape as well.

III.3 Calorimeter Development

The initial calorimeter design was tested in 11 in-pile experiments. The main design improvements involved

a. Reduction of heat losses along the ceramic support rod.
b. The improvement of the calorimeter seal (plug at the bottom of the aluminium body).
c. The addition of a cadmium filter to lower the total energy deposition.
d. Evaluation of gamma heating and thermocouple performance.

The heat losses were reduced by machining the ceramic support rod as thin as possible, without jeopardizing its mechanical strength.

The calorimeter seal failed initially at energy depositions around 2000 kJ/kg UO_2. Metallographic examinations revealed that the metal-metal seal was not gas-tight. Escaping hot fuel vapor could therefor erode the seal, once fuel vapor was generated. By replacing the aluminium plug with a zirconium plug, the sealing torque on the plug could be increased to values which resulted in a gas-tight seal. Such an improved calorimeter body was pressure tested in a hydrostatic facility, where it withstood internal pressures of up to 80 MPa. The addition of a cadmium filter assures that pressures generated in the calorimeter body do not exceed this pressure limit.

Compared to the fission energy deposition, the gamma heating of the calorimeter is a 10 percent effect. Since the goal in the energy measurement is a total uncertainty of $\pm$ 3 percent, gamma-heating must be evaluated carefully. The total gamma heating is composed of a prompt part and a delayed part. The dominant contributors to the prompt gamma heating are the prompt gammas from core fissions. The delayed gamma heating is due to the decay of core fission products. Several experiments were performed in the ACRR to reliably measure prompt and delayed gamma heating of the calorimeter.

The first measurement of the gamma heating of the alumium body (ACRR shot 1088) gave uncertain and conflicting results, with respect to magnitude and ratio of prompt and delayed gamma heating contributions. It was therefore decided to measure the basic response of thermocouples to the ACRR gamma field (Shot 1134). Next, the problem of thermocouples connectors was investigated (Shot 1135). These connectors are mounted in the top lid of the inner and outer canister to bring the thermocouple signals out of the EEOS package. Due to the gamma flux gradients in the ACRR core and due to the non-symmetric gamma heating of the container lids, axial and radial temperature gradients develop in the connectors, leading to spurious thermocouple voltages. (These hermetically sealed

PTO-connectors do not contain thermocouple alloy pins.) The connector effects were investigated by comparing the signals from thermocouples which were installed with and without connectors (ACRR Shots 1135, 1151). Furthermore, an error signal was measured across inner plus outer connector, such that it represents the sum of the spurious signals from inner and outer connectors for the particular connector pins. It was found, however, that this error signal is not representative for all pins in the 18-pin connector, obviously different temperature gradients exist along different connector pins.

The investigations showed, however, that the thermocouple deviations from these spurious signals can be accounted for on the basic of the following findings:

a. The thermocouple deviations from connector effects are consistent from shot to shot.
b. Their magnitude is acceptable during the first 25 seconds (about $\pm$ 1.5 K).
c. The true calorimeter temperature (as measured without connectors) is within $\pm$ 1 K of the mean of all five thermocouples with connectors.

Also, to minimize effects in the upper connector, the lead shielding was extended upwards.

The improved calorimeter performed satisfactorily at 3000 J/g UO_2 energy deposition (ACRR Shots 1227 and 1264) which increased the calorimeter temperature by about 320 K. The temperature readings of the five thermocouples generally agree within $\pm$ 3K, once thermal equilibrium is established between fuel and calorimeter body.

III.4 Energy deposition calculations

The energy analysis program (described in Chapter IV) and the optimization of cadmium filters for the pressure cell, require information about the fission energy distribution within the fuel sample. Such energy deposition calculations for EEOS samples require very good spatial resolution because:

a. The cadmium ring around the fuel sample casts sharp shadows in the neutron flux distribution.
b. Energy deposition differences in the EOS sample are only 5 to 10 percent.
c. There are large dimensional differences between the driving core and the EEOS fuel sample (meters compared to centimeters).

First calculations using a S-16 version of TWOTRAN did not quite reach the desired resolution in energy deposition results /III.4/.

A complementary method was then developed to check and extrend the TWOTRAN results /III.5/. This methods uses the cylindrical neutron source, which is calculated with TWOTRAN for the ACRR cavity, as input. Then it evaluates the distribution of neutron absorptions in the EEOS fuel by integrating over all possible neutron paths through the fuel. Neutron scattering in the fuel is neglected, because in EEOS fuel, fission events are much more probable than scattering events. The calculations result in a detailed two-dimensional r-z energy distribution for the EEOS sample.

The main modelling assumptions of the PATH code are:

- The EEOS fuel geometry is that of a homogeneous cylinder.

- The neutron flux in the ACRR cavity is assumed to be homogeneous and isotropic in the absence of fuel. The justification of this hypothesis comes from the fact that neutrons in the central cavity have been scattered many times in the pool water.

- The EEOS fuel only absorbs neutrons and doesn not scatter them (the greater the fuel enrichment, the better this approximation). Thus the accuracy of the calculation is better for highly enriched fuel, but it is still sufficient for the 15% enriched EEOS fuel.

- The neutrons created by fission inside the fuel do not contribute to the energy profile, they escape to the reactor pool.

The method was first used to study the energy deposition into the EEOS pressure cell fuel. (50% dense UO_2 powder, 15% enrichment, 2.3 mm high, 10.3 mm diameter). Figure III.6 shows a contour plot of the calculated radial and axial energy distribution in this sample. The energy distribution is normalized to the volumetric average energy in the sample. The resulting ratio of peak-to-minimum energy deposition (pm) is 1.17.

For the purpose of the precise energy evaluation, it is desirable to make the energy deposition in the pressure cell as uniform as possible. One good means is to cool the hot corners of the fuel sample by surrounding it with a suitable neutron absorber, e.g. cadmium. The PATH code was therefore used to find height and thickness of that cadmium filter which would minimize pm. The optimum cadmium filter turned out to be .2 mm thick (which is practically black for thermal neutrons) and 15.2 mm high. The pm - ratio for this filter design is 1.064 (Figure III.7). The corresponding peak-to-average ratio is pa = 1.040. These numbers compare very well with the earlier TWOTRAN result of pm = 1.07 $\pm$.02 and pa = 1.05 $\pm$ .02 /III.4,6/, calculated for a similar filter design.

The above given results refer to the initial fuel powder geometry. As the fuel sample is melted and partially vaporized during the reactor transient, its geometry changes due to pressure gradients. These changes in fuel geometry make the energy deposition profile time-dependent. Since this quantity enters the energy evaluation, the PATH energy deposition calculations were also performed for various compacted fuel geometries.

Only the results for an extreme limit of fuel movement are presented here: the full radial and axial compaction of the powder to a density of 8 g/cm^3 (Fig. III.8). It is seen that even in this case the peak-to-minimum ratio of energy deposition increases only to pm = 1.073 (it was 1.064 for the powder).

However, there is ample experimental and theoretical information, showing that it is highly unlikely during EEOS experiment to have such a compacted fuel geometry for significant fractions of the power excursion. Rather, the fuel is violently moved throughout the available volume and thus a near-uniform fuel density distribution should exist for most of the experiment time.

Therefore the energy deposition results for the powder geometry with optimum cadmium filter are used in the data evaluation for the pressurization time.

III.5 Ratio of Fissions

The ratio in the number of fissions induced in the pressure cell fuel and the calorimeter fuel, is needed to calculate the absolute energy deposition into the pressure cell. The ratio of fissions was deduced in the following way.

III.5.1 Fission Product Inventory Analyis

After irradiation of the EEOS package in the ACRR, the number of fissions in the two fuel samples was measured using the ^{140}Ba - ^{140}La fission product inventory analysis.

The fission product decay chain of importance is

$$^{140}Xe \xrightarrow[16s]{3.7} {}^{140}Cs \xrightarrow[66s]{2.3} {}^{140}Ba \xrightarrow[12.8d]{0.3} {}^{140}La \xrightarrow[40.22h]{0.0} {}^{140}Ce$$

(fission yield) (half life) (stable)

Essentially all of the ^{140}Xe and ^{140}Cs will decay into ^{140}Ba within a very short time, compared with the ^{140}Ba half-life, after irradiation. Thus, after several hours a parent-daughter decay relationship between ^{140}Ba and ^{140}La is established. Solving the radioactive decay equations in the usual way gives an equation for the number of ^{140}Ba isotopes produced in the irradiation as function of measurement time and ^{140}La-activity (see e.g. Ref. II-1, p.208). The disintegration rate of ^{140}La is measured with a gamma ray spectrometer. Once the number of ^{140}Ba atoms is known for time $t=0$, the number of fission events follows from the ^{140}Ba fission yield.

The fission product inventory analysis is performed for the pressure cell and the calorimeter with identical fuel-counter distance.

III.5.2 Gamma Self Shielding

The gamma counting technique must take into account that the material distribution between the gamma source (fuel) and the counter is not identical for the case of pressure cell and calorimeter. This gives rise to different gamma self shielding in the two cells which was accounted for by two measures:

1. Addition of compensating shims to the more transparent calorimeter (2 mm Zr and 14.6 mm Al). These shims balance the Zr crucible and the thick aluminium base of the pressure cell. Counting direction is through the base of the calorimeter and pressure cell (Fig. III.9).

2. An analytical correction of remaining small differences in gamma absorption, e.g. from the different fuel geometries in both cells, was performed using the Monte Carlo photon transport code PABST /III.7/.

The PABST code (Photon Absorption Efficiency Study) calculates the uncollided flux at a point due to an isotropic volumetric photon source. The combinatorial geometry package from the MORSE code is used to model the problem in three dimensions. Gamma-ray cross sections from the QAD-CG code are used in the PABST code.

The PABST code randomly chooses a start location from a uniform volumetric source region defined by two coaxial cylinders (axis parallel to z-axis). The detector location is either a point detector or an area detector, in which case the detector point is randomly choosen on the detector disk (Figure III.9). The combinatorial geometry package from the MORSE code calculates the number of mean free paths from the start location to the detector location.

X-ray photographs of irradiated pressure and calorimeter cells always showed that the initially powdered fuel coated the crucible walls as thin dense uniform layer at frozen fuel. Therefore the fuel region was modelled as a layer of 100% dense UO_2 on the internal crucible walls. Typical layer thickness was .43 mm on the pressure cell walls and .17 mm on the calorimeter walls.

Figure III.10 summarizes the main PABST results for
a) a plain calorimeter without additional shims,
b) a calorimeter with shims (as shown in the left part of Fig. III.9) and the hexagonal hole in the calorimeter seal filled with a Zr plug, and finally
c) a plain pressure cell, as shown in the right part of Fig. III.9.

For a given gamma flux from the fuel region, about 30% more gammas reach the detector in the case of the unshielded calorimeter than in the case of pressure cell. When shims are added to the calorimeter,

such that the thickness of Zr and Al layers in both arrangements are identical and the hole in the calorimeter seal is plugged, the calculated detector count rates become very similar. The still slightly lower transparency of the pressure cell is due to the thicker fuel crust and the stainless steel set screw, which has no counterpart in the calorimeter. Averaged over the active detector area, which ranges from 5.5 to 26.25 mm radius, the ratio of the gamma fluxes is .989. This factor was used to correct the ratio of fissions deduced from the above described fission product inventory analysis.

III.5.3 Uncertainties In The Ratio of Fissions

In the determination of the ratio of fissions, a number of uncertainties normally associated with the determination of absolute fission numbers do cancel, e.g.

- the absolute detector efficiency for 1.6 MeV photons,
- the decay probability of ^{140}La for the 1.6 MeV decay path, and
- the cumulative fission yield for ^{140}Ba.

The remaining dominant uncertainty in the ratio of fissions stems from the counter statistics. With one exception (EEOS-09) the statistical counting uncertainty was between .8 and 1.2%.

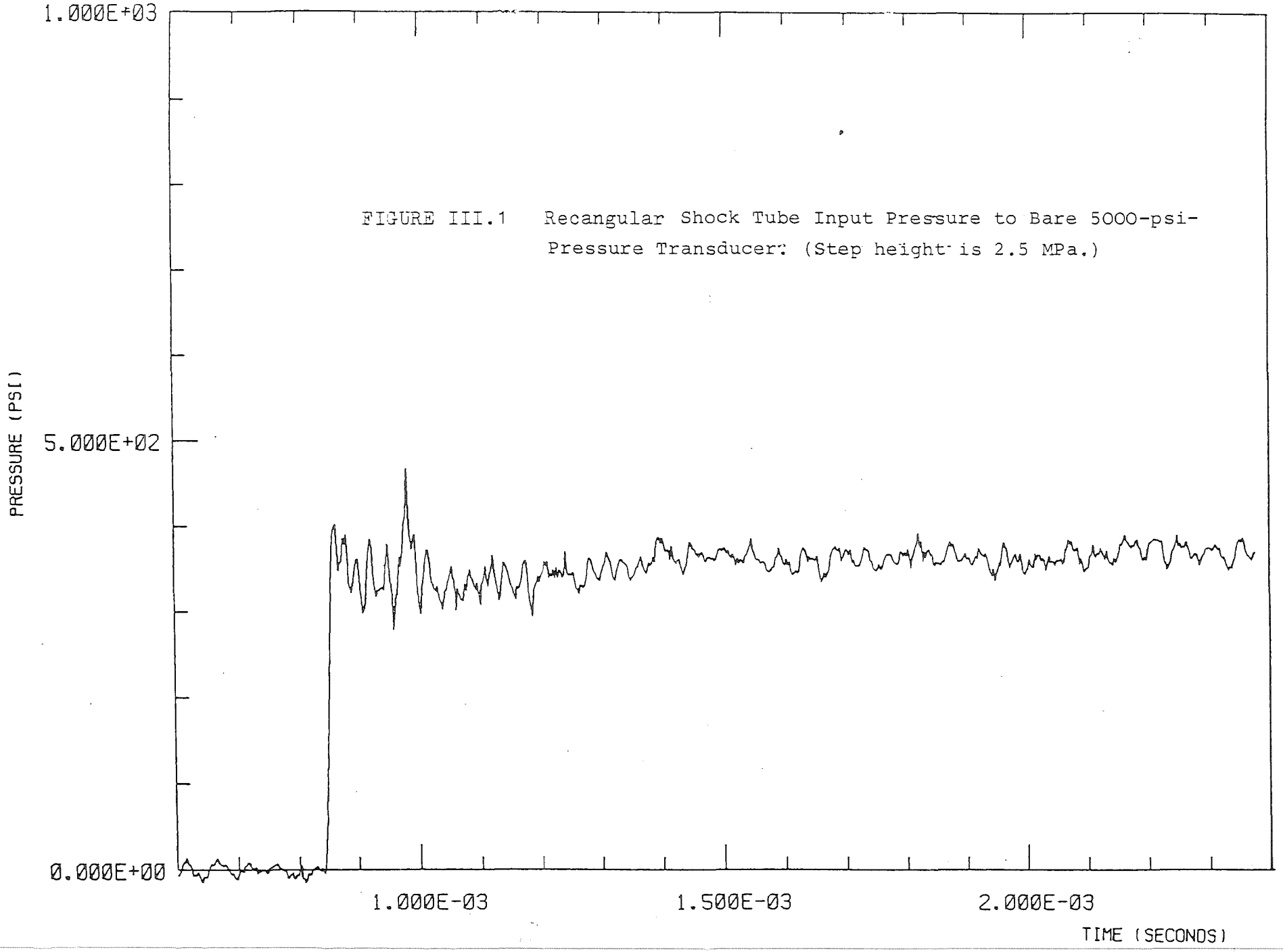

FIGURE III.1 Recangular Shock Tube Input Pressure to Bare 5000-psi-Pressure Transducer: (Step height is 2.5 MPa.)

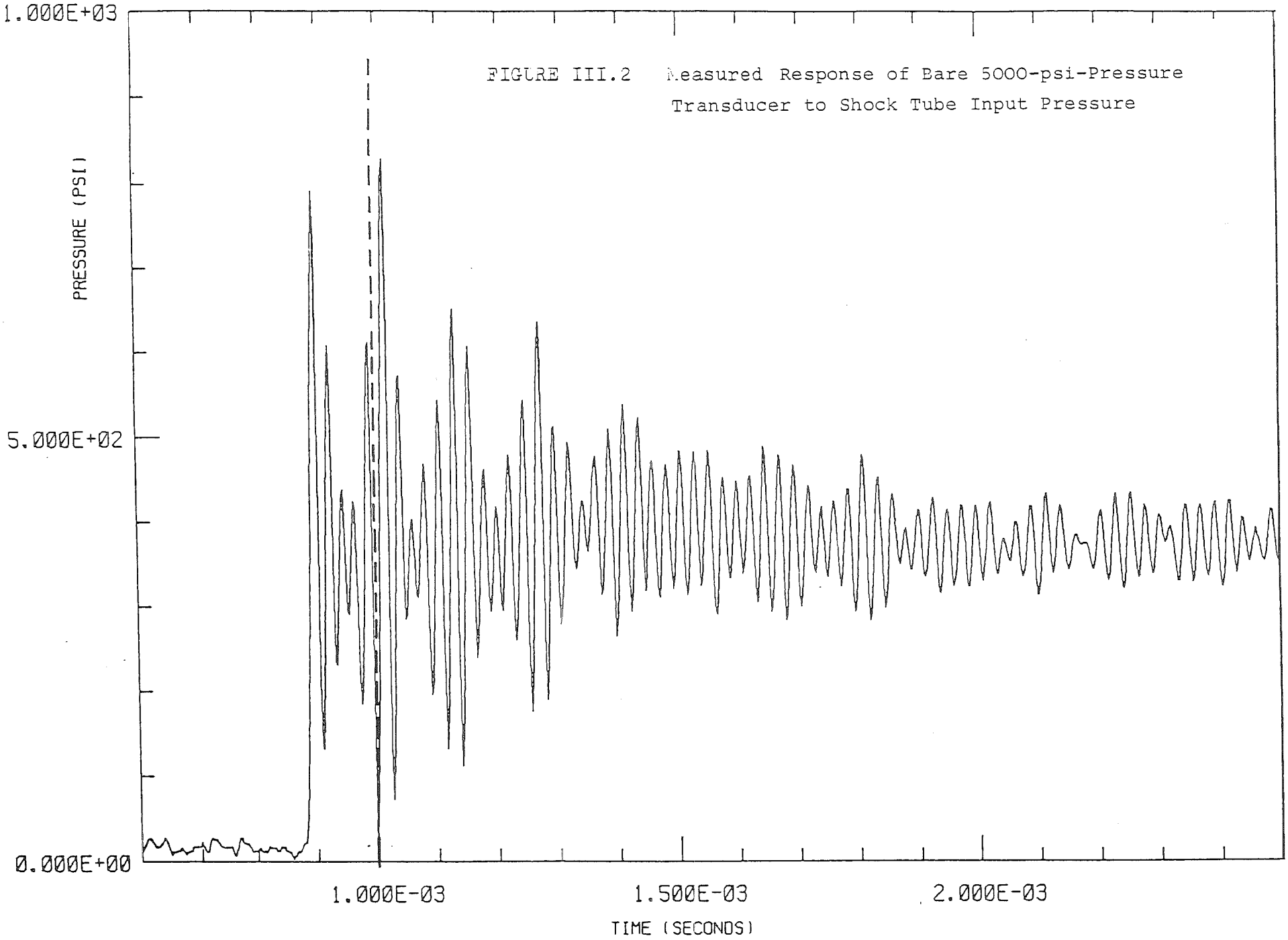

FIGURE III.2 Measured Response of Bare 5000-psi-Pressure Transducer to Shock Tube Input Pressure

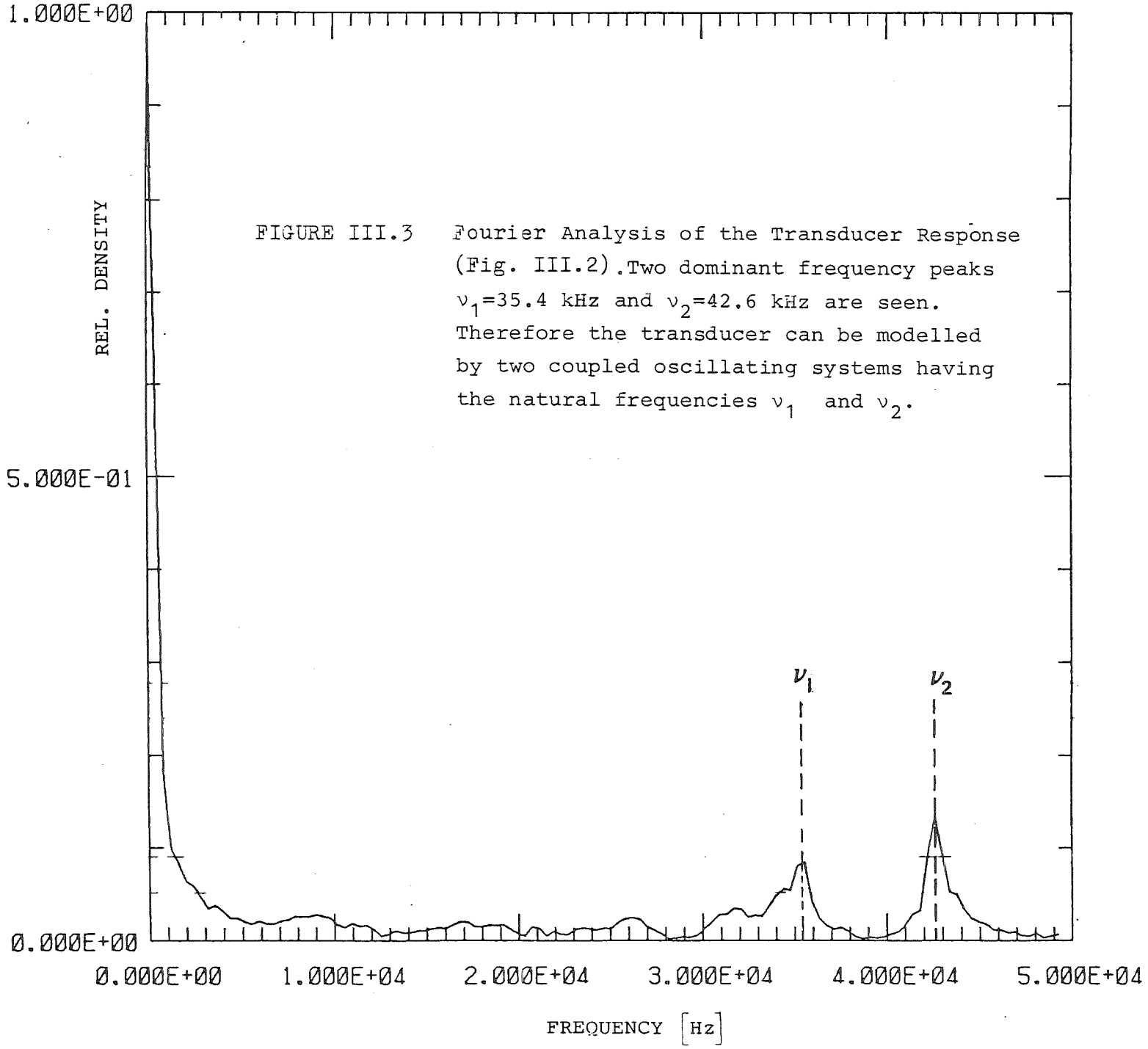

FIGURE III.3 Fourier Analysis of the Transducer Response (Fig. III.2). Two dominant frequency peaks ν_1=35.4 kHz and ν_2=42.6 kHz are seen. Therefore the transducer can be modelled by two coupled oscillating systems having the natural frequencies ν_1 and ν_2.

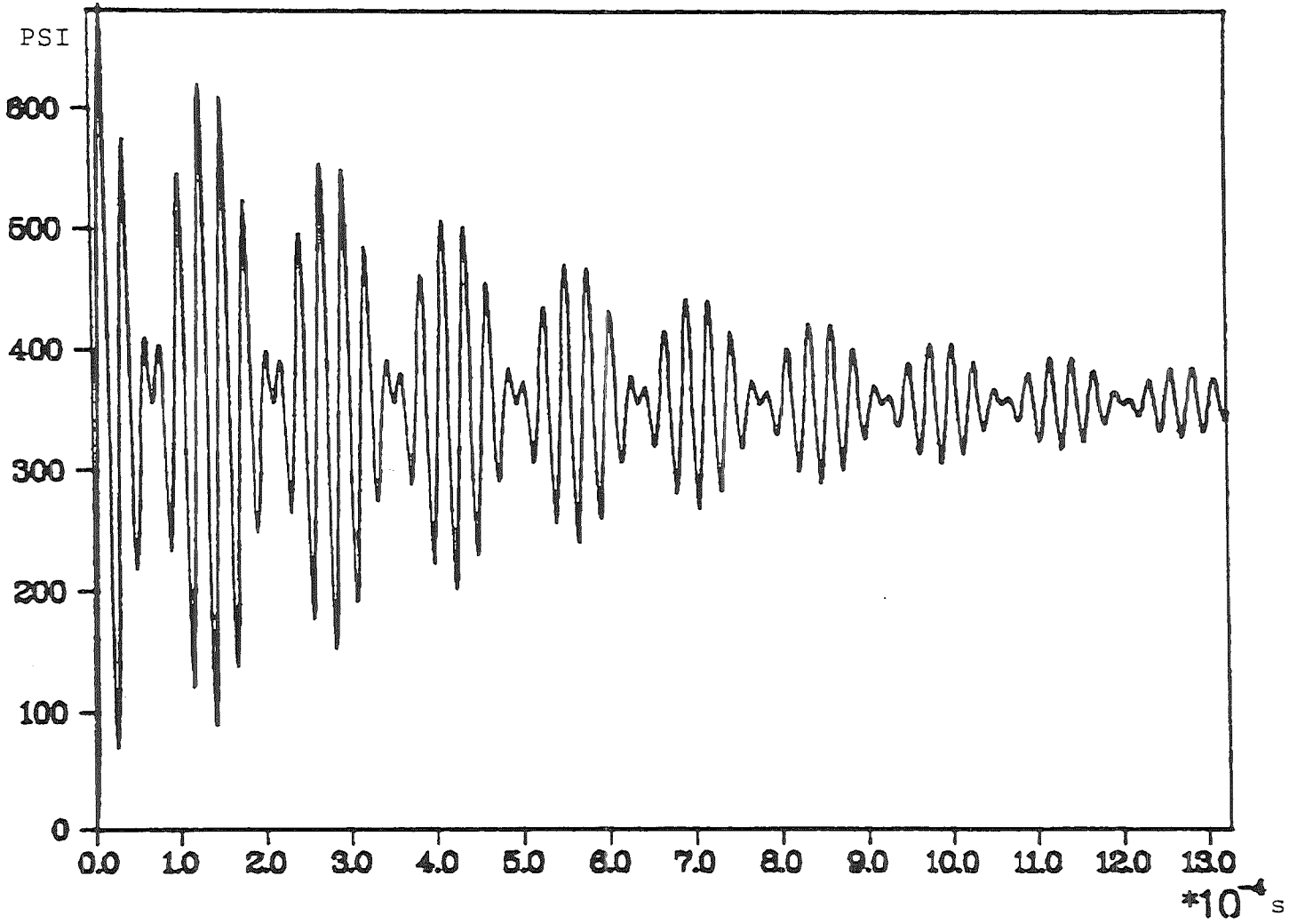

FIGURE III.4 Analytical Fit Function for the Measured Transducer Response Shown in Figure III.2

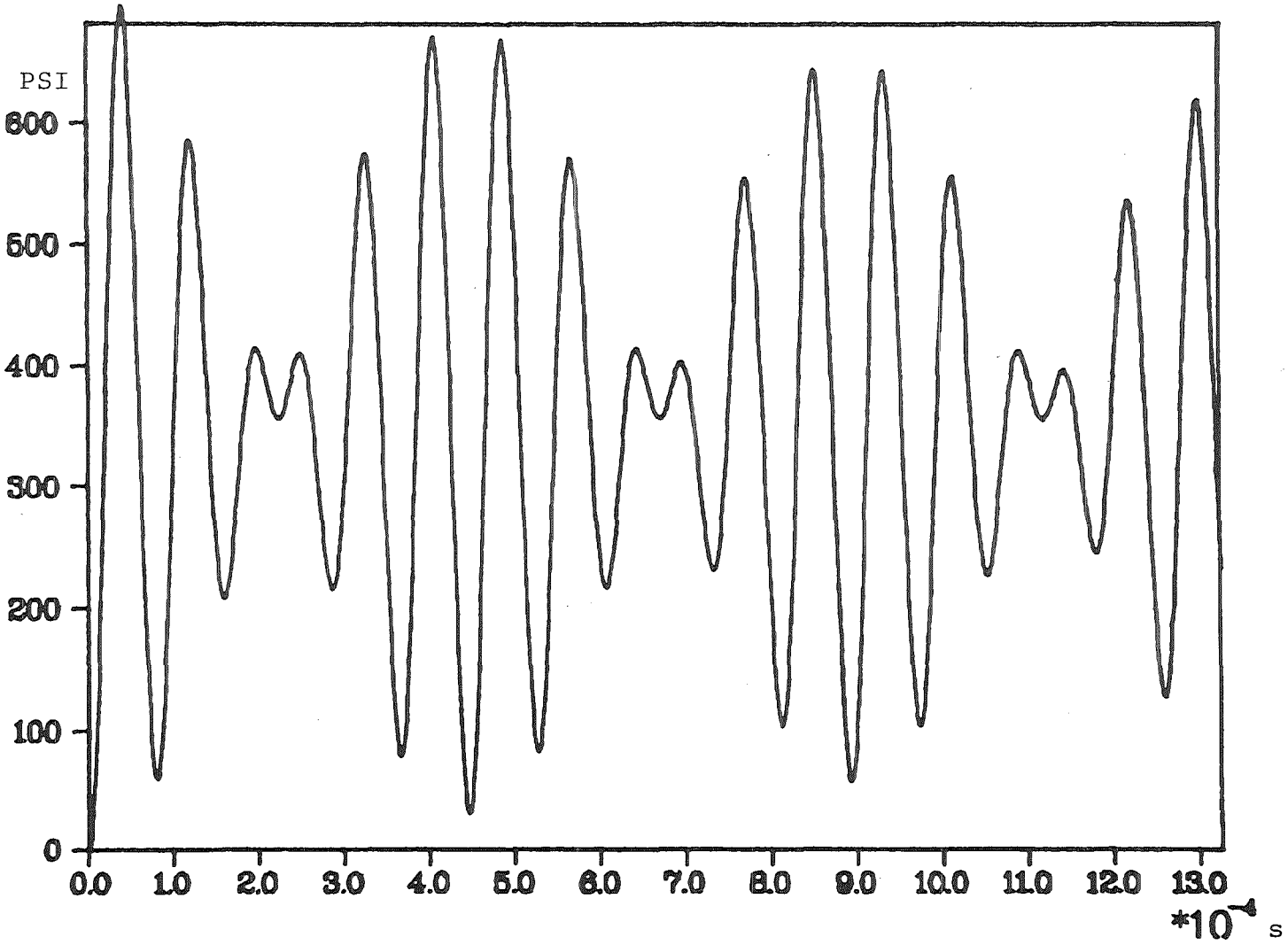

FIGURE III.5 Calculated Response of Modified Transducer to 2.5 MPa Pressure Step (Fig. III.1). The oscillating mass is ten times that of the bare transducer (R= 10). The addition of masses to the transducer membrane decreases the oscillation frequency and the damping, as can be seen from comparison with Fig. III.2 (same axis scales).

Energy/average contour plot

FIGURE III.6 Calculated Radial and Axial Energy Distribution in an Unshielded EEOS Fuel Sample of Initial Powder Geometry. The energy is normalized by the average energy. Peak-to-minimim ratio of the energy deposition is 1.10/.94 = 1.17 .

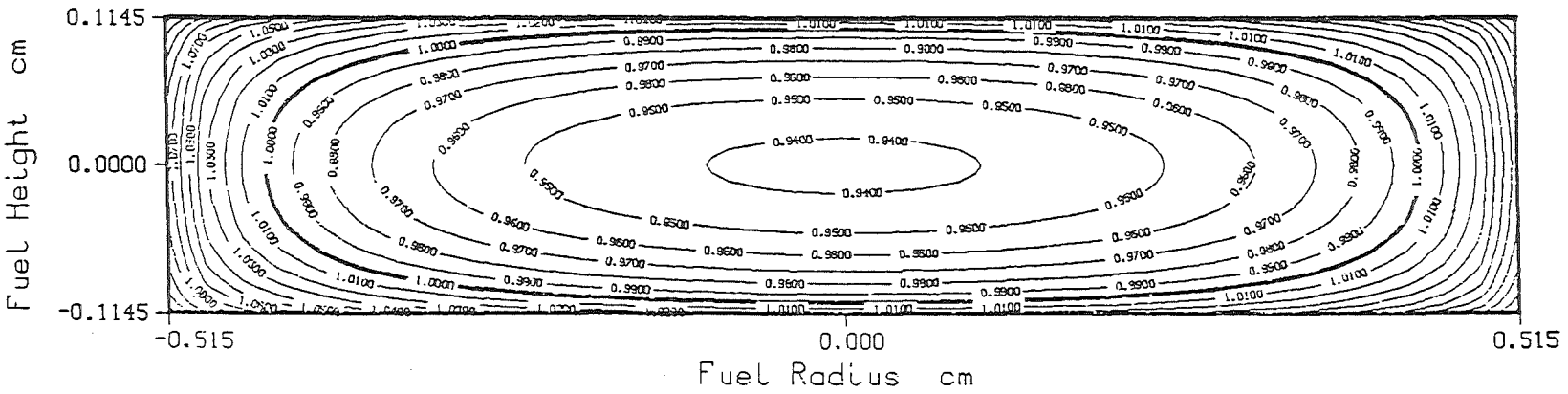

PLOT 2 13.20.30 WED 10 NOV, 1982 JOB-PJMCRTE , SANDIA ALBQ DISSPLA VER 8.2

UO2 fuel mass : 1 gram
fuel enrichment : 15 % 235-U
fuel specific mass : 5.17 gram/cc
no cadmium

Energy/average contour plot

FIGURE III.7 Calculated Energy Distribution in an EEOS Fuel Powder Sample with Optimum Cadmium Filter Design. Peak-to-minimum ratio is 1.064.

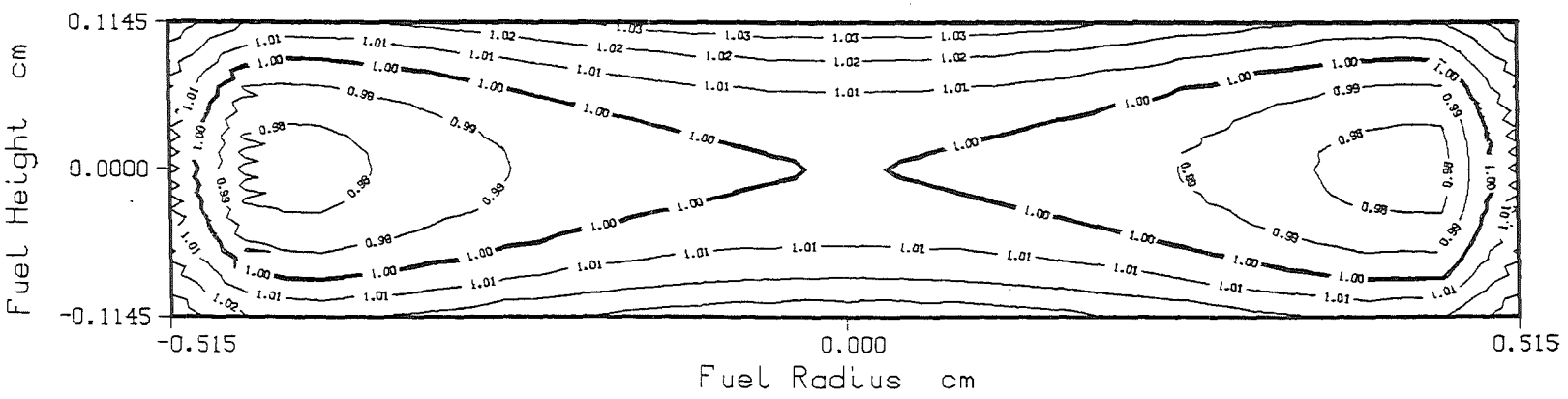

PLOT 2 15.38.59 FRI 3 DEC, 1982 JOB-NMBREITUI SANDIA ALBQ DISSPLA VER 8.2

UO2 fuel mass	:	1 gram
fuel enrichment	:	15 % 235-U
fuel specific mass	:	5.17 gram/cc
cadmium ring	:	1.43 cm radius
		1.52 cm height
		.08 cm thickness

Energy/average contour plot

FIGURE III.8 Calculated Energy Distribution in an EEOS Fuel Sample, Which Was Fully Compaced Radially and Axially to a Density of 8 g/cm^3. Even in this quite severe limit of liquid fuel motion the peak-to-minimum ratio increases to only 1.078 .

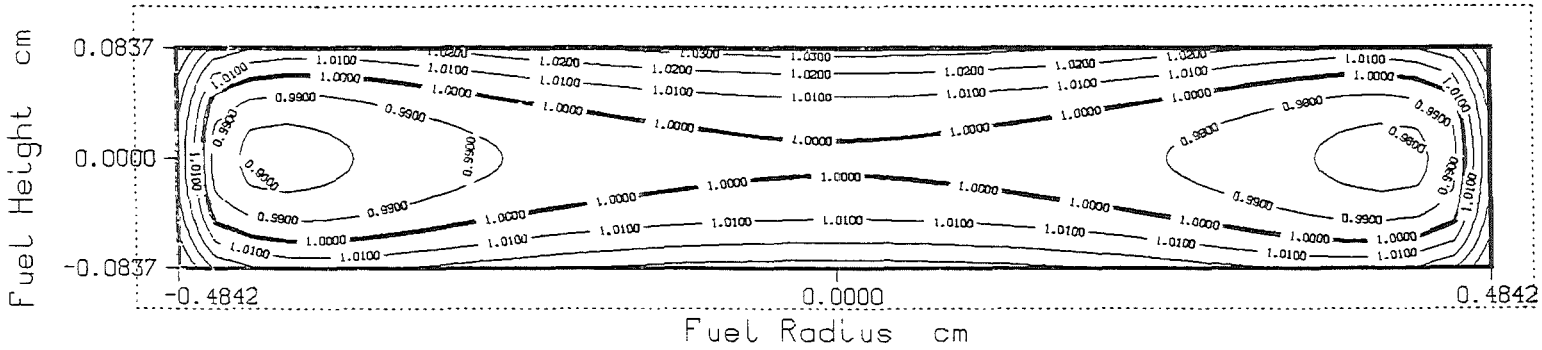

UO2 fuel mass	:	1.00 gram
fuel enrichment	:	15.00 % 235-U
fuel density	:	8.00 gram/cc
cadmium ring	:	1.43 cm radius
		1.52 cm height
		.08 cm thickness

PLOT 2 10.17.32 WED 8 DEC, 1982 JOB-INBRCITUI SANDIA ALBQ DISSPLA VER 8.2

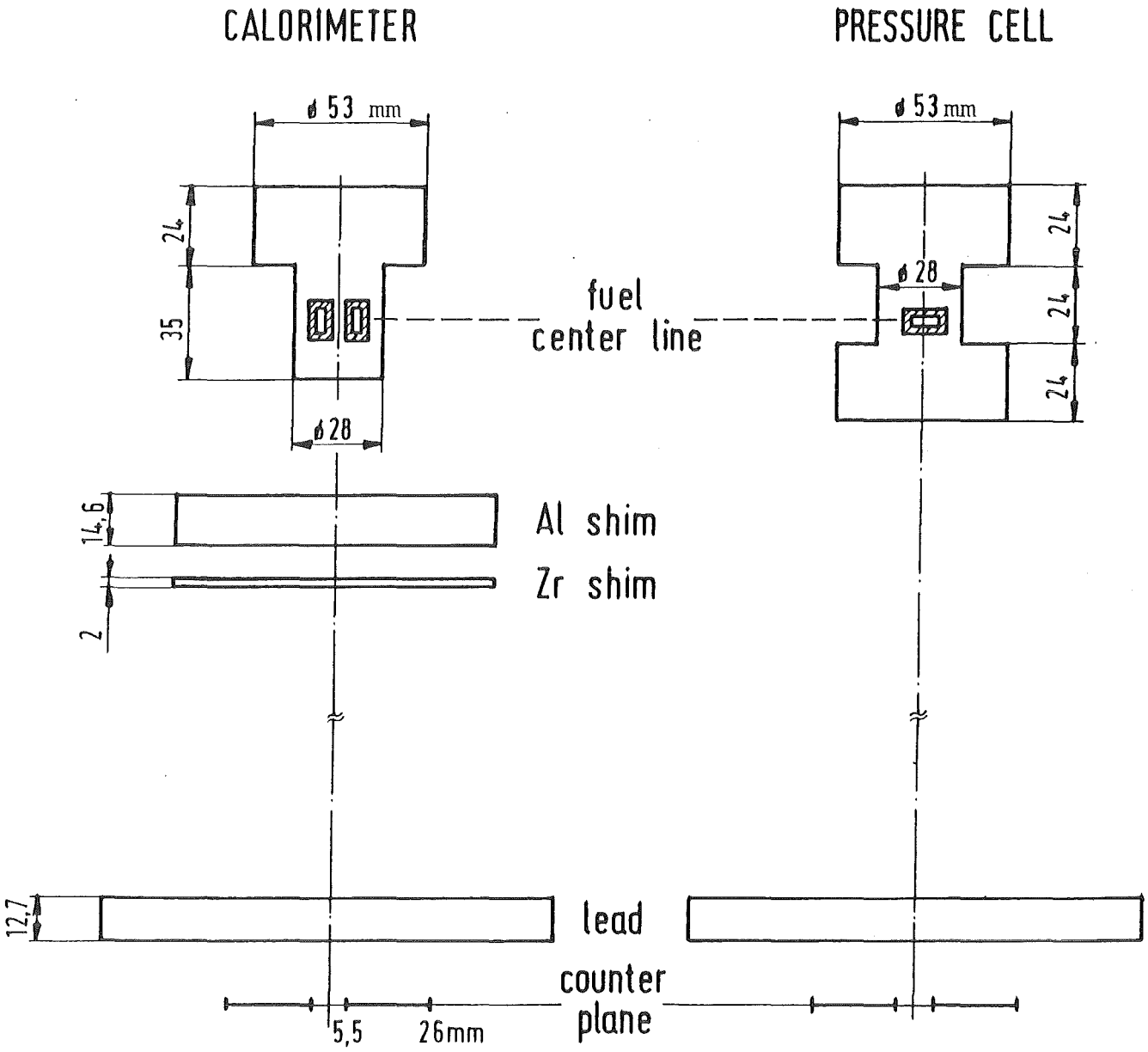

FIGURE III.9 Set-up for Gamma Counting of Irradiated Calorimeter (left) and Pressure Cell (right). The Zr and Al shims in front of the calorimeter compensate the Zr crucible and thick aluminium base of the pressure cell.

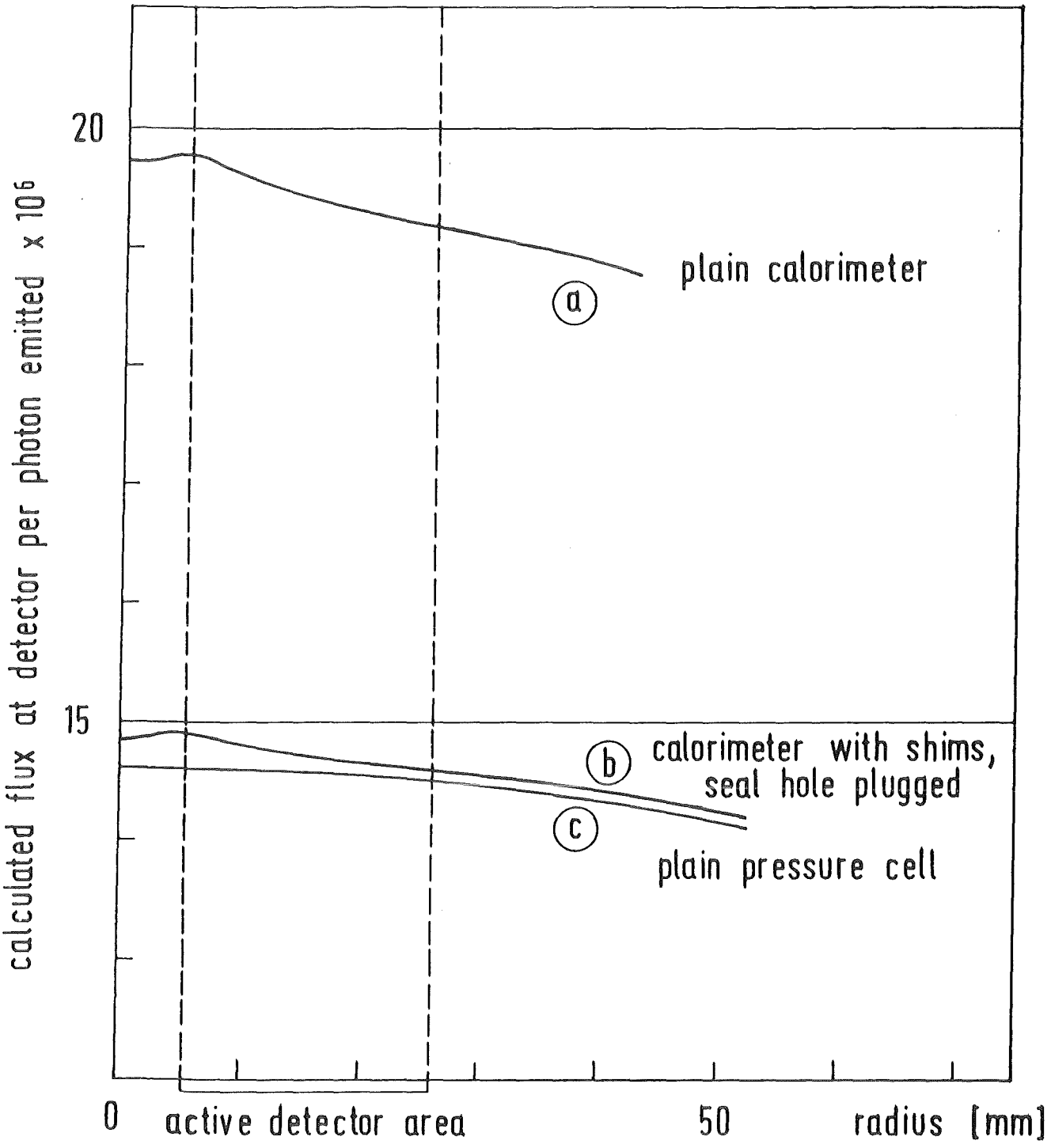

FIGURE III.10 Calculated Gamma Flux at the Detector using the Monte Carlo Gamma Transport Code PABST. The plain calorimeter transmitts significantly more gammas than the plain pressure cell.The calorimeter modified with shims and seal hole plug(Fig.III.9)yields a 1.1% higher count rate than the pressure cell.The measured ratio of fissions using the set-up of Fig.III.9 was corrected by this 1.1%.

IV TEST PREPARATION

IV.1 Contamination Control

It has become clear from other in-pile experiments (e.g. the VIPER tests) that measured fuel or fission product pressures can be totally masked by contaminations. (Any substance giving rise to an additional non-fuel pressure during the experiment must be considered a contaminant). The control of contamination is therefore a necessary prerequisite for vapor pressure measurements on nuclear fuels.

For the design of a material cleaning and handling procedure, various aspects of the initially rather obscure phenomenon of "contamination" were investigated in detail /IV.1/. The following findings are important for the control of contamination in EEOS experiments:

- Only a few 10^{-5} g of volatile materials are tolerable in the present EEOS experiment design.
- The dominant transfer mechanisms for contaminant substances are direct contact, physical absorption of gases or vapors, and deposition of aerosols from the ambient atmosphere.
- Direct contact contamination mainly results from a variety of human contaminations, e.g. a single fingerprint can transfer 10^{-4} g of volatile materials.
- Important for contamination by physisorbtion are those molecules which have a high heat of physisorption and whose critical temperature is above 300 K, because these molecules are capable of multilayer adsorption during the experiment preparation. Most important are water and polar hydrocarbons which can have relatively high abundances in laboratory air.
- The exposure of surfaces to normal laboratory air results in deposition of solid or liquid aerosols due to sedimentation and movement of the suspending atmosphere itself. Liquid aerosols spread into thin films spontaneously and solid aerosols can be bound with forces which are orders of magnitude greater than the corresponding gravitational force on the aerosol.

Based on these findings appropriate cleaning procedures and facilities were designed for the EEOS experiments.

IV.2 Glove Box Facility

An ultra clean Glove Box Facility was designed, built, and used for assembly of the EEOS test packages. The facility consists of two main subsystems: the glove box and the attached ultra-high vacuum (UHV) system. Figure IV.1 depicts the outlay of the glove box. The components in the lower left serve to maintain a high-purity argon atmosphere within the glove box. Water and oxygen partial pressures are maintained at a few ppm. The other components are used for:

- evacuating the pass-through; running a particulate vacuum cleaner in the box (parts in lower right of Figure)

- filling and pressure testing the inner containment canister with helium (parts in upper right of Figure),

- evacuating and filling the ultra-violet-light cleaning chamber (top of Figure), and

- bleeding gases into the UHV system (left middle part of Figure)

The UV-cleaning chamber allows cleaning of cell parts from physically absorbed hydrocarbon contamination.

Figure IV.2 shows the UHV-system, which is designed to allow

- bakeout of the open pressure cell to remove residual water,
- sealing of the pressure cell in situ,
- evacuation and sealing of the calorimeter,
- analysis of atmospheres during bakeout and
- analysis of post-test atmospheres in the pressure cells.

The attached mass spectrometer is an important tool for the contamination control in the EEOS experiments. The system has been automated to provide computerized control of the mass analyzer and reduction of the measured ion intensities to absolute partial pressures.

Important design aspects of the system are:

- oil free pumping by using a combination of absorption and ion pumps,
- reliable operation since there is no mechanical wear,
- no exhaust during operation, and
- safe against loss of power.

The system was designed to allow also irradiated fuel work.

IV.3 Preparation Routes

IV.3.1 Pressure Cell And Calorimeter Components

The pressure cell components are all fabricated from metals, the parts must first be cleaned and then processed under controlled conditions.

Table IV.1 shows anticipated contamination substances together with the cleaning steps used for their removal. Cleaning is designed to take place in three different environments with increasing degree of cleanlines. Thus contamination from intermediate processing steps or from previous insufficient cleaning can be compensated for at the next level of cleaning. Because physically adsorbed multilayers of water and volatile hydrocarbons are expected to be major causes for contamination, the two last cleaning steps emphasize removal of these molecules.

Table IV.1: Summary of Cleaning Steps for EEOS Pressure Cell Components

Contamination Source and Expected Contaminations	class	Primary Cleaning	Secondary Cleaning (combined with storage)	Final Cleaning
1. Contact contamination:		Mechanical cleaning in water-ethanol, affected class: B,C	UV-ozone cleaning supported by active adsorbents for water and hydrocarbons	heating in UHV-system to about 500 K
- gross hydrocarbons	A			
- inorganic salts	B			
- particulates	C			
		Ultrasonic cleaning in triclorethylene, affected: A,F	affected contaminants: E,F	affected contaminant : E
2. Airborne contamination:		Ultrasonic cleaning in water-ethanol, affected: B,C,D		
- particulates	D			
- water	E			
- film hydrocarbons	F	UV-ozone cleaning affected: A,F		

After primary and secondary cleaning of the individual cell components, the top and bottom halves of the EEOS-cells were assembled in the glove box described above. The preassmebled cell was then stored in the UV-ozone box, which is located within the glove box. Eventual hydrocarbon contamination from preassembly should be removed by the UV-ozone cleaning process which was active during storage. The preassembled cell was only removed from the storage environment shortly before fuel loading.

Although the pressure build-up from contaminants does not adversely affect the calorimeter performance, the calorimeter parts were cleaned the same way as the pressure cell components, in order to avoid system and cross-contaminations.

IV.3.2 Fuel

While the pressure cell components are significantly contaminated in the as-received state and must be cleaned to the desired cleanliness level, the fuel must be kept in its as-received state throughout the processing. Care was taken to

- avoid contact contamination during handling by using only tools with clean hard surfaces like glass, metals or ceramics,
- avoid contamination from working atmospheres (physisorption, particulates) by keeping water and hydrocarbon vapor concentrations below 10 ppm in the glove box atmosphere.

Any water vapor that may have been adsorbed on the fuel powder nevertheless, should probably have been released in the final vacuum bakeout of the loaded pressure cell.

The ultra-pure UO_2 was already received in the powdered state, the pellets of reactor grade UO_2 and $(U,Pu)O_2$ were crushed with a stainless steel pestel and mostar under high purity argon.

IV.4 Fuel Characterization

The experiments described in this report utilized

1. ultra pure UO_2 powder in experiments EEOS-04 and 05,
2. reactor grade UO_2 in experiments EEOS-06 and 07, and
3. reactor grade $(U,Pu)O_2$ in experiments EEOS-08 and 09.

The ultra-pure UO_2 powder was specially fabricated at Los Alamos National Laboratory (LANL) to be as free as possible of impurities. Table IV.2 lists the most important impurity levels as determined at LANL and other relevant fuel specifications.

Immediately after fabrication the UO_2 was sealed under high-purity argon in a thoroughly cleaned stainless steel container and transferred into the clean glovebox at SNL, described above.

Table IV.2 Specifications of High Purity Uranium Dioxide Powder

O/U ratio	2.01 ± .005		Impurity contents:		
			Mg	<10	ppm
U-234	.11	atom %	Si	15	ppm
U-235	15.00	atom %	V	<25	ppm
U-236	.13	atom %	Fe	<15	ppm
U-238	84.76	atom %	Cu	13	ppm
			Zn	<25	ppm
mean powder particle size	4.	10^{-6} m	Sr	<40	ppm
			Mo	<25	ppm
			Bi	15	ppm
			H_2O	100±50	ppm
			C	5±2	ppm
			Cl	<5	ppm
			F	8±2	ppm
			P	<5	ppm
			S	20±2	ppm
			N	19±2	ppm

The reactor grade UO_2 stems from fuel pins originally fabricated for Sandia's Prompt Burst Energetics (PBE) program by LANL. A spare pin from that program was disassembled and pellets used for experiments EEOS-06 and 07. The fuel specifications are summarized in Table IV.3

The reactor grade mixed-oxide pellets were also fabricated at LANL following processes used for previous reactor test fuel fabrication. The results of various fuel examinations are presented in Table IV.4.

Both reactor grade fuel types had a relatively high oxygen-to-metal ratio. However, thermodynamic calculations show that the total pressure in equilibrium with $UO_{2\pm x}$ or $(U,Pu)O_{2\pm x}$ is insensitive to changes of x at the very high temperatures probed in the EEOS experiments. This results from the fact that the oxygen potential of the condensed phase $\Delta\bar{G}_{O_2}(x,T)$ becomes rather independent of x at such high temperatures. All other thermodynamic quantities which influence equilibrium partial pressures (see e.g. Equations 15-17 in Ref. I.3) do not depend on the stoichiometry of the condensed oxide.

Table IV.3 Specifications of Reactor Grade Uranium Dioxide Pellets

O/U ratio	2.08		Impurity contents:		
			Mg	3	ppm
U-234	.093	atom %	Si	2	ppm
U-235	14.23	atom %	V	< 30	ppm
U-236	.086	atom %	Fe	2	ppm
U-238	85.59	atom %	Cu	< 1	ppm
			Zn	< 30	ppm
			Sr	< 45	ppm
			Mo	< 30	ppm
			Bi		ppm
			H_2O		ppm
			C		ppm
			Cl		ppm
			F		ppm
			P	< 115	ppm
			S		ppm
			N		ppm

Table IV.4 Specifications of Reactor Grade $(U,Pu)O_2$ Pellets

O/(U+Pu)	2.09		Impurity contents:		
			Mg	< 3	ppm
Pu-238	.075	atom %	Si	25	ppm
Pu-239	87.00	atom %	V	< 5	ppm
Pu-240	11.55	atom %	Fe	95	ppm
Pu-241	1.16	atom %	Cu	25	ppm
Pu-242	.211	atom %	Zn	< 10	ppm
Pu/(U+Pu)	26,85	weight %	Sr	< 5	ppm
			Mo	< 10	ppm
			Bi	< 1	ppm
			H_2O	370	ppm
			C	170	ppm
			Cl	5	ppm
			F	< 5	ppm
			P	6	ppm
			S	770	ppm
			N	5	ppm

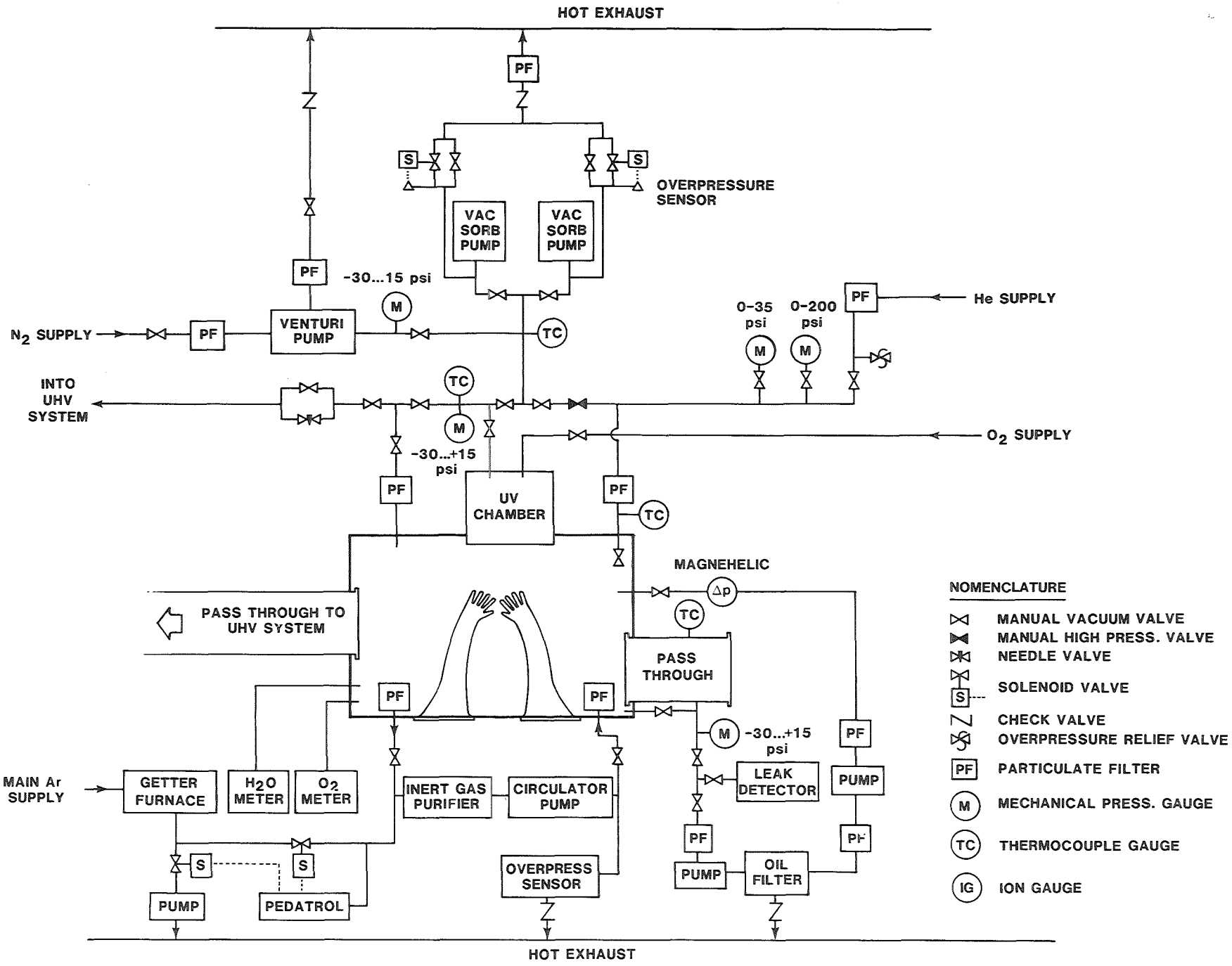

FIGURE IV.1 Glove Box for UV-Cleaning and Assembly of EEOS Experiment Equipment.

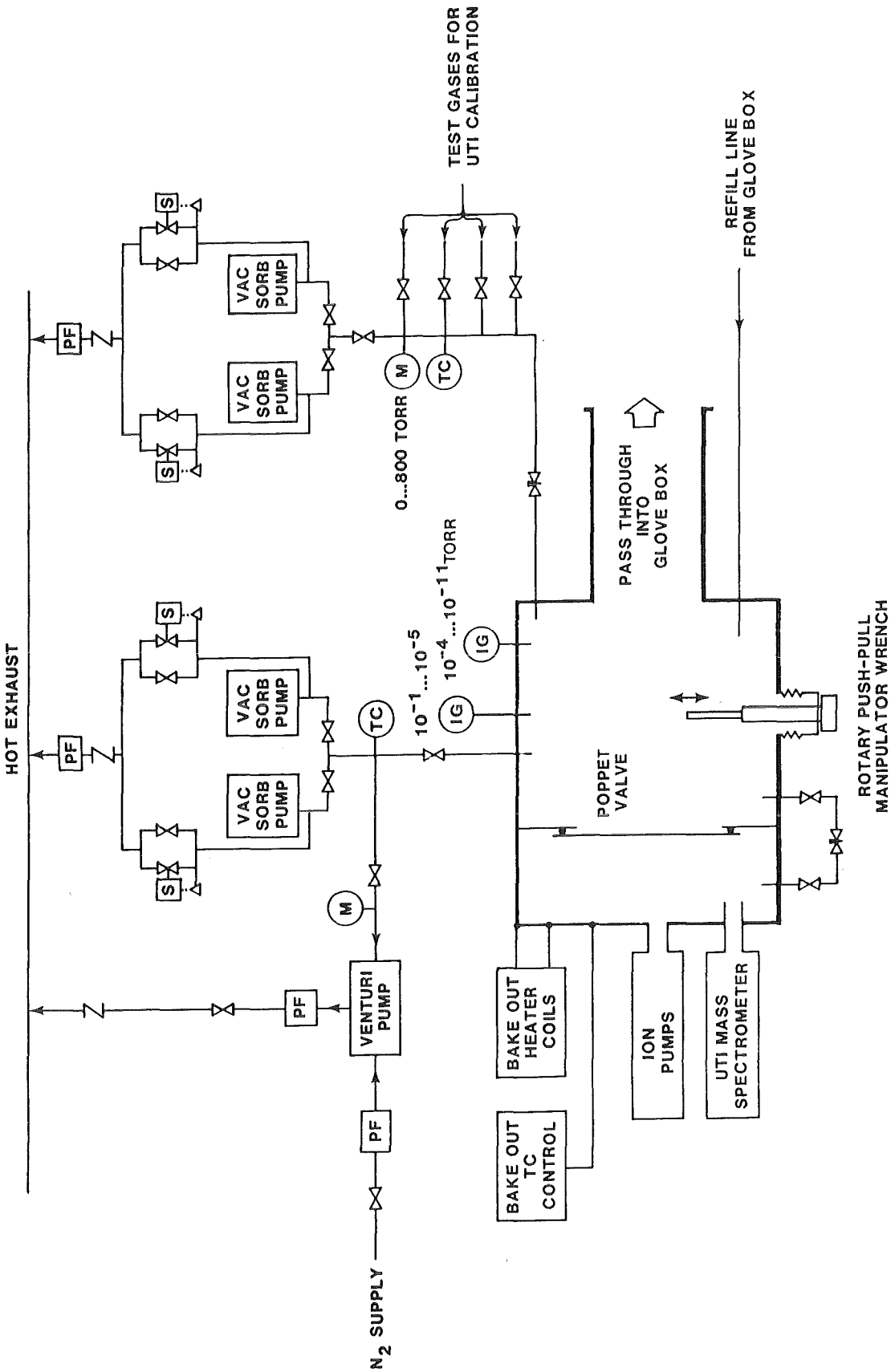

FIGURE IV.2 UHV-system for Bakeout, Evacuation and in situ Sealing of Pre-assembled Pressure Cell and Calorimeter.

V. ANALYSIS PROGRAMS

This chapter describes the analysis of the measured raw data which consist of pressure transducer voltages, fission chamber currents and thermocouple voltages.

The code called REAP (Reactor Energy Analysis Program) performs three main tasks (see Fig. II.6):

1. evaluation of the total net enthalpy deposition into the calorimeter fuel,
2. derivation of the time dependent enthalpy in the pressure cell fuel, and
3. calculation of the time dependent net pressure.

V.1 Energy Equation

The energy balance for a control volume is expressed for the present conditions as

$$\frac{\partial T}{\partial t} = \frac{1}{c_p \rho} \left[\dot{q} - \rho \frac{\partial}{\partial x} (vh) + \frac{\partial}{\partial x} \left(k \cdot \frac{\partial T}{\partial x} \right) \right] \qquad (V.1)$$

where

T = temperature of control volume (K)
t = time (s)
c_p = specific heat of fuel (J/kgK)
ρ = fuel density (kg/m^3)
$\dot{q}$ = volumetric energy deposition rate (W/m^3)
x = coordinate (m)
v = fuel velocity (m/s)
h = specific enthalpy of fuel (J/kg)
k = thermal conductivity (W/mK)

The first term in Eq. V.1 describes volumetric power generation in the control volume due to fission, gamma and beta heating. The second term describes energy transport by flowing liquid fuel,

which is only included in the pressure cell model, not in the calorimeter model. The third term describes heat conduction into the control volume. Terms for kinetic energy, potential energy and thermal expansion of fuel are neglected. Equation V.1 is solved in the calorimeter model and the pressure cell model.

V.2 Calorimeter Model

The calorimeter model uses Eq. V.1 to deduce the fission energy deposition into the fuel sample from the measured calorimeter temperature as function of time. Table V.1 summarizes the energy transfer terms Q_i^j which are modeled in REAP for the various calorimeter components and which enter on the right side of Eq. V.1. In Q_i^j, the superscript j denotes the calorimeter component (fuel, calorimeter body, etc.) and the subscript i the energy transfer mode (fission heating, conduction, etc.). The modeling equations for the individual energy transfer terms Q_i^j are given in the following sections.

V.2.1 Fission Heating

The fission power of the calorimeter fuel sample, Q_{fis}^f is written as:

$$Q_{fis}^f(t) = i(t) \cdot c \cdot m^f \qquad (V.2)$$

where

- i = fission chamber current measured during the ACRR pulse (A)
- c = neutronic coupling factor of calorimeter fuel (kW/kg A)
- m^f = mass of calorimeter fuel (kg)

The coupling factor c is initially not known, it represents the fundamental constant describing fuel fission heating. Its value is determined from a calculated fit of the measured calorimeter temperatures.

Calorimeter Component	Material	Energy Transfer Q_i^j / Model Equation					
		Fission Heating	Gamma Heating	Beta Heating	Solid Conduction	Gaseous Conduct.	Radiation
Fuel	UO_2,(U,Pu)O_2	Q_{fis}^f Eq. V.2	Q_γ^f Eq. V.4		Q_{sc}^j Eq. V.8		
Calorimeter Body	Al+Zr		Q_γ^{cb} Eq. V.3	Q_β^f Eq. V.7	Q_{sc}^j Eq. V.8	Q_{gc}^j Eq. V.9	Q_{rad}^j Eq. V.10
Support Rod	Machinable Ceramic		Q_γ^{rod} Eq. V.5		Q_{sc}^j Eq. V.8		
Calorimeter Case	Al		Q_γ^{cs} Eq. V.6		Q_{sc}^j Eq. V.8	Q_{gc}^j Eq. V.9	Q_{rad}^j Eq. V.10

Table V.1 Summary of Energy Transfer Processes Q_i^j Modelled in the Calorimeter Calculations.

V.2.2 Gamma Heating

All calorimeter components are heated by the intense gamma radiation during an ACRR pulse. Even with the lead shield (Fig. II.3) typical gamma heating amounted to 30 to 40 K. The gamma heating was measured for each EEOS experiment by irradiating an empty (not fueled) calorimeter.

V.2.2.1 Calorimeter Body

The gamma heating power of the calorimeter body, Q_γ^{cb}, in ACRR shot K is calculated from the relation

$$Q_\gamma^{cb}(t) = \left[E_{BG}^{pr} \cdot \frac{i_K(t)}{I_{BG}} + \frac{E_{BG}^{pr} \cdot \Gamma(t) \cdot I_K}{G \cdot I_{BG}} \right] \cdot \frac{m_K^{cb}}{m_{BG}^{cb}} \qquad (V.3)$$

where

E_{BG}^{pr} = gamma heating of the empty calorimeter body from prompt core gammas as measured in the background shot, (J)

$i_K(t)$ = fission chamber current measured in shot K (A)

I_K = total fission chamber charge in shot K (As)
$= \int_0^\infty i_K(t)dt$

I_{BG} = fission chamber charge in the background shot (As)
$= \int_0^\infty i_{BG}(t)dt$

$\Gamma(t)$ = average gamma decay power of core fission products (MeV/s/fission)

G = average gamma decay energy of core fission products
$= \int_0^\infty \Gamma(t)dt = 6 \pm 1$ MeV/fission

m_j^{cb} = mass of calorimeter body in shot j (kg)

The first term on the right side of Eq. V.3 represents the prompt fission gammas from the core. The second term describes the delayed gamma heating from the decay of core fission products. The formulation in Eq. V.3 uses the fact that prompt and delayed decay energies are about equal (both 6 $\pm$ 1 MeV/fission) and it also assumes that all fissions occur at the time of the prompt pulse.

V.2.2.2 Calorimeter fuel

The gamma heating of calorimeter fuel cannot be measured directly because of the simultaneous fission energy release in the fuel sample. The gamma heating of UO_2 was therefore determined indirectly in one background shot, using lead as a simulant for fuel. Comparison of the calorimeter temperature rise with and without lead allows the mean energy of the incident gamma flux to be determined from the known gamma energy absorption coefficients of lead and aluminium. Knowing this mean gamma energy (1.66 MeV), the gamma heating power of UO_2 can be evaluated from the measured gamma heating of aluminum, Q_γ^{cb}:

$$Q_\gamma^f(t) = Q_\gamma^{cb}(t) \cdot \frac{m^f}{m^{cb}} \cdot \frac{(\mu/\rho)^{UO_2}_{1.66}}{(\mu/\rho)^{Al}_{1.66}} \qquad (V.4)$$

where

Q_γ^{cb} = gamma heating of calorimeter body (Eq. V.3) (W)

m^f, m^{cb} = mass of calorimeter fuel and calorimeter body, respectively, (kg)

$(\mu/\rho)^i_{1.66}$ = energy absorption coefficient of substance i for 1.66 MeV gammas (m^2/kg) (taken from literature)

For the ratio gamma absorbtion coefficients in Eq. V.4 a value of 1.351 was used.

V.2.2.3 Ceramic support rod

The gamma heating of the ceramic support rod was calculated from the measured gamma heating of the calorimeter body, Q_γ^{cb}, using a relation analogeous to Eq. V.4:

$$Q_\gamma^{rod}(t) = Q_\gamma^{cb}(t) \cdot \frac{m^{rod}}{m^{cb}} \cdot \frac{(\mu/\rho)^{rod}_{1.66}}{(\mu/\rho)^{cb}_{1.66}} \qquad (V.5)$$

Since the atomic numbers of the ceramic rod constituents (O,Si,Mg, Al) are all close to that of aluminum, which is the main body material, the ratio of gamma mass absorption coefficients in Eq. V.5 was set to 1.0.

V.2.2.4 Calorimeter case

The gamma heating of the calorimeter case, which is fabricated from aluminum, was evaluated from

$$Q_\gamma^{cs}(t) = Q_\gamma^{cb}(t) \cdot \frac{m^{cs}}{m^{cb}} \cdot \frac{\phi^{cs}}{\phi^{cb}} \qquad (V.6)$$

where

m^{cs} = mass of calorimeter case (kg)
m^{cb} = mass of calorimeter body, (kg)
ϕ^{cs}/ϕ^{cb} = ratio of gamma flux incident on calorimeter case to that of calorimeter body

Using the known gamma attenuation coefficient for 1.66 MeV in Al the gamma flux ratio was estimated to 1.02.

V.2.3 Beta Heating

An additional delayed energy deposition into the calorimeter comes from beta decay of the fission products in the calorimeter fuel. The rate of energy deposition from beta decays is

$$Q_{\beta}^{f}(t) = \frac{E_{fis}^{f}}{e_{fis}} \cdot q_{\beta}(t) \cdot p_{abs} \qquad (V.7)$$

where

E_{fis}^{f} = total fission energy deposited in the calorimeter fuel (J)
$= \int_{0}^{\infty} Q_{fis}^{f}(t)dt$

e_{fis} = energy release per fission = 167 MeV/fission
q_{β} = beta decay power per fission (MeV/s/fission)
p_{abs} = absorption probability for beta particles in the calorimeter body.

The fission heating power of the calorimeter fuel sample Q_{fis}^{f} is given in Eq. V.2. The beta decay power was taken from the literature. The absorption probability for electrons was set to 1.00.

V.2.4 Solid Conduction

REAP treats one-dimensional solid conduction from fuel to calorimeter case (via calorimeter body and ceramic rod), and from the calorimeter body to the calorimeter case via thermocouples. For a given time step, conduction is considered to be in steady state with the following energy transport rate:

$$Q_{sc}^{j} = \frac{\Delta T}{\sum_{i} R_i} \qquad \text{with} \quad R_i = \frac{L_i}{k_i A_i} \tag{V.8}$$

where

ΔT = temperature difference between node points (K)

L_i = conduction length for material layer i between the node points (m)

k_i = thermal conductivity of material layer i (W/m·K)

A_i = conduction cross section of material layer i (m^2)

V.2.5 Gaseous Conduction

The calorimeter is evacuated during test assembly and therefore the heat losses due to gaseous conduction from the calorimeter body to the calorimeter case should be negligible compared to solid conduction losses. However, since between evacuation and actual test generally several days passed, if could not always be avoided that minor traces of helium leaked from the inner container (filled with 1 bar He) into the calorimeter. Under these circumstances gaseous conduction (and possibly convection) became a noticable heat loss path. These losses were modeled using the relation

$$Q_{gc}(t) = \alpha \cdot h_{gc} \cdot \Delta T(t) \tag{V.9}$$

where

α = empirical conductivity factor

h_{gc} = heat transfer coefficient of helium (W/K)

$= k_{He} \cdot A/L$

ΔT = temperature difference between heated calorimeter body and cold calorimeter case (K)

The unknown conductivity factor α is evaluated from the measured cooling curve of the calorimeter body. α turned out to be in the range of .1 to .5 indicating that the helium pressure in the calorimeter vessel was of the order of several Pa.

V.2.6 Radiation Heat Transfer

The net radiative energy exchange between two opaque surfaces of different temperatures T_1 and T_2 is given by:

$$Q_{rad} = A \cdot \frac{\sigma(T_2^4 - T_1^4)}{1/\varepsilon_1(T_1) + 1/\varepsilon_2(T_2)^{-1}} \qquad (V.10)$$

where

A = area of radiation exchange (m^2)
σ = Stefan-Boltzmann constant
ε = wavelength-independent (gray) emissivity of the emitting surface

Equation V.10 was used with ε_{Al}=0.1 to treat radiative heat transfer between the calorimeter body and the calorimeter case.

V.2.7 Summary of Calorimeter Energy Evaluation

The equations presented above for the energy transfer modes Q_i^j contain two unknowns, the neutronic coupling factor c in Eq. V.2, and the effective heat transfer factor α in Eq.V.9. Both can be evaluated from the measured cooling curve of the calorimeter because the coupling factor mainly determines the vertical position of the cooling curve and the heat transfer factor determines the slope of the curve. REAP uses a least squares method to find that combination of coupling factor and heat transfer factor, which produces optimum agreement between measured and calculated cooling curves. The method yields a unique solution for c and α

because neutronic energy deposition and heat losses are seperated in time. There is only a small heat loss during the neutronic heating and no neutronic heating late in time when heat losses become significant.

The relative importance of the energy transfer modes discussed above, is illustrated in Table V.2 which shows calculated temperature changes of the calorimeter body due to each of the energy transfer modes modeled.

Table V.2 Temperature Change of the Calorimeter Body Due to Various Energy Transfer Modes (REAP calculation for EEOS-07, time is 10 s after reactor pulse)

Energy Transfer Mode	Temperature Change at 10 s (K)	Percent of Fission Heating
Fission heating	304.0	100.0
Gamma heating	31.0	10.2
Beta heating	6.5	2.1
Solid conduction	-13.8	-4.5
Gaseous conduction	-25.0	-8.2
Radiation	-0.5	- .16

Table V.2 demonstrates that the measured calorimeter response is clearly dominated by fission heating of the fuel. Gamma heating and gaseous conduction are both smaller by about one order of magnitude. Beta heating and solid conduction amount to a few percent of the fission heating, radiation heat transfer is insignificant.

V.3 Pressure Cell Model

The pressure cell model solves the energy balance (Eq.V.1) for the fuel and for the adjacent zirconium crucible. The energy transfer processes included in the modeling are summarized in Table V.3.

Table V.3 Summary of Energy Transfer Processes Modeled in The Pressure Cell Calculations

Pressure Cell Component	Material	Fission Heating	Gamma Heating	Conduction	Convection
Fuel	UO_2 $(U,Pu)O_2$	Q^f_{fis} Eq. V.12	Q^f_γ Eq. V.13	Q^f_c Eq. V.8	Q^f_{conv} Eq. V.17
Crucible	Zr		Q^{cr}_γ Eq. V.14	Q^{cr}_c Eq. V.8	

V.3.1 Fission Heating

The fission power released at time t in a fuel volume element dV at location $\vec{r}$, having the fuel density ρ can in general be expressed as:

$$q_{fis}(\vec{r},t)=h^{cal}_{fis} \cdot \frac{n_{pc}}{n_c} \cdot m^f_{pc} \cdot \frac{c^{pc}(\vec{r},t)\cdot i(t)\cdot \rho(\vec{r},t)}{\int_{t=0}^{\infty}\int_{\vec{r}} c^{pc}(\vec{r},t)\cdot i(t)\cdot \rho(\vec{r},t)\,dV\,dt} \qquad (V.11)$$

(Term: I II III IV)

where:

q_{fis} = fission power per unit volume (W/m^3)

h^{cal}_{fis} = total specific fission energy deposition in the calorimeter fuel (J/kg), as calculated from the integration of Eq. V.2:

$$= \frac{1}{m^f_{cal}} \int Q^f_{fis}(t)\,dt$$

n_{pc}/n_c = ratio of number of fissions in the pressure cell fuel to that in the calorimeter fuel as measured with fission product inventory analysis

m^f_{pc} = total mass of pressure cell fuel sample (kg)

c^{pc} = space and time dependent neutronic coupling factor of pressure cell fuel (W/kgA)

i = time dependent current of fission chamber (A), is a measure for the reactor power

There are four terms on the right hand side of Eq. V.11.
The products of these terms have the following physical meaning:

I x II = total specific fission energy deposition in the pressure cell fuel (J/kg), as deduced from the calorimeter measurement (Term I) and the fission product analysis (term II)

I x II x III = total absolute fission energy deposition in the pressure cell fuel sample (J)

IV = fission power density in dV (W/m^3)/ total absolut fission energy deposition in the pressure cell fuel (J).

I x II x III x IV = fission power density in volume element dV (W/m^3)

For the energy analysis of the pressure cell fuel it was assumed that the fuel density $\rho(\vec{r},t)$ is constant in time and space and that its value is equal to the initial fuel smear density in the fuel crucible (about 5300 kg/m^3). This important assumption is based on a number of experimental and theoretical informations, which uniquely show that the liquid fuel is violently agitated by existing pressure gradients and should therefore be distributed rather homogeneously throughout the EEOS crucible volume during energy deposition times. An experimental indication for this is e.g. the fact that after EEOS experiments the fuel was always coating the crucible walls as a high density layer of uniform thickness. Obviously there was no gravity driven draining of liquid fuel. The most probable way for the formation of such a uniform fuel crust appears to be the slow freezing of a contineously moving vapor/liquid mixture.

It also should be noted that in the EEOS experiments, the pressure cell fuel maintained the initial homogeneous powder density for roughly 50% of the total experiment time, until the melt temperature was reached.

A constant fuel density implies that the coupling factor c^{pc} in Eq. V.11 is independent of time, it therefore suffices to estimate its space dependence. From the PATH results shown in Fig. III.7 a volumetric average was calculated and used as the one-dimensional coupling factor $c^{pc}(x)$. With constant fuel density and time independent coupling factor the absolut fission energy deposition rate into the volume element dV of area A and thickness dx becomes

$$Q^{f}_{fis}(x,t) = q_{fis}(x,t)\cdot dV \quad \text{(Watt)}$$

$$= h^{cal}_{fis} \cdot \frac{n_{cp}}{n_c} \cdot m^{f}_{pc} \cdot \frac{c^{pc}(x)\,dx}{\int_{x=0}^{x_e} c^{pc}(x)\,dx} \cdot \frac{i(t)}{\int_{0}^{\infty} i(t)\,dt} \qquad \text{(V.12)}$$

Eq. V.12 is used in REAP to evaluate the fission energy deposition into pressure cell fuel nodes.

V.3.2 Gamma Heating

The gamma heating of the pressure cell fuel is very close to that of the calorimeter fuel because gamma shielding from the pressure cell crucible and from the calorimeter body are

a) small in magnitude (a few percent of the incident gamma flux) and
b) canceling each other to a large degree.

The gamma heating of a pressure cell fuel node I is therefore evaluated by scaling Eq. V.4 with the ratio of fuel masses:

$$Q_\gamma^{f,I}(t) = Q_\gamma^f(t) \cdot \frac{m_{pc}^I}{m^f} \qquad (V.13)$$

where

$Q_\gamma^f(t)$ = gamma heating of calorimeter fuel as given in Eq. V.4, (W)

m_{pc}^I = mass of pressure cell fuel node I (kg)

m^f = total mass of calorimeter fuel (kg)

The gamma heating of the zircalloy crucible node K is calculated from the measured gamma heating of the calorimeter body using an analogeous equation:

$$Q_\gamma^{cr,K}(t) = Q_\gamma^{cb}(t) \cdot \frac{m_{pc}^K}{m^{cb}} \qquad (V.14)$$

where

$Q_\gamma^{cb}(t)$ = gamma heating of calorimeter body (W)

m_{pc}^K = mass of crucible node K (kg)

m^{cb} = mass of calorimeter body (kg)

V.3.3 Conduction

Conduction in the pressure cell fuel and crucible is modeled with the equation given for the calorimeter calculation (Eq. V.8).

V.3.4 Convection

As already discussed in Section V.3.1 the liquid pressure cell fuel moves within the crucible volume during the reactor pulse. Therefore a term for convective energy transport must be included in the modeling, which is expressed in Eq. V.1 as $\rho \frac{\partial}{\partial x}(vh)$. The velocity v represents a mean fuel velocity component vertical to the crucible wall. It is assumed that each liquid fuel node exchanges energy with the neighboring nodes by exchanging liquid with the velocity v.

The effective velocity v was estimated in two steps:

1. The one-dimensional momentum equation for incompressible flow in the form of Eq. V.15 was solved for the simple case of a uniform but time dependent pressure gradient $\partial p(t)/\partial x$ in the fuel region.

$$\frac{\partial v}{\partial t} + v \frac{\partial v}{\partial x} + \frac{1}{\rho} \cdot \frac{\partial p}{\partial x}(t) - \frac{1}{\rho} \cdot \mu \frac{\partial^2 v}{\partial x^2} = 0 \qquad (V.15)$$

where

v = fuel velocity (m/s)
x = coordinate (m)
ρ = density (kg/m^3)
μ_{eff} = effective fuel viscosity (Pa.s)

The result for v_o, the maximum fuel velocity in the center of the fuel region is:

$$\frac{dv_o}{dt} = -\frac{8\mu_{eff}}{\rho L^2} \cdot v_o + \frac{C}{\rho} \cdot \frac{\partial p}{\partial x}(t) \qquad (V.16)$$

where

L = thickness of fuel region (in 1-dim. model),
C = fit parameter, introduced to describe slip between driving vapor pressure and liquid fuel empirically.

The first term in Eq. V.16 describes the slowing down of the fuel movement due to friction within the fuel and with the crucible walls. The second term represents fuel acceleration due to pressure gradients in the fuel. The pressure gradient can be calculated for each time of the experiment from the known energy gradient in the fuel and the iteratively determined p(h) relation.

2. Eq. V.16 was used as theoretical basis for fitting the pressure decay measured in the experiment. The free fit parameters μ_{eff} and C are evaluated from the agreement of measured and calculated pressure decay, as shown e.g. in Fig. VI.13.

The described semi-empirical approach for the evaluation of conductive heat losses relies on the experimental fact that the backside of the pressure pulse is mainly determined by the convective heat losses. The two other terms in Eq. V.1, namely fission heating and conduction, are much smaller during these times. Fig. VI.15 shows e.g. that the prompt pulse heating is finished roughly at the time of peak pressure.

In summary the model equation for the convective energy transport in the liquid fuel node I is

$$Q_{conv}^{f,I}(t) = \rho\ A\ v_o\ \ (h^{I+1}-h^I)-(h^I-h^{I-1}) \qquad (V.17)$$

where

ρ = fuel density (kg/m^3)
A = fuel node cross section (m^2)
v_o = effective fuel velocity for convective energy transport (m/s), evaluated by integrating Eq. V.16
h^j = specific enthalpy of fuel in node j (J/kg)

The convective model was extended for description of the experiments EEOS-08 and EEOS-09 in which some melting of the zircalloy walls occurred. Due to the high coupling factor of the plutonium containing test sample, liquid fuel came into direct contact with the crucible walls. In the other experiments a fuel crust developed very shortly after the first fuel melting, shielding the walls against high heat fluxes. The heat of melting of Zr (266 kJ/kg) and its subsequent heating in a Zr/fuel mixture provides a fast acting and effective internal heat sink, because there is no need for transporting energy out of the closed system.

The heat loss from liquid fuel to solid Zr was described using an empirical Stagnation Heat Flux correlation for fluids impacting an ablating solid /V.1/. The conduction heat transfer to the molten Zr was estimated with an equation analogeous to Eq. V.8.

V.5 Error Assessment

In the following error assessment it was assumed that the individual errors are statistically independent and that the standard deviations may therefore be added according to Eq. V.19.

For many of the quantities i entering the error analysis, there was not enough statistically significant information to define a true standard deviation σ_i. In these cases the value used for σ_i represents a rough estimate for the 70% confidence interval.

V.5.1 Enthalpy Evaluation

The enthalpy of the pressure cell fuel in a node at location x and at time t results practically completely from fission heating. Gamma heating during the prompt pulse is only about 1% of the fission heating and can therefore be neglected in the error assessment.

The accumulated fission energy deposition into a pressure cell fuel node at location x and time t follows from Eq. V.12:

$$h^{pc}_{fis}(x,t) = h^{cal}_{fis} \cdot \frac{n_{pc}}{n_c} \cdot m^{f}_{pc} \cdot \frac{c^{pc}(x)dx}{\int_{x=0}^{x_e} c^{pc}(x)dx} \cdot \frac{\int_0^t i(t)dt}{\int_0^\infty i(t)dt} \qquad (V.18)$$

$$A = B \cdot C \cdot D \cdot E \cdot F$$

where

A = total specific enthalpy content in pc fuel node at time t, (kJ/kg)

B = total specific enthalpy of calorimeter fuel, (kJ/kg)

C = ratio of number of fissions induced in pressure cell fuel and calorimeter fuel, resp.

D = total mass of pressure cell fuel, (kg)

E = ratio of fission energy deposition into pressure cell fuel at node x to that into total pressure cell fuel (fraction in space)

F = ratio of fission energy deposition delivered at time t to the total energy delivered by ACRR pulse (fraction in time)

The standard deviation in A then follows from

$$\frac{\sigma_A}{A} = \left[\left(\frac{\sigma_B}{B}\right)^2 + \left(\frac{\sigma_C}{C}\right)^2 + \left(\frac{\sigma_D}{D}\right)^2 + \left(\frac{\sigma_E}{E}\right)^2 + \left(\frac{\sigma_F}{F}\right)^2\right]^{1/2} \qquad (V.19)$$

The individual standard deviations (s.d.) are as follows:

1. $$\frac{\sigma_B}{B} = \left[\left(\frac{\sigma_{cp}}{cp}\right)^2 + \left(\frac{\sigma_{\Delta T}}{\Delta T}\right)^2\right]^{1/2}$$

$\frac{\sigma_{cp}}{cp}$ = relative s.d. of the heat capacity of calorimeter body, made from aluminum = 1%

$\frac{\sigma_{\Delta T}}{\Delta T}$ = relative s.d. of measured calorimeter temperature increase

$$= \left[\left(\frac{\sigma_{T_o}}{T_o}\right)^2 + \left(\frac{\sigma_{T_{max}}}{T_{max}}\right)^2\right]^{1/2} = (.5^2 + .5^2)^{1/2} \% = .7\%$$

2. $$\frac{\sigma_c}{C} = \left[\left(\frac{\sigma_{co}}{n_{co}}\right)^2 + \left(\frac{\sigma_{ss}}{f_{ss}}\right)^2\right]^{1/2}$$

$\frac{\sigma_{co}}{n_{co}}$ = relative s.d. in number of 1.6 MeV counts n_{co} measured in fission product inventory analysis =1%

$\frac{\sigma_{ss}}{f_{ss}}$ = relative s.d. of calculated gamma self shielding correction factor (value was .989) = .5%

3. The uncertainty in the total mass of the pressure cell fuel was at the most

$$\frac{\sigma_D}{D} = .1\%$$

4. The relative coupling factor $c^{pc}(x)$ varied in the calculations from .982 at x=0 to 1.025 at x=.8 mm. From the energy deposition studies described in Section III.4 these values may have uncertainties of $\pm$ .02, so that

$$\frac{\sigma_E}{E} = 2\%$$

5. In the energy analysis it is assumed that the fission chamber current is proportional to the reactor power. There is no obvious reason for a deviation between actual reactor power and i(t) on the millisecond time scale, hence

$$\frac{\sigma_F}{F} = 0.$$

With these individual standard deviations the result for the enthalpy is

$$\frac{\sigma_A}{A} = 2.60\%.$$

To account somewhat for possible addional errors, e.g. from the 1-dimensional modeling of (small) heat losses, the total standard deviation in the enthalpy values was set to ± 3%.

In experiments EEOS-08 and 09 also some Zr melting was modeled. The uncertainty in the fuel enthalpy from this process was estimated to another ± 3%, giving a total error of ± 4.2%.

This rather small value is only possible due to two quite precise measurements: that of the calorimeter temperature and that of the ratio of fissions in calorimeter and pressure cell. The other important fact keeping σ_A small, is the flat energy deposition profile in the pc fuel sample.

V.4.2 Pressure Evaluation

The pressure transducers were calibrated with a hydraulic press by loading the transducer membrane via a simulant piston and an original aluminum adapter (see Fig. II.1) and measuring the output voltage. The p-V characteristic was reproducible within about ± .3MPa.

During the EEOS tests it was realized that the particular position of the transducer cables within the 8 m deep ACRR central cavity, could cause a random zero shift in the transducer output, corresponding to about ± .25 MPa. This effect is thought to be due to slight changes in the cable capacitance, which is sensed by the high frequency signal conditioning electronics.

In the calculation of the net pressure, the time scale of the experiment shot had to be corrected to that of the background shot, in order to perform the necessary substration. The uncertainty in the time scale adjustment may have caused addional errors in the net pressure of about ±.1 MPa.

To account for other possible deviations between measured and actual pressure, a somewhat more conservative error bound of $\pm$ .5 MPa was used in defining the error band in the final p-h curves (e.g Fig. VI.12).

VI. TEST RESULTS

VI.1 Test Matrix

The following tests were conducted within the EEOS program:

- two experiments using ultra pure UO_2 powder,
- two experiments using powder prepared from reactor grade UO_2 pellets, and
- two experiments using powder from reactor grade $(U,Pu)O_2$ pellets.

Two tests of each type were performed to check the reproducibility of the results. The vapor pressure from ultra pure UO_2 was thought to serve as a baseline against which the vapor pressure from other fuels could be compared. The reactor grade UO_2 was investigated to see if the typical impurities which are present from the fabrication process in nuclear fuels would contribute noticeably to the vapor pressure of pure UO_2. The two experiments on reactor-grade (U,Pu) mixed-oxide were intended to compare its saturation vapor pressure with that of reactor typical UO_2. If they were identical the much more extensive vapor pressure data basis of UO_2 could be used for the mixed oxides also.

VI.2 Discussion of Tests

In this section examples of measured signals, results of data analysis, and individual events of the six EEOS experiments are discussed.

VI.2.1 Experiment EEOS-04

The fuel in EEOS-04 was ultrapure UO_2 (see Section IV.4). Since

EEOS-04 was the first scoping experiment and in view of the large uncertainties in measured p-h-relations (see Fig. VII.4) a relatively low energy input was choosen.

In the background shot, the calorimeter contained a lead sample to measure the gamma heating of fuel, which is very close to that of lead.

The calorimeter temperatures measured in the background shot and the fueled experiment are shown in Fig.VI.1. The temperature rise in the background shot consists of the prompt gamma heating at the time of the reactor pulse (.3s) and the subsequent delayed gamma heating from decaying core fission products. The cooling of the fueled calorimeter was significantly larger than expected. It is probably due to helium gas which leaked from the inner cannister into the evacuated calorimeter case. Each point along the curves marks the average temperature of the five thermocouples at the respective time.

The measured average temperature points are compared to the calculated temperature curves in Fig. VI.2. The mean deviation of measured and calculated temperatures in the experiment shot is .74 K ($t \geq 4s$), using $1.539.10^7$ kW/kg A and .438 for the neutronic coupling factor in Eq. V.2 and the conductivity factor α in Eq. V.9, respectively.

The reactor pulse was monitored with a fission chamber in the ACRR core. (A second fission chamber was installed in the reactor pool for redundancy.) The fission chamber signal was multiplexed and recorded with different amplifier gains and sampling frequencies. Fig. VI.3 shows the prompt reactor pulse (low gain, 40 kHz) and Fig. VI.4 the pulse tail (high gain, .4 kHz). For the data analysis REAP combines both data sets into one file, corrects for zero shifts and performs a smoothing procedure. Fig. VI.5 gives an example for the resulting fission chamber signal.

The pressure signals of background and experiment shot (Fig. VI.6) are processed by adjusting both pulses to the same zero time, smoothing both pressure signals and calculating the difference, which gives the net pressure signal p(t) required for the data analysis (marked line in Fig. VI.6). In experiment EEOS-04 the pressure transducer was prestressed to 2 MPa by an unintended small mismatch in fabrication tolerances. The vapor pressure was therefore only recorded after it exceeded 2 MPa and had separated the piston from the crucible.

The measured pressure-enthalpy relation is depicted in Fig. V.7. Due to the relatively low energy input and the prestressed transducer, only the pressure range from about 2.5 to 8 MPa was covered in EEOS-04. The 1-σ error limits are estimated to $\pm$ 3% in enthalpy and .5 MPa in pressure, giving the shaded band in Fig. V.7.

VI.2.2 Experiment EEOS-05

The fuel in experiment EEOS-05 was again pure UO_2 to check reproducibility of the EEOS-04 results. A larger reactor pulse was choosen to increase energy deposition and to cover a larger part of the saturation vapor pressure curve. On the other hand the calorimeter was shielded with more cadmium than in EEOS-04 to avoid overpressurization of the calorimeter body, therefore the calorimeter reached about the same temperature maximum as in EEOS-04 (Fig. VI.8). The measured average temperatures could be fitted by REAP calculations to within .53K (Fig. VI.9). The energy analysis yielded the following results for the calorimeter fuel sample (at 2 sec):

fission energy deposition	2642.5 kJ/kg
gamma heating	39.4 kJ/kg
beta heating	31.4 kJ/kg .

The second step in the data analysis is calculation of the space and time dependent enthalpy of the pressure cell fuel using the model described in Section V.3. Fig. VI.10 shows the results obtained for EEOS-05:

- Heat losses from the solid powder (up to times about .30865s) are very small.
- After fuel melting convection of liquid fuel noticeably increases the heat transfer to the cold zirconium wall, as can be seen from the much flatter slope dh/dx in the cooled region of the fuel for t>.30865 s.
- The peak energy node migrates inwards as the cooling front proceeds, but there remains an unquenched adiabatically heated core of liquid fuel for all of the energy deposition period.
- Maximum fuel enthalpy in EEOS-05 was 3337.$\pm$100 kJ/kg, which corresponds to about 7500K.

The third step in data analysis is evaluation of the net pressure and its correlation with the calculated peak enthalpy as function of time. The pressure signal of the background and of the experiment shot is shown in Fig. VI.11. The measured net pressure reached 33 MPa. The correlation of the front part of the pressure pulse with the peak enthalpy values of the heat-up phase (Fig. VI.10) yields the pressure-enthalpy curve shown in Fig.VI.12.

In the final p-h curve, the pressure information is essentially the result of a simple pressure substraction, whereas the enthalpy information involves an energy deposition and transfer model. The energy deposition part of the model is mainly based on the calorimeter and the fission product inventory results (h_{fis}^{cal} and n_{pc}/n_c in Eq. V.12). The energy transfer part of the model is dominated by liquid fuel motion and evaluation of the governing quantity v_o (Eq. V.17) is again based on experimental information, namely the backpart of the pressure pulse. Fig. VI.13 shows that the pressure cell model quite nicely describes the measured pressure decay. It should be noted that the heat transfer only determines where along an adiabatic line in Fig.VI.10 the peak energy node is located. Heat losses were never so severe that the total fuel sample was quenched (for t<.3200s).

Another result lending confidence to the energy evaluation came from the pressure signal in EEOS-05 (Fig. VI.14). Expansion of the solid fuel powder caused a pressure signal before any vapor was generated. This pressure should decay at the moment of first fuel melting. The observed pressure collapse coincides indeed with the calculated time of first fuel melting (= time when the first fuel node reaches 1115 J/g). The data indicate that the energy evaluation is correct within $\pm$ 5% or better.

Fig.VI.15, which compares the time relation between fission chamber current and pressure transducer voltage, demonstrates the nearly adiabatic nature of the EEOS-experiments by the fact that the pressure does increase for almost the full duration of the prompt energy deposition. At the time of the peak pressure the energy deposition rate was only few percent of the maximum heating rate. Since at this time the energy deposition and loss rates should be equal, it can be estimated from Eq. V.12 that the heat losses must have been around 10 kW at .32s. Fig. VI.15 further demonstrates that significant loss of liquid fuel from the crucible can be excluded.

VI.2.3 Experiment EEOS-06

Experiment EEOS-06 utilized fuel powder which was prepared from conventionally fabricated UO_2 pellets. The known impurity contents are given in section IV.4.

The measured calorimeter temperatues are presented in Fig. VI.16. The temperature decay is much slower than in EEOS-04 and -05 and close to the theoretically expected cooling curve of the calorimeter. Probably much less helium leaked into the evacuated calorimeter in the case of EEOS-06.

The measured average temperatures are compared to the calculated calorimeter temperatures in Fig. VI.17. The calorimeter energy data resulted in the pressure cell enthalpies shown in Fig. VI.18. The pressure cell fuel reached a maximum enthalpy of 3163$\pm$95 kJ/kg.

The corresponding maximum net pressure amounted to 19.6 MPa (Fig.VI.19). In experiment EEOS-06 a very sudden pressure excursion started at .3165 seconds (Fig. VI.20). The pressure transducer signal exhibited a short oscillation and then stabilized at a rather constant pressure before following the advancing pressure excursion in the test volume. The most probable cause for this event is a slight pressure seat of the piston in the crucible. The piston got loose at about 3 MPa internal pressure. From thereon the piston was free to move, as indicated by the damped oscillation. (The very fast osciallation was not fully resolved by the 40 kHz sampling rate).

The pressure-enthalpy curve of experiment EEOS-06 is depicted in Fig. VI.21. It should be emphasized that only the part of the curve above about 3.5 MPa represents a saturation vapor pressure measurement, the lower pressures are the result of a delayed piston excursion.

VI.2.4 Experiment EEOS-07

The fuel in experiment EEOS-07 was again powder prepared from reactor-grade UO_2 pellets.

The measured calorimeter temperatures in Fig. VI.22 indicate rather large temperature gradients in the calorimeter body during the first seconds. Especially the central thermocouple registers high temperatures. The markers in Fig.VI.22 again represent the average temperature of all thermocouples at a given time. These average temperatures are compared to the REAP calculations in Fig. VI.23, the mean deviation being .56 K (for t>5s).

The calculated enthalpies of the pressure cell fuel are plotted in Fig. VI.24. The fuel reached 3038 ± 92 kJ/kg or about 6500 K. The measured pressure signal of background and experiment shot can be seen from Fig. VI.25. The experiment shot exhibited a very early oscillation event the cause of which became not clear. At this time about 1/4 of the prompt reactor pulse has passed. There is practically no net pressure increase during the following 5 ms, although a significant energy deposition occurs during this time intervall, raising the fuel enthalpy to about 2000 kJ/kg. The piston seems to be bonded to the crucible up to about .311 seconds, then shortly attains a constant value and finally follows the full pressure excursion up to 15.8 MPa of net pressure.

The pressure-enthalpy curve measured in experiment EEOS-07 is shown in Fig. VI.26. Only the pressures above 1.3 MPa represent true vapor pressure data.

VI.2.5 Experiment EEOS-08

The test sample was fuel powder prepared from commercially fabricated (U,Pu) mixed-oxide pellets. The fissionable Pu-content was 20.3% of (U+Pu), the uranium was depleted.

The calorimeter temperatures measured with and without test fuel are plotted in Fig. VI.27 and the comparison with calculated temperatures is presented in Fig. VI.28. The energy deposition in EEOS-08 was somewhat higher then expected, leading to roughly 400 K temperature increase in the calorimeter.

The measured pressure is shown in Fig. VI.19 together with the small background signal. Early in the experiment there is again a pressure jump of about 1 MPa. Thereafter the pressure transducer monitors a smooth exponentially increasing transient up to 54 MPa where the amplifier saturated.

The energy analysis for the pressure cell fuel revealed that in this experiment - contrary to the previously described tests - some melting of the zircalloy curcible occurred. The reason is the significantly increased coupling factor of the plutonium containing fuel, which prevents freezing of liquid fuel on the cold crucible walls and leads to a large heat flux into the zircalloy. The heating and melting of zircalloy provides an effective internal heat sink because there is no need to transport the energy out of the fuel volume. The initially relatively cold liquid zircalloy mixes with the moving hot fuel and quickly attains a temperature close to the instantaneous fuel temperature. The modeling equations for this process are described in Section V.3. The addional uncertainties from this part of the energy evaluation were estimated to $\pm$ 3%, giving a statistied total uncertainty of 4.2% in fuel enthalpy.

The pressure-enthalpy curve resulting from correlation of net pressure and peak fuel enthalpy is shown in Fig. VI.30.

VI.2.6 Experiment EEOS-09

In EEOS-09 commercially fabricated (U,Pu) mixed-oxide was used as test fuel. The reactor pulse was choosen somewhat smaller than in EEOS-08, giving about 50 K less heating of the calorimeter (Fig. VI.31).

The pressure signal in experiment EEOS-09 (Fig. VI.32) showed a smooth increase up to about 26 MPa, then at .3106 s a sudden break in the slope and about .6 ms later again a sharp increase in pressure. It is thought that at .3106 s some liquid fuel extruded between the piston and the crucible and that after filling the available free volume outside the crucible (which was kept as small as possible) the transducer again monitored the pressure increase in the fuel sample. The increase is much steeper at this time because of the increased enthalpy of the fuel.

Experiment EEOS-09 was only evaluated up to 26 MPa. The resulting pressure-enthalpy relation is shown in Fig. VI.33.

Calorimeter Temperatures In EEOS-04

Measured Data

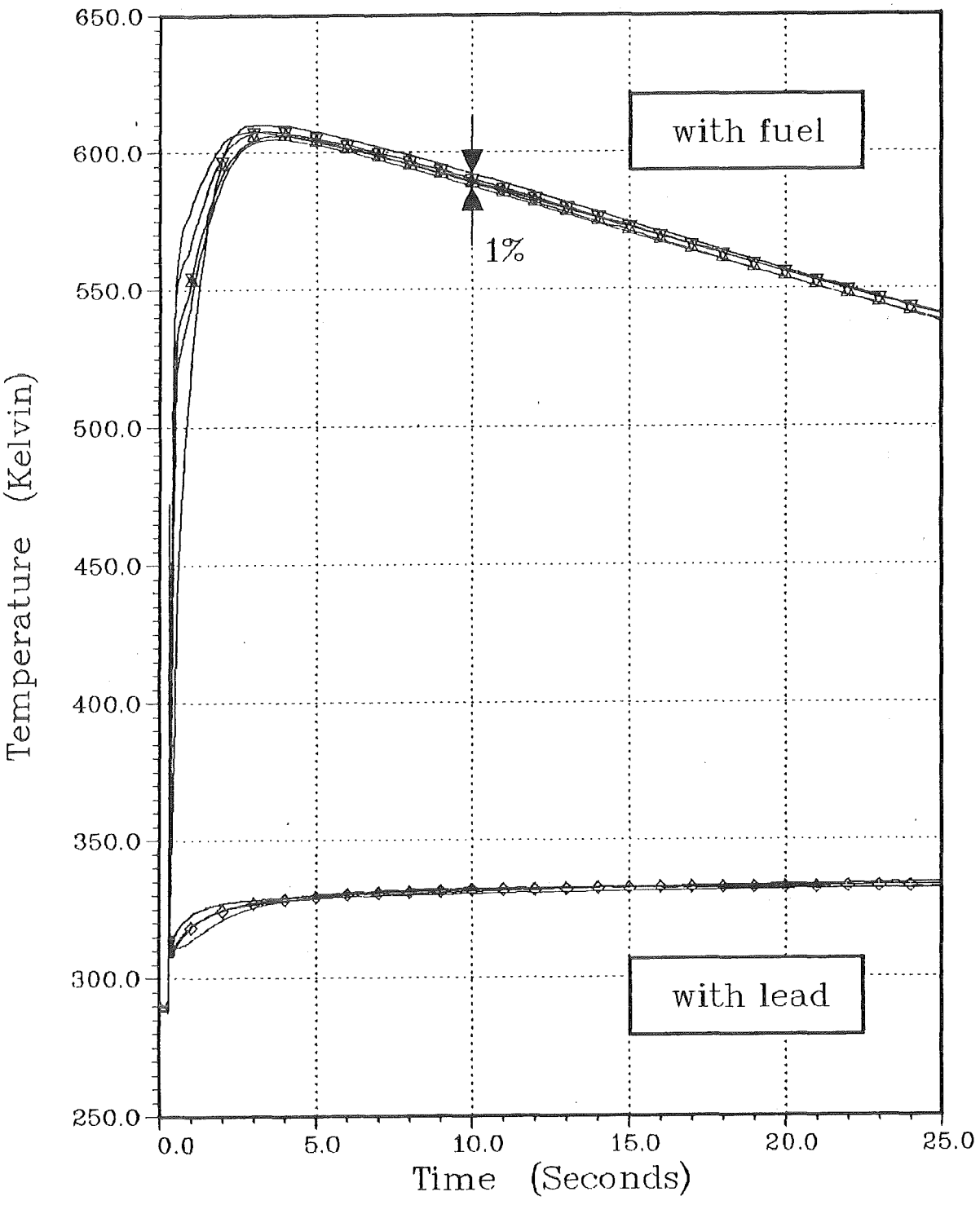

PLOT 1 16.30.52 WED 9 JAN, 1985 JOB=INR85810, KFK DISSPLA 9.0

FIGURE VI.1

Calorimeter Temperatures In EEOS-04

Measured Average and Calculated Data

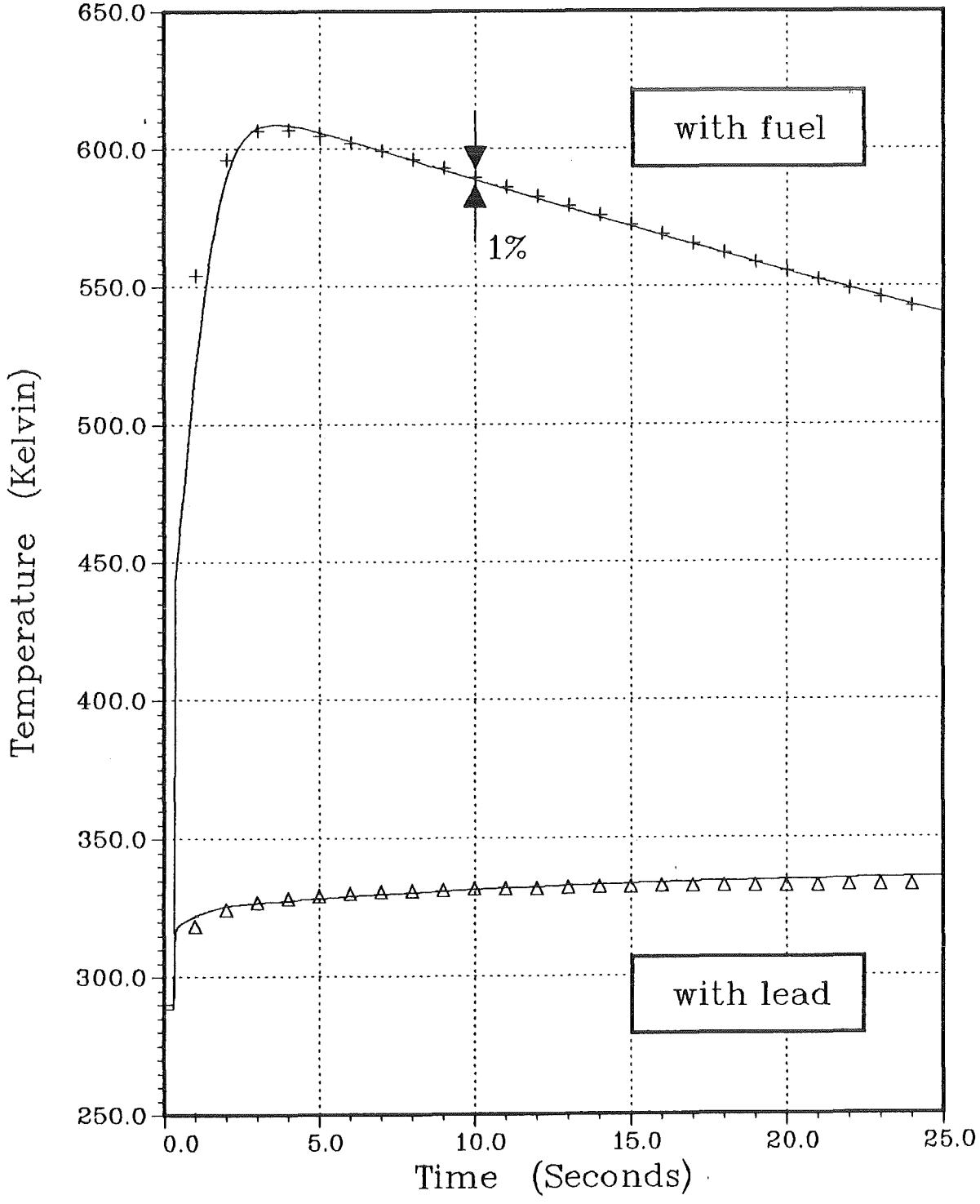

PLOT 1 12.12.08 THUR 10 JAN, 1985 JOB-INR858M2, KFK DISSPLA 9.0

FIGURE VI.2

coupl. factor = $1.539*10^7$
cond. factor = 0.438
deviation (K) = 0.74

Fission Chamber Signals in EEOS-04

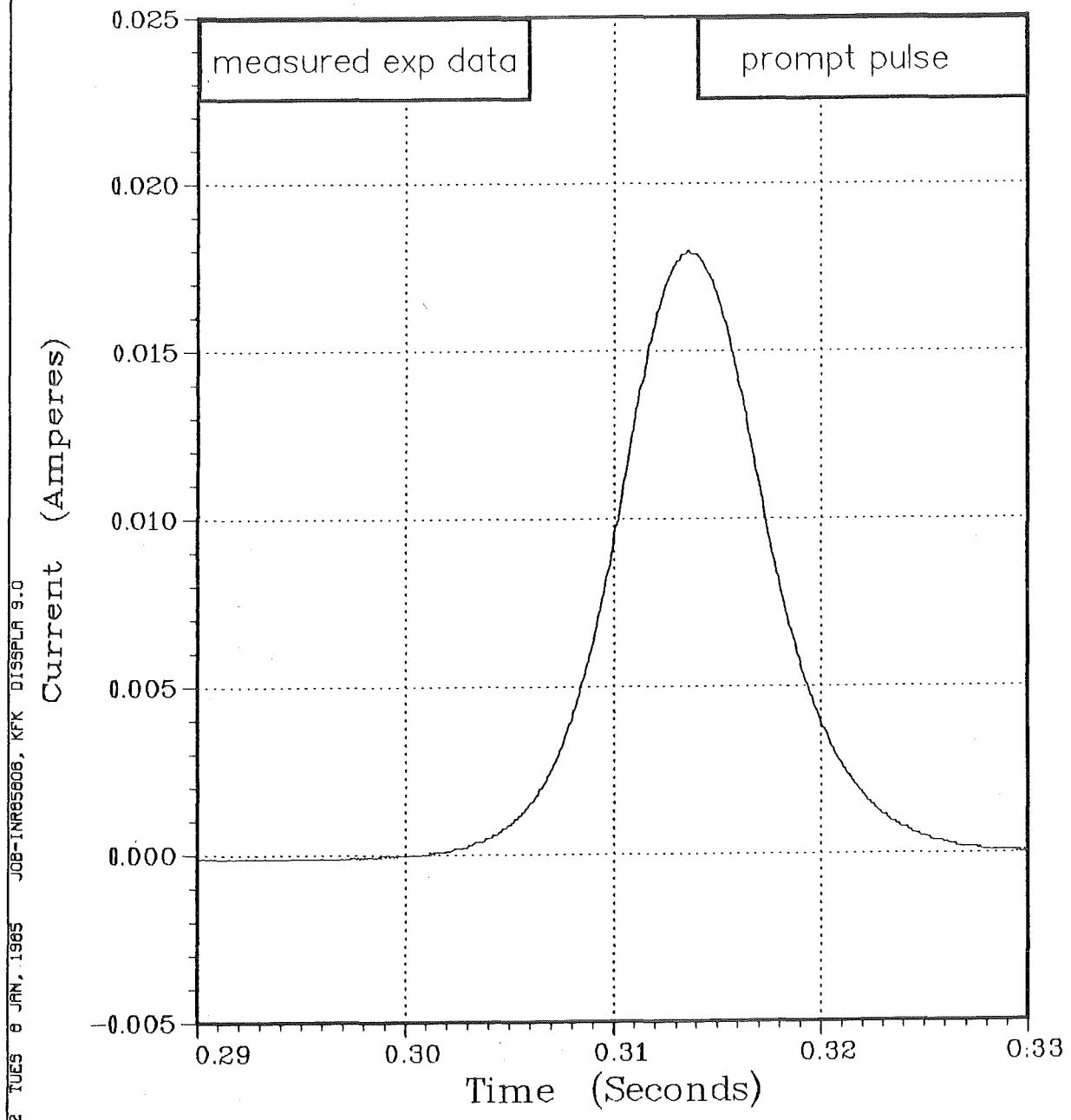

FIGURE VI.3

Fission Chamber Signals In EEOS-04

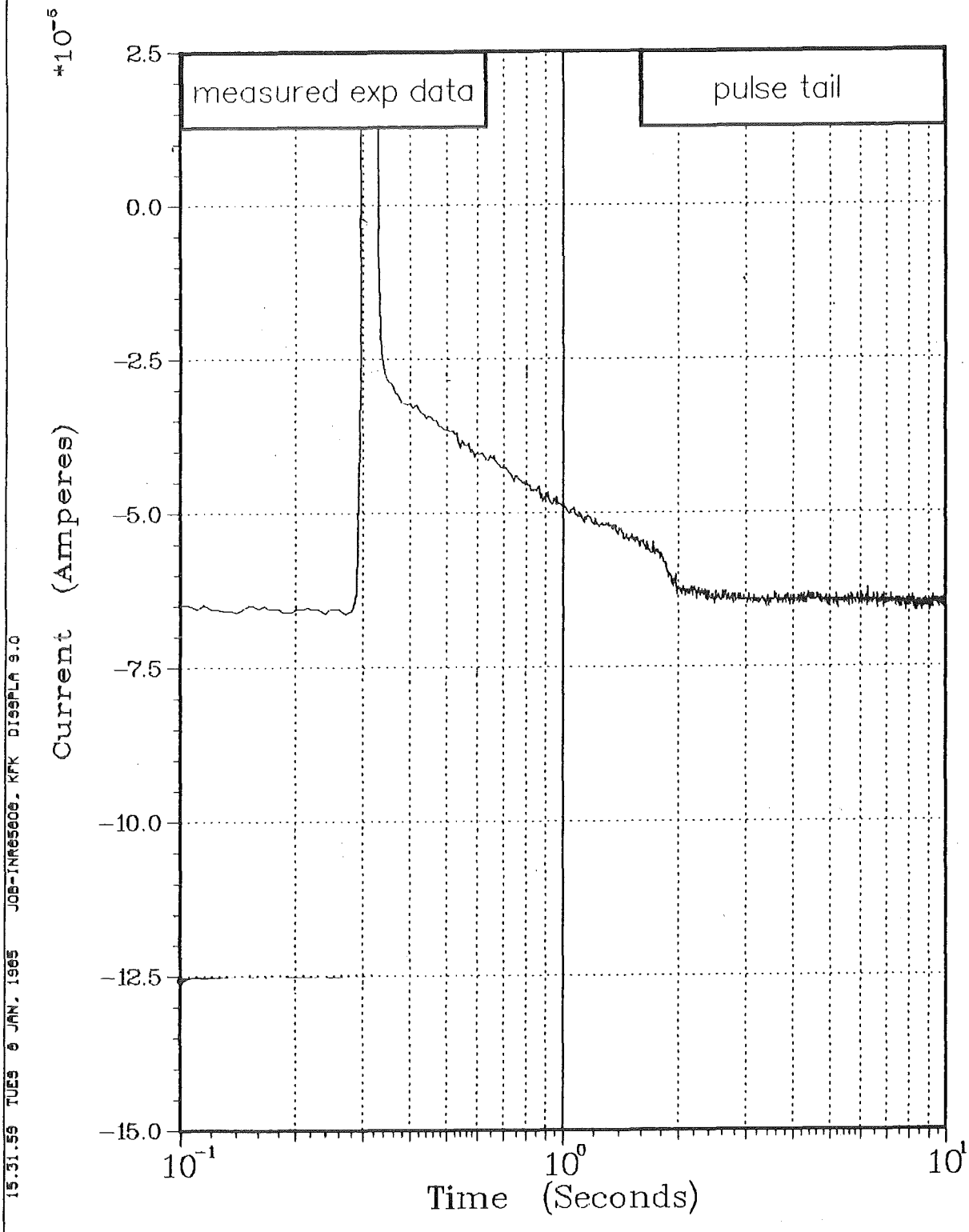

FIGURE VI.4

Fission Chamber Signals in EEOS-04

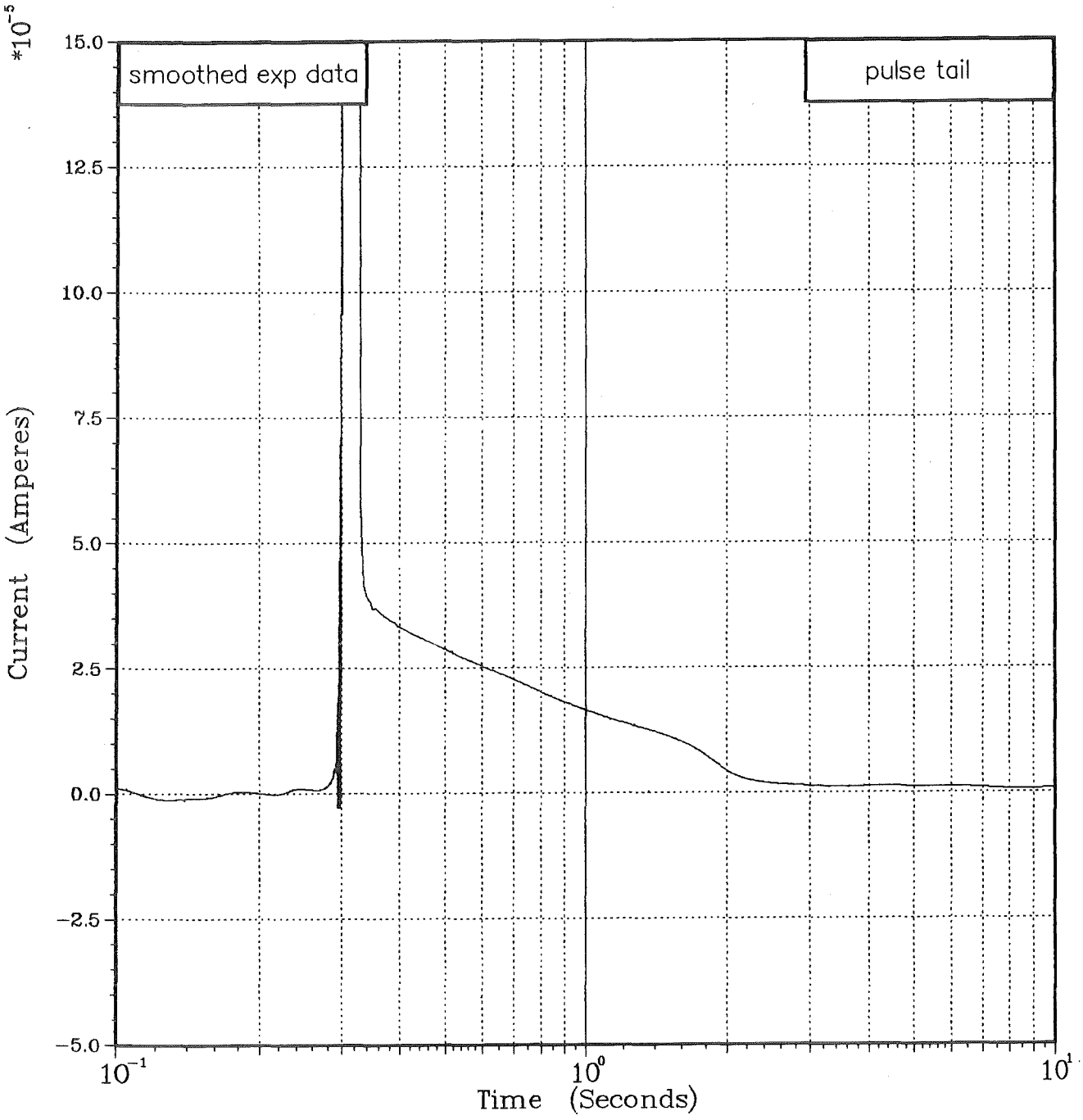

FIGURE VI.5

Pressure Signals in EEOS-04

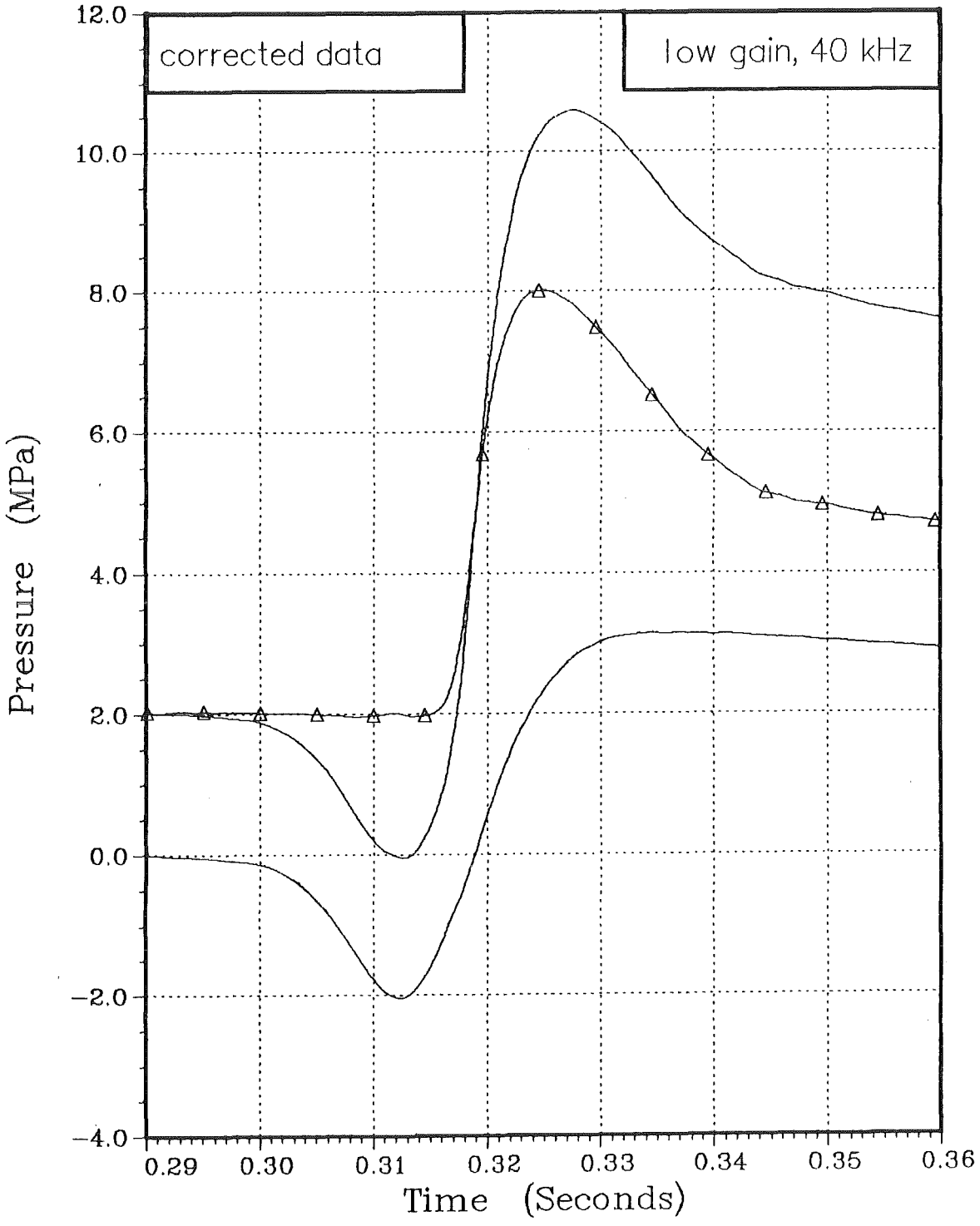

FIGURE VI.6

Pressure–Enthalpy Measurement

EEOS–Experiment 04

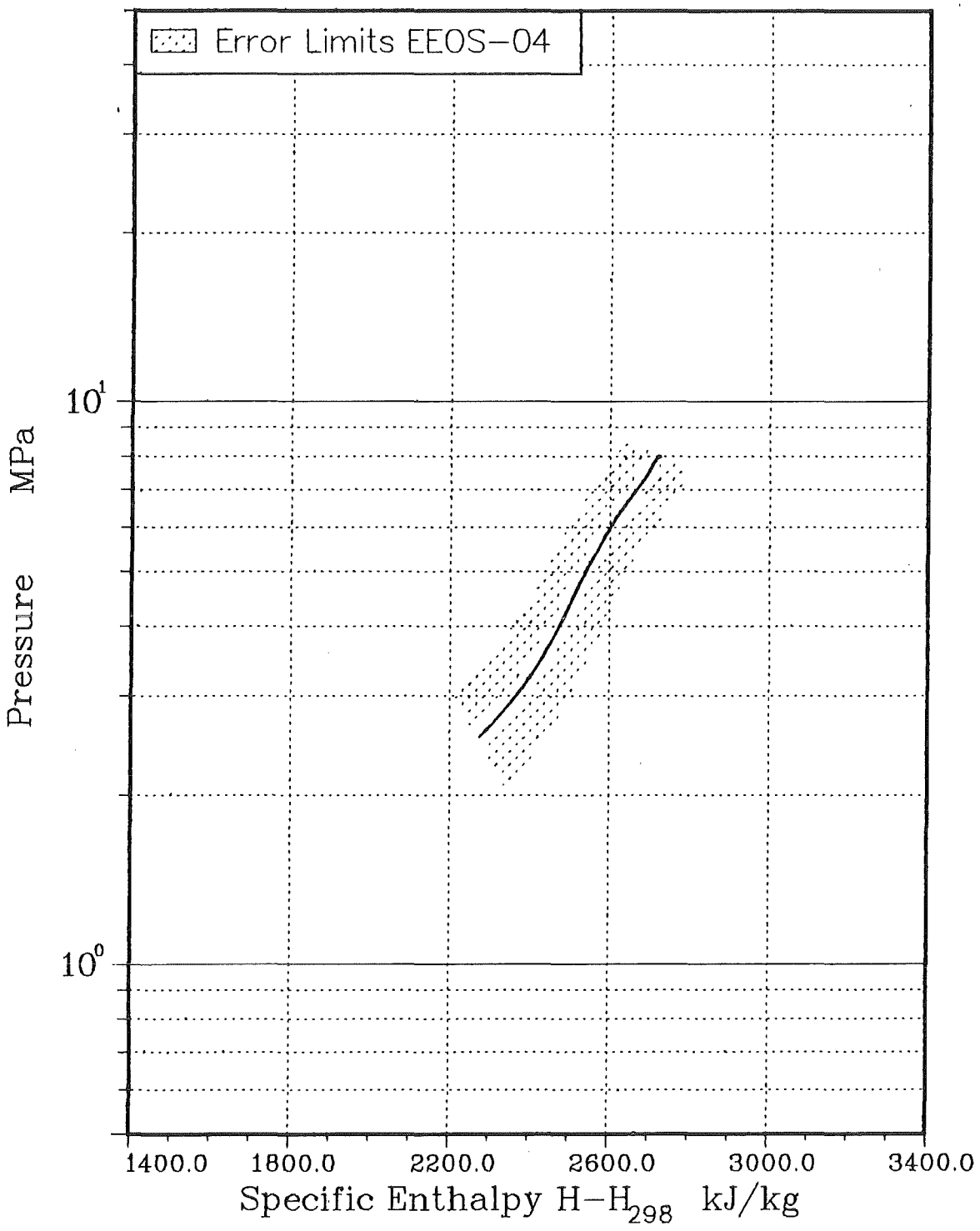

FIGURE VI.7

PLOT 3 13:28.25 MON 14 JAN, 1985 JOB-INR85BM3, KFK DISSPLA 9.0

Calorimeter Temperatures In EEOS-05

Measured Data

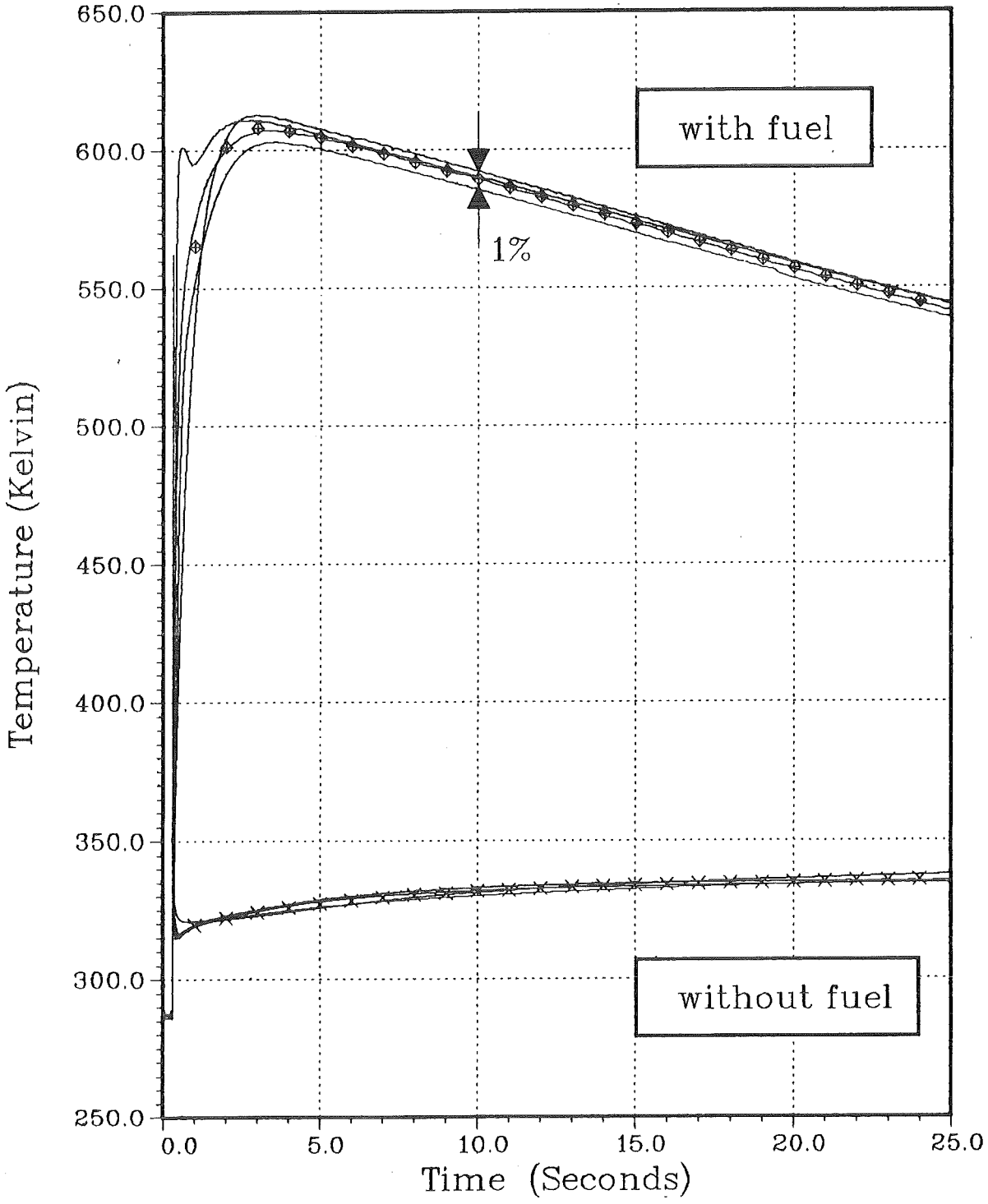

FIGURE VI.8

Calorimeter Temperatures In EEOS-05

Measured Average and Calculated Data

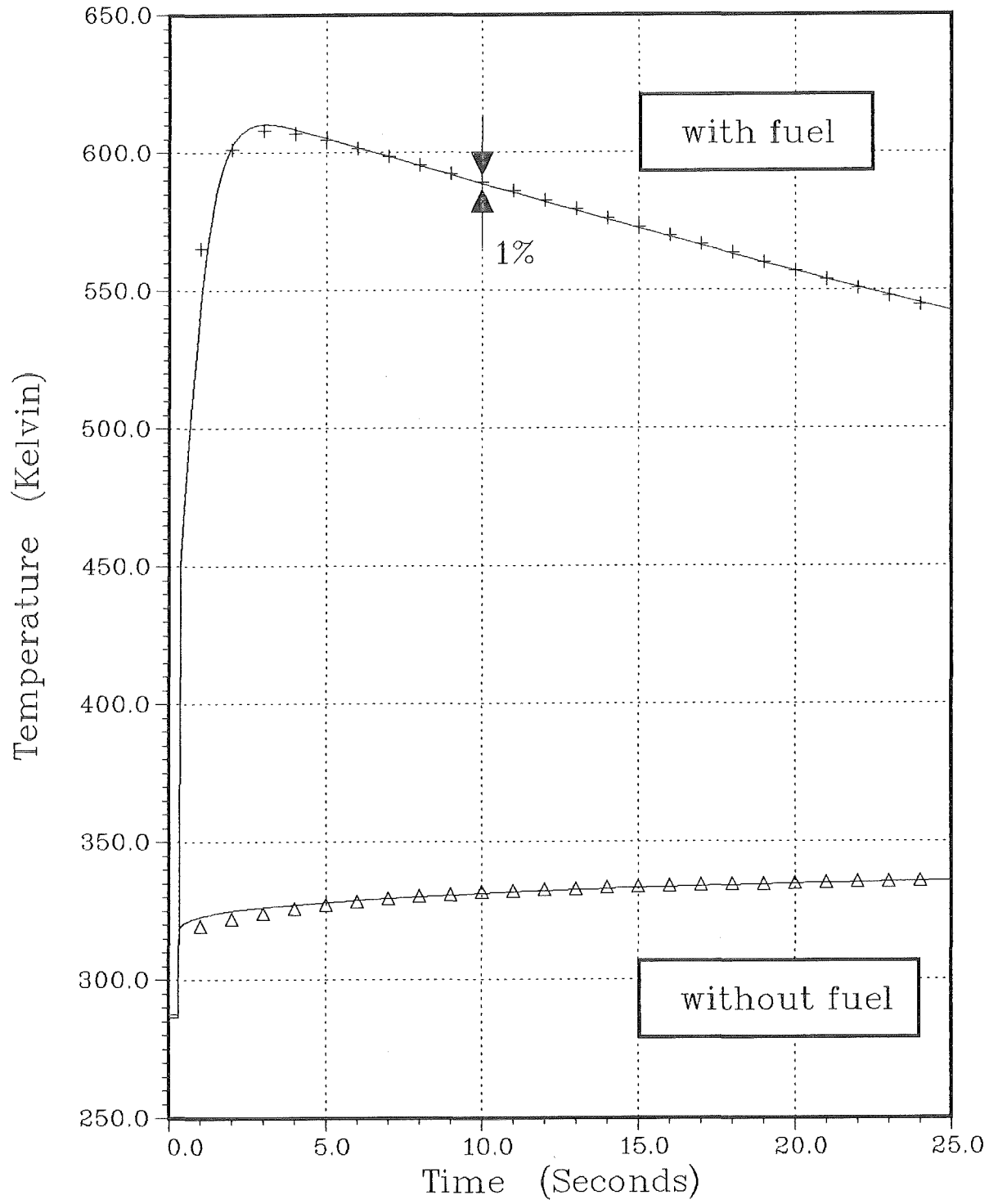

PLOT 1 11.02.45 FRI 4 JAN, 1985 JOB-INR858M2, KFK DISSPLA 9.0

FIGURE VI.9

coupl. factor = $1.268*10^{7}$
cond. factor = 0.410
deviation (K) = 0.53

Fuel Enthalpy in EEOS-05

Data of Heat-up Phase

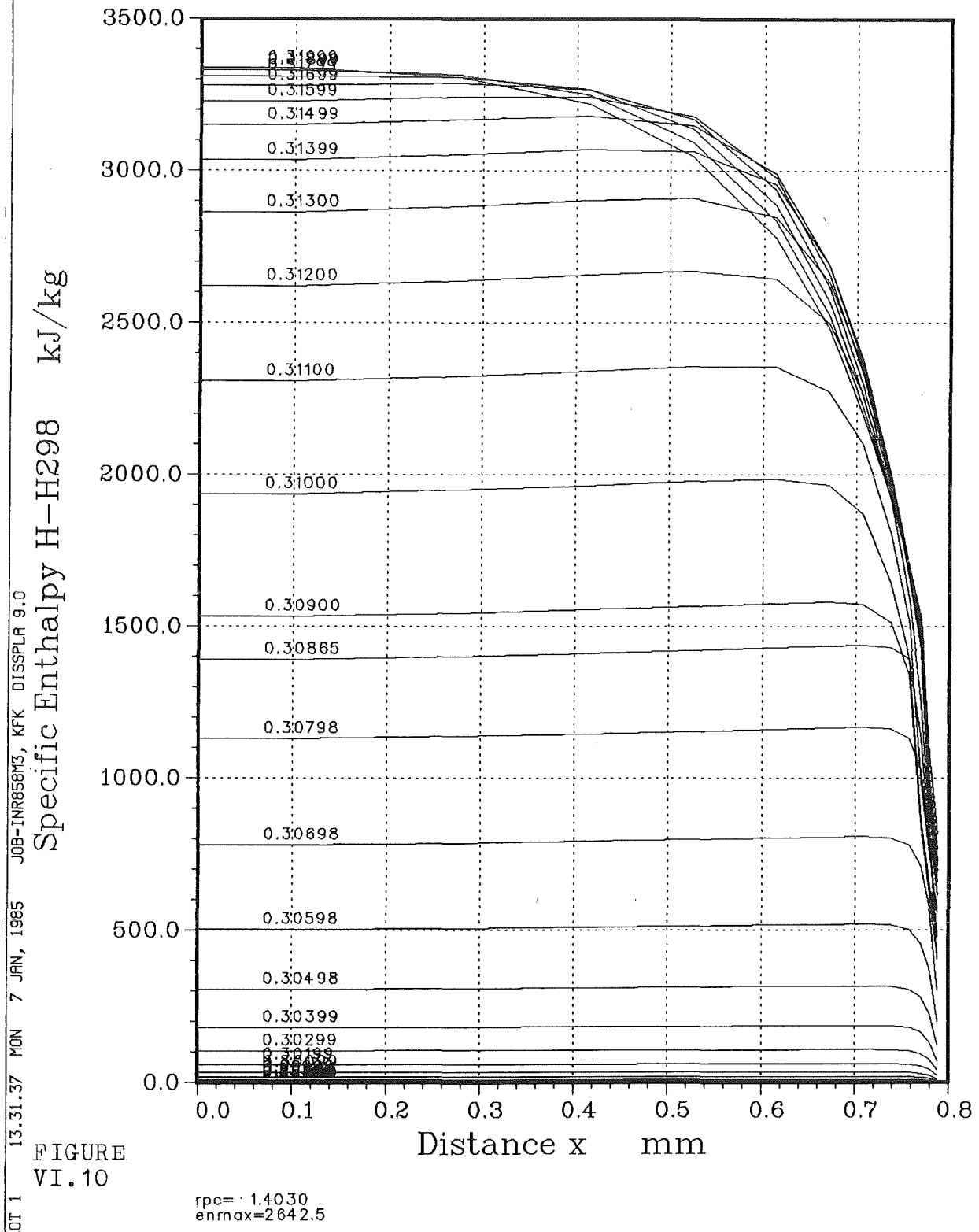

FIGURE VI.10

Pressure Signals in EEOS-05

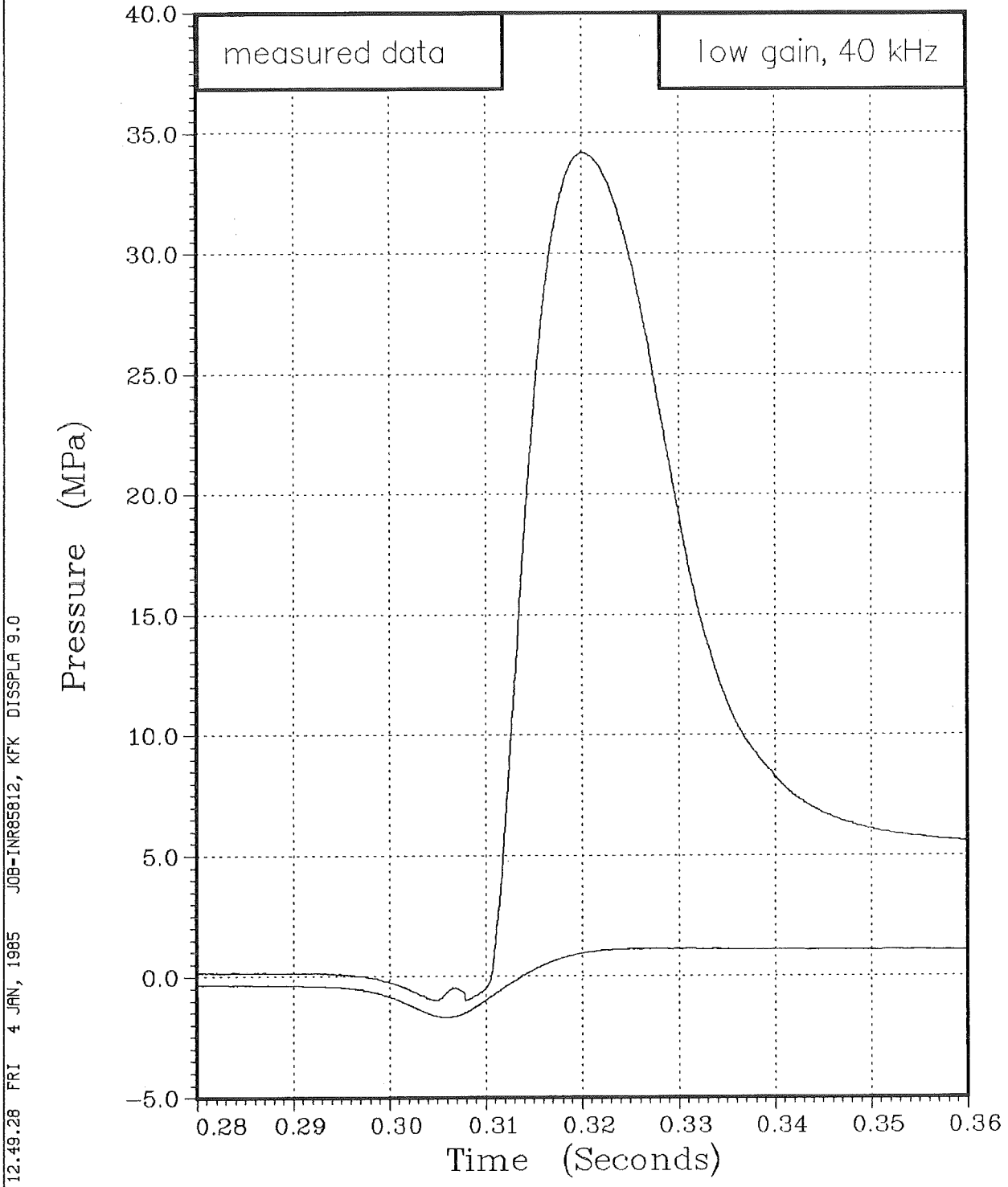

FIGURE VI.11

Pressure–Enthalpy Measurement

EEOS–Experiment 05

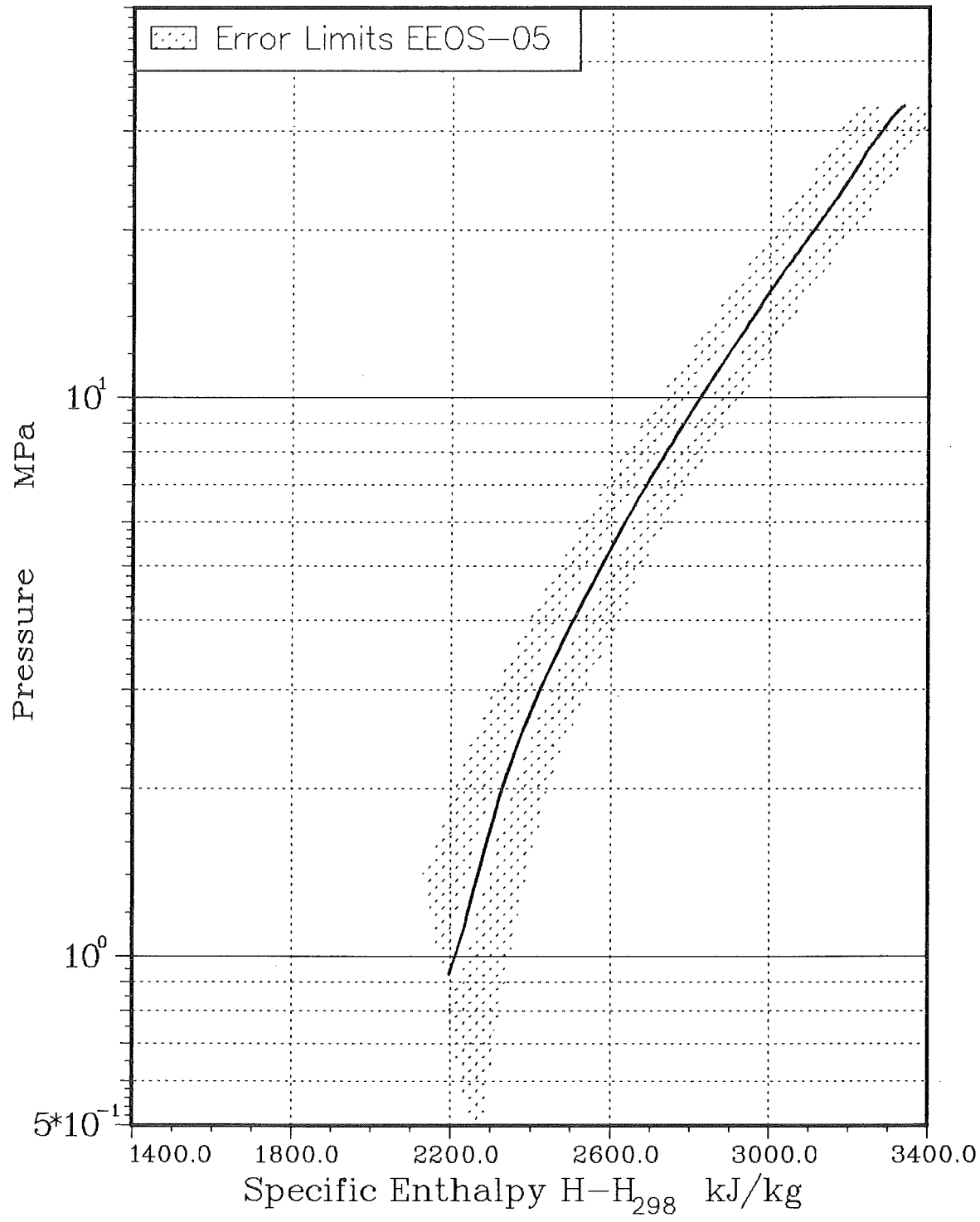

FIGURE VI.12

Pressure Signals in EEOS-05

Measured And Calculated Data

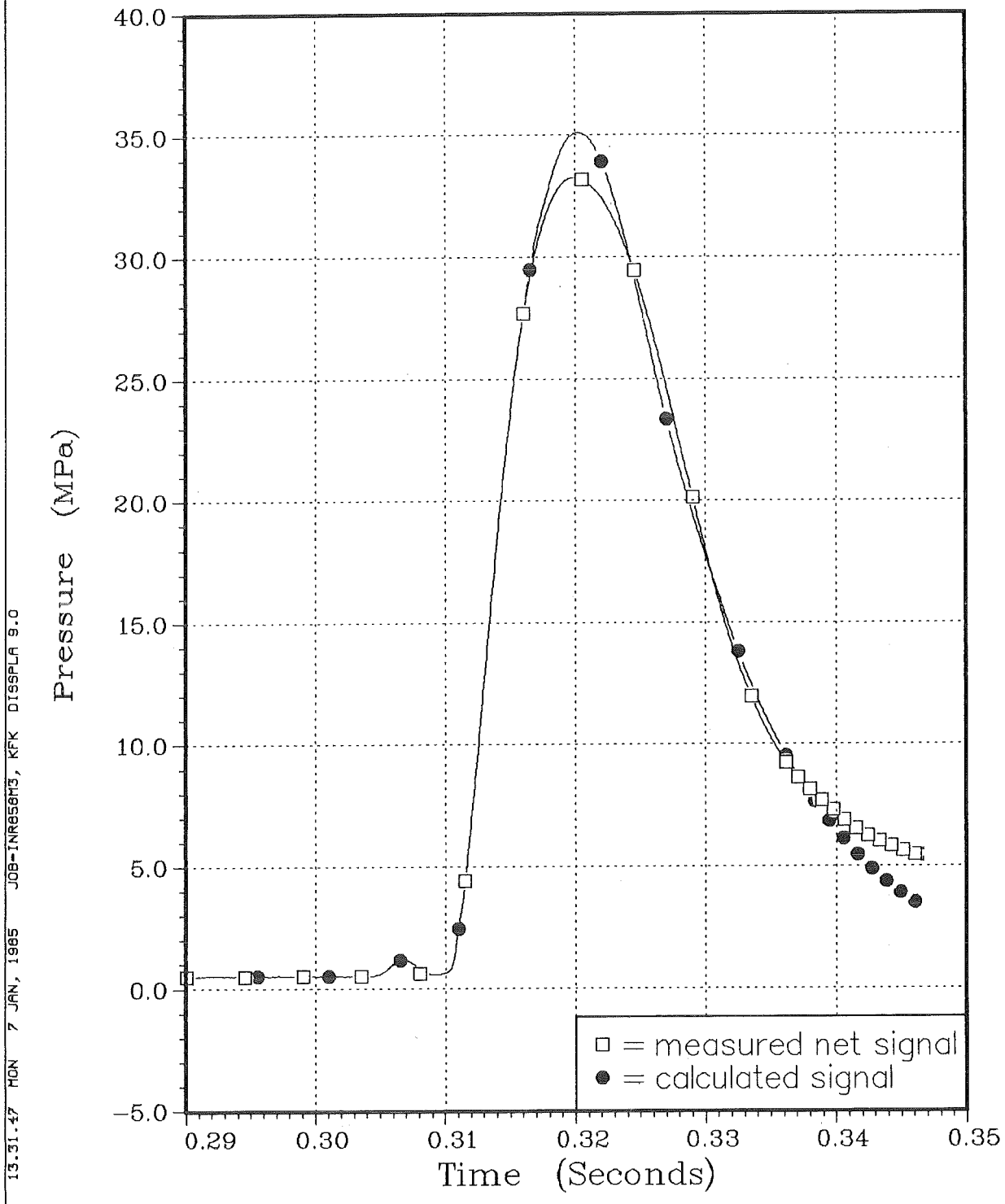

FIGURE VI.13

Pressure Signals in EEOS-05

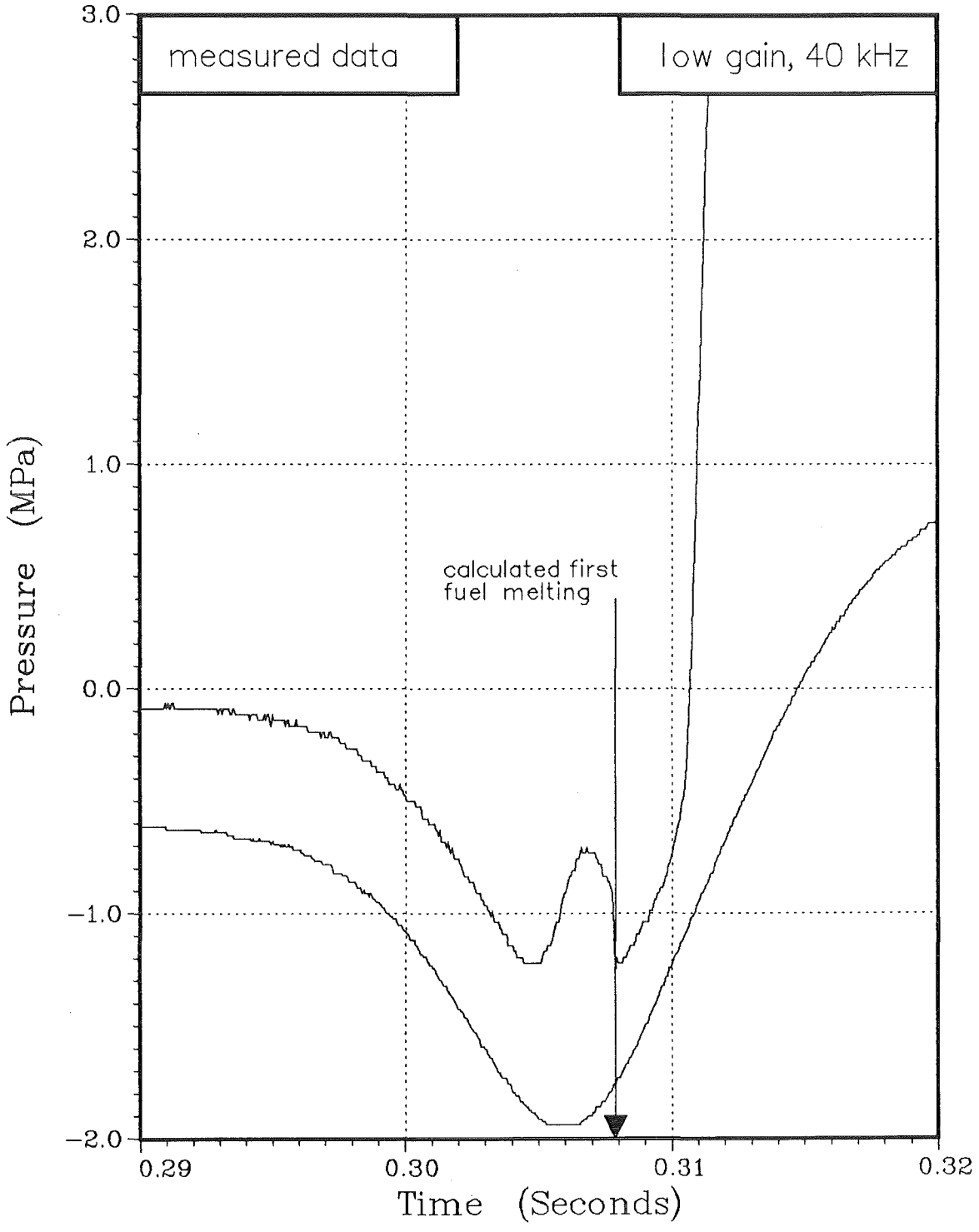

FIGURE VI.14

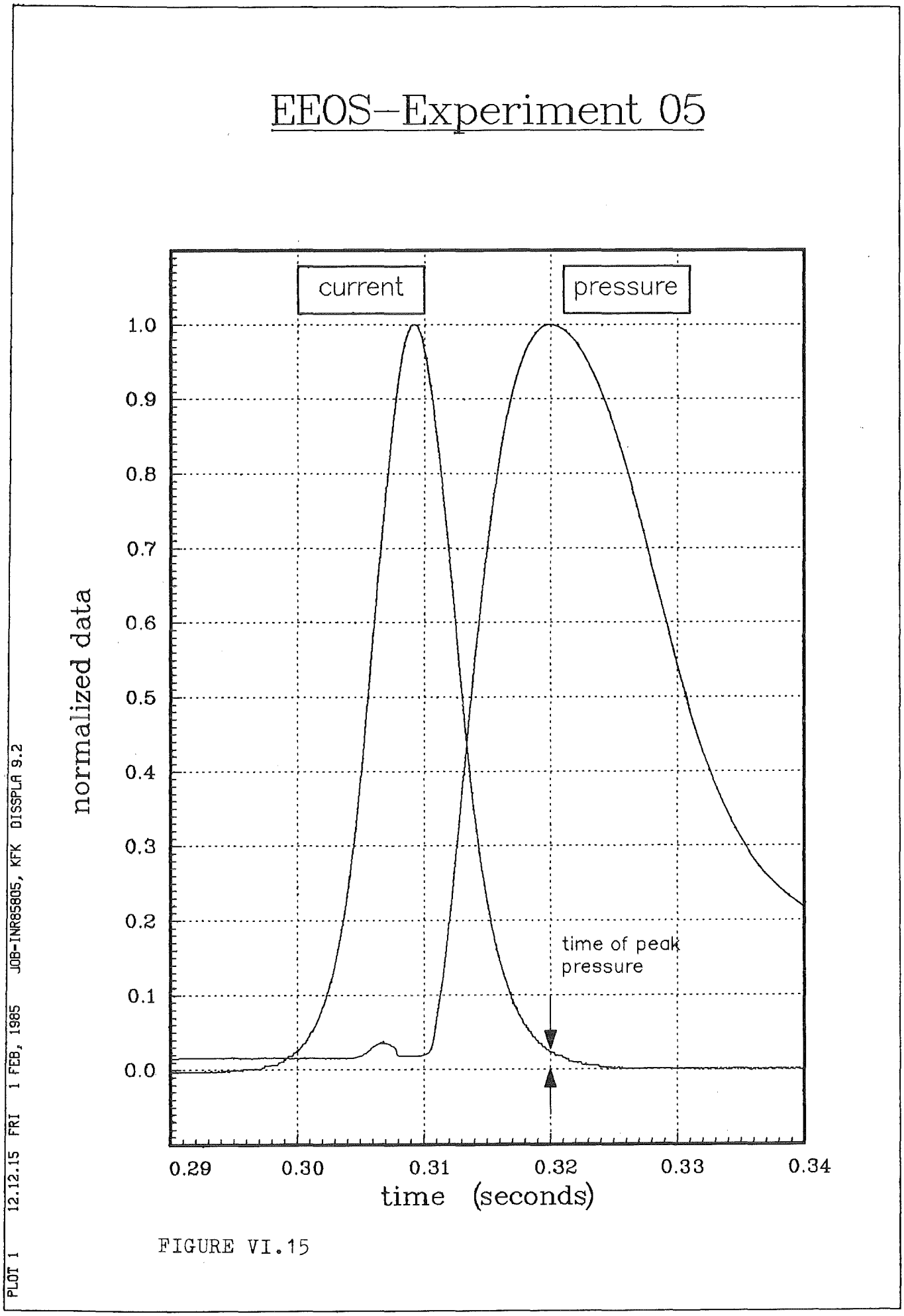
EEOS–Experiment 05
current
pressure
time of peak pressure
normalized data
1.0
0.9
0.8
0.7
0.6
0.5
0.4
0.3
0.2
0.1
0.0
0.29
0.30
0.31
0.32
0.33
0.34
time (seconds)
PLOT 1 12.12.15 FRI 1 FEB, 1985 JOB-INR85805, KFK DISSPLA 9.2

FIGURE VI.15

Calorimeter Temperatures In EEOS-06

Measured Data

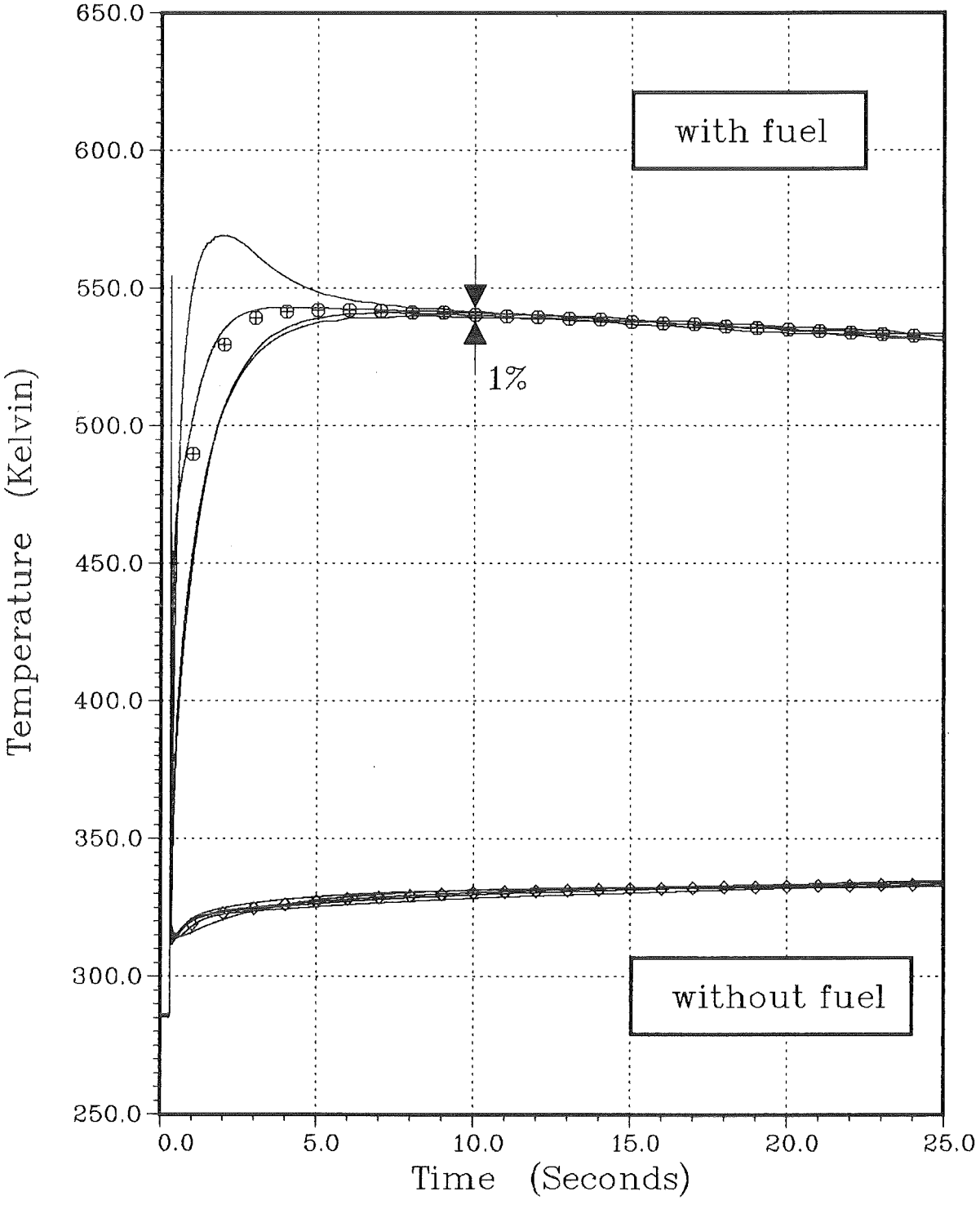

PLOT 1 11.21.34 WED 17 OCT, 1984 JOB-INR85801, KFK DISSPLA 9.0

FIGURE VI.16

Calorimeter Temperatures In EEOS-06

Measured Average and Calculated Data

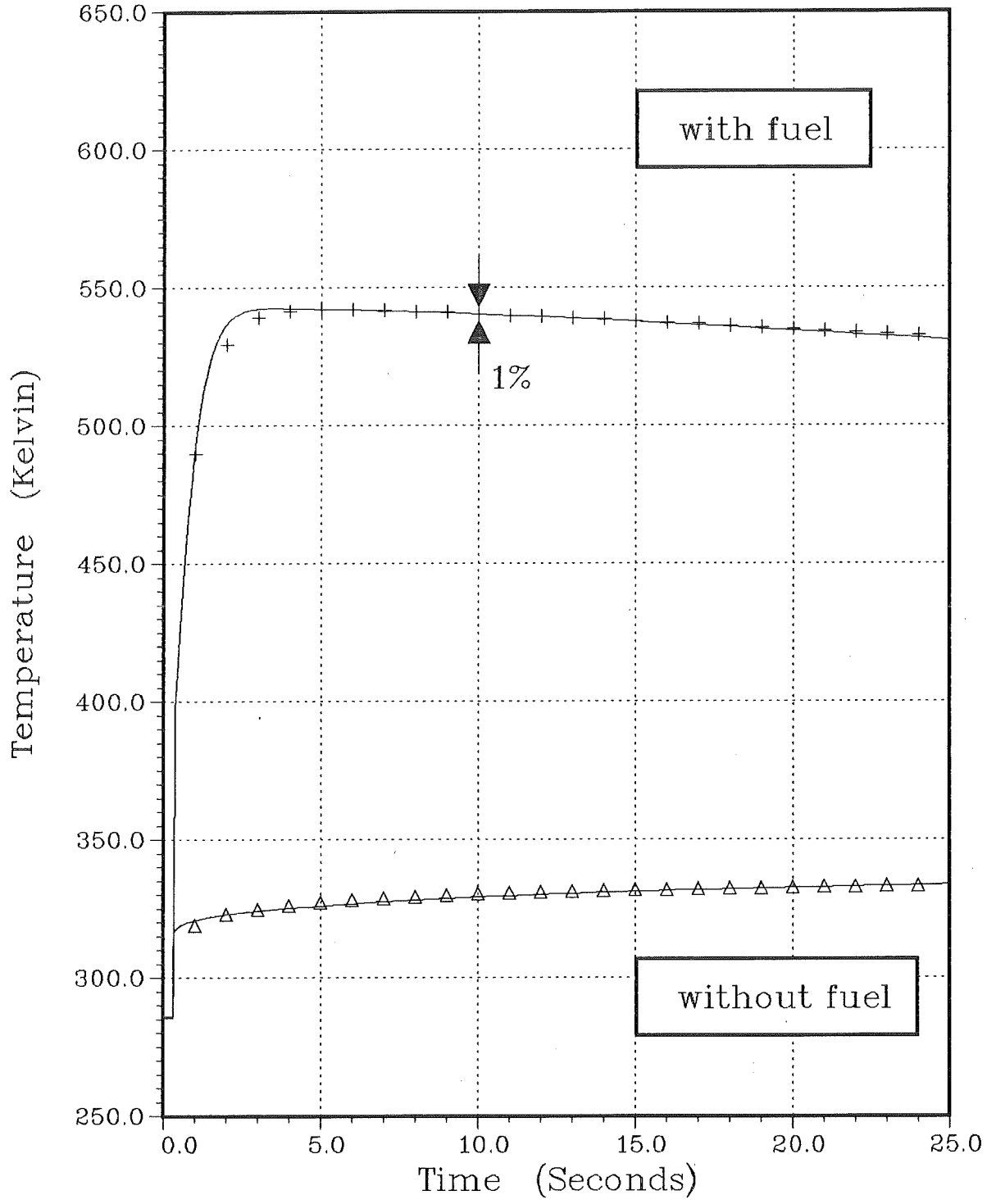

PLOT 1 12.59.37 WED 2 JAN, 1985 JOB-INR656M2, KFK DISSPLA 9.0

FIGURE VI.17

coupl. factor = $1.364*10^7$
cond. factor = 0.100
deviation (K) = 0.52

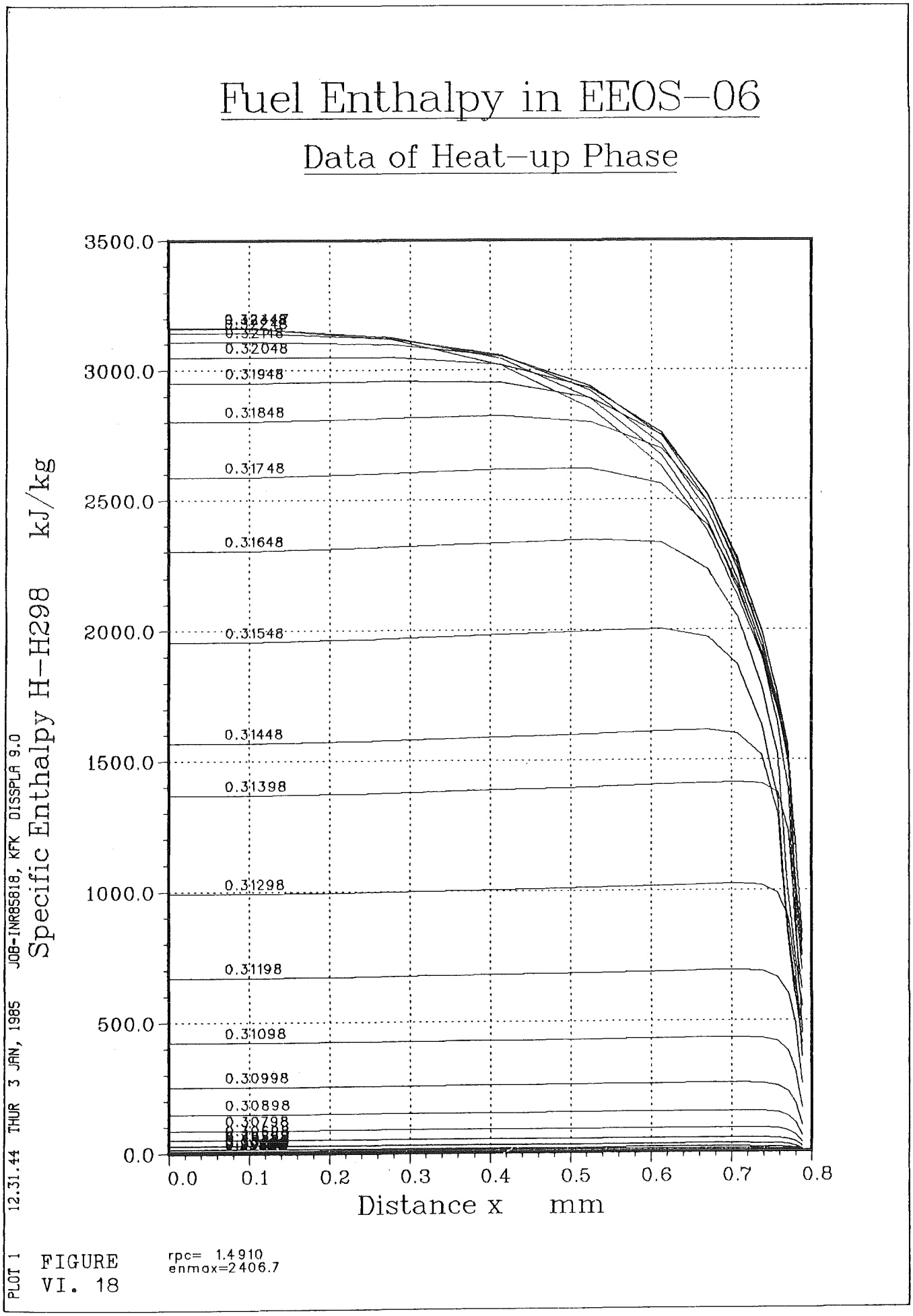
Fuel Enthalpy in EEOS-06
Data of Heat-up Phase
Specific Enthalpy H-H298 kJ/kg
Distance x mm
3500.0
3000.0
2500.0
2000.0
1500.0
1000.0
500.0
0.0
0.0
0.1
0.2
0.3
0.4
0.5
0.6
0.7
0.8
0.32048
0.31948
0.31848
0.31748
0.31648
0.31548
0.31448
0.31398
0.31298
0.31198
0.31098
0.30998
0.30898
PLOT 1 12.31.44 THUR 3 JAN, 1985 JOB-INR85818, KFK DISSPLA 9.0
rpc= 1.4910
enmax=2406.7

FIGURE VI. 18

Pressure Signals in EEOS-06

Measured And Calculated Data

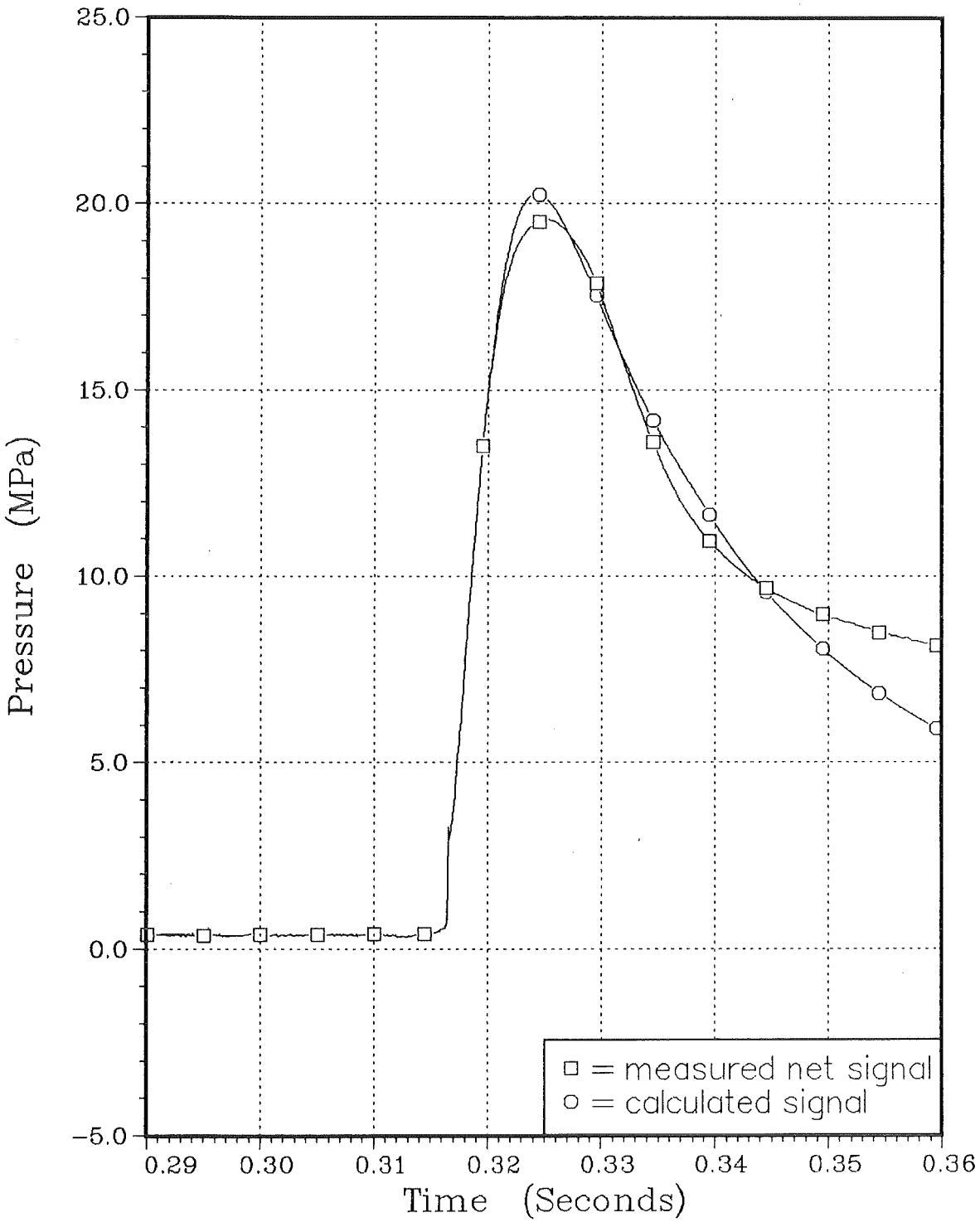

PLOT 1 12.31.57 THUR 3 JAN, 1985 JOB-INR85610, KFK DISSPLA 9.0

FIGURE VI.19

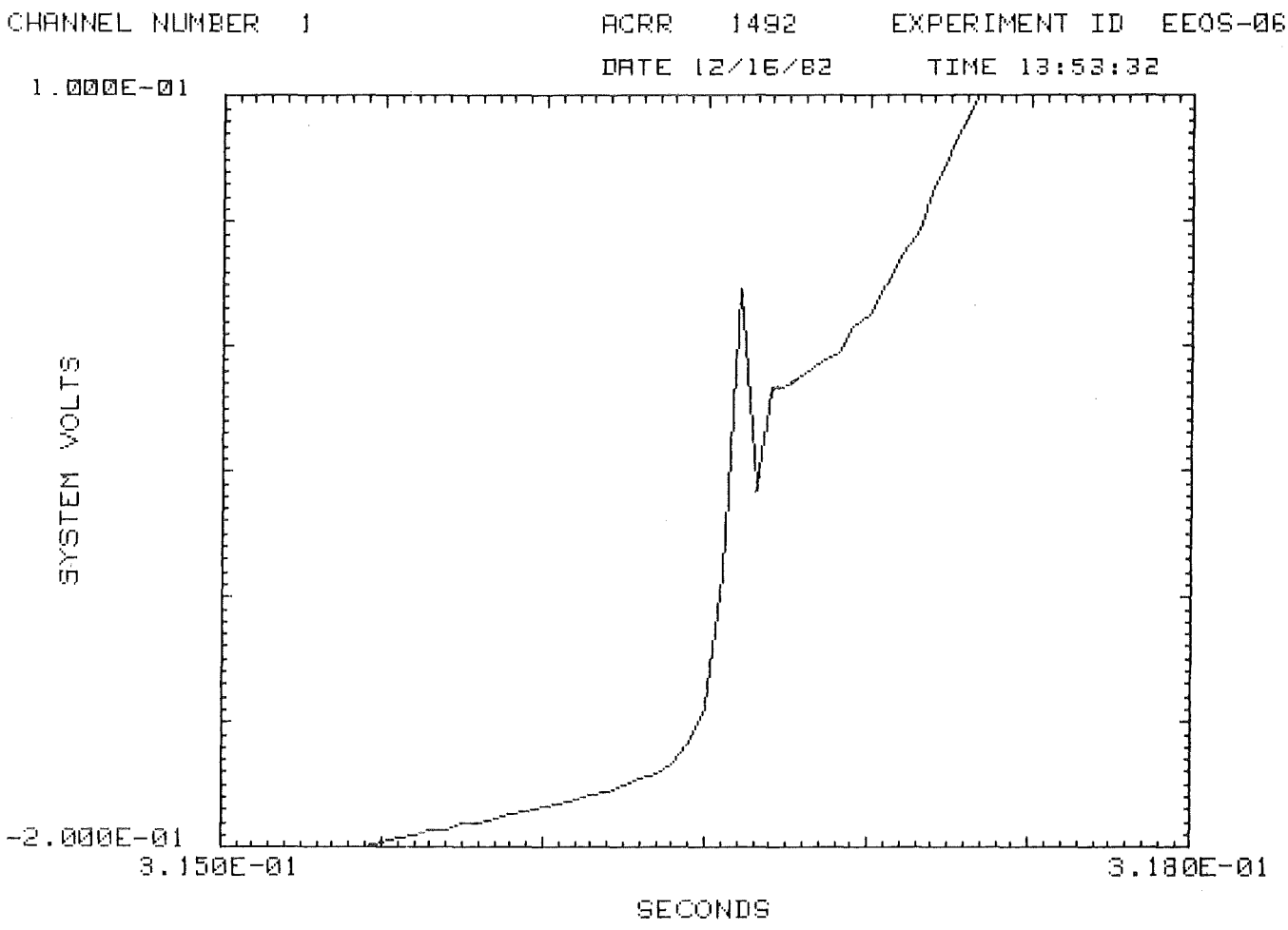

FIGURE VI. 20 Oscillation of pressure transducer in experiment EEOS-06

Pressure–Enthalpy Measurement

EEOS–Experiment 06

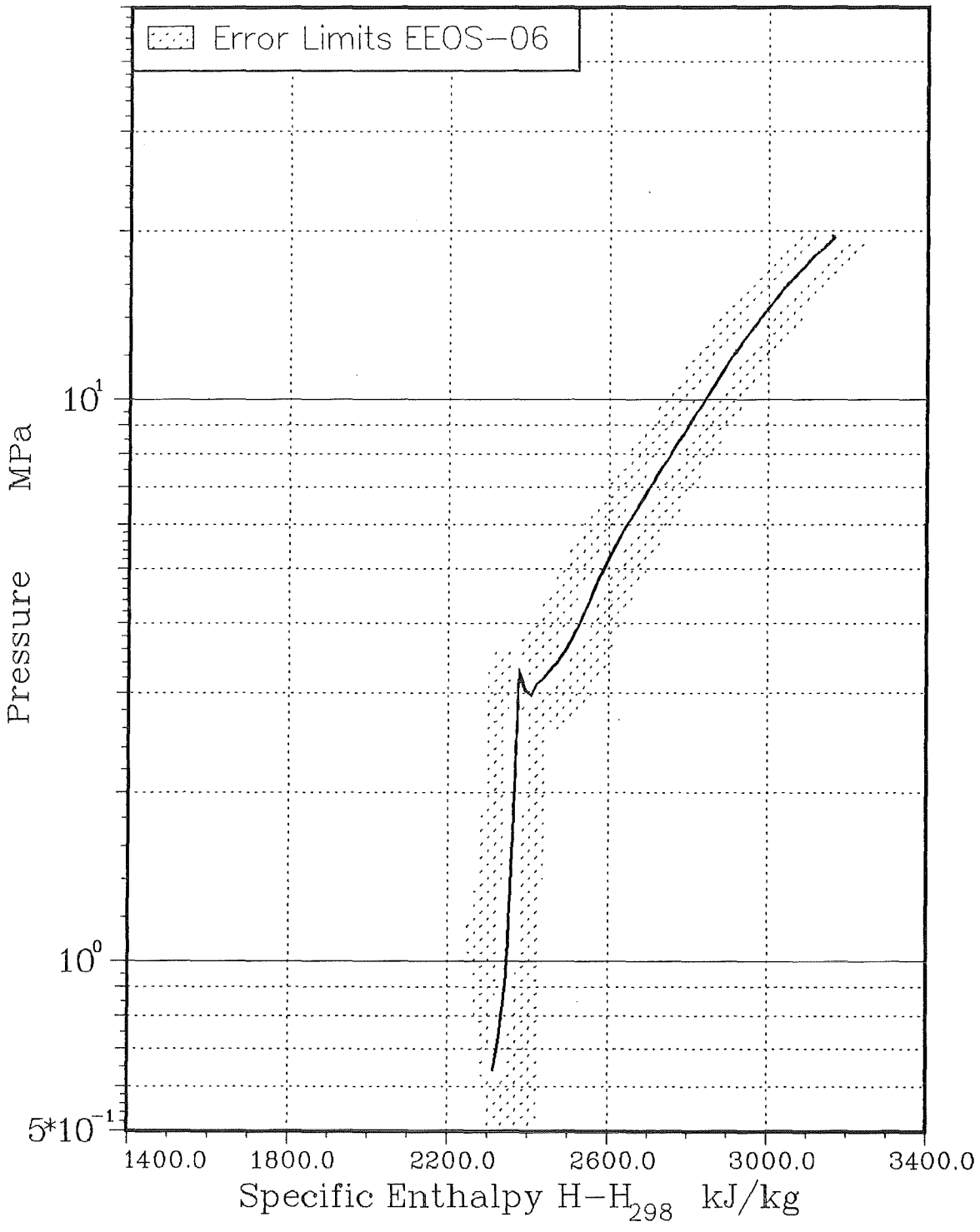

FIGURE VI.21

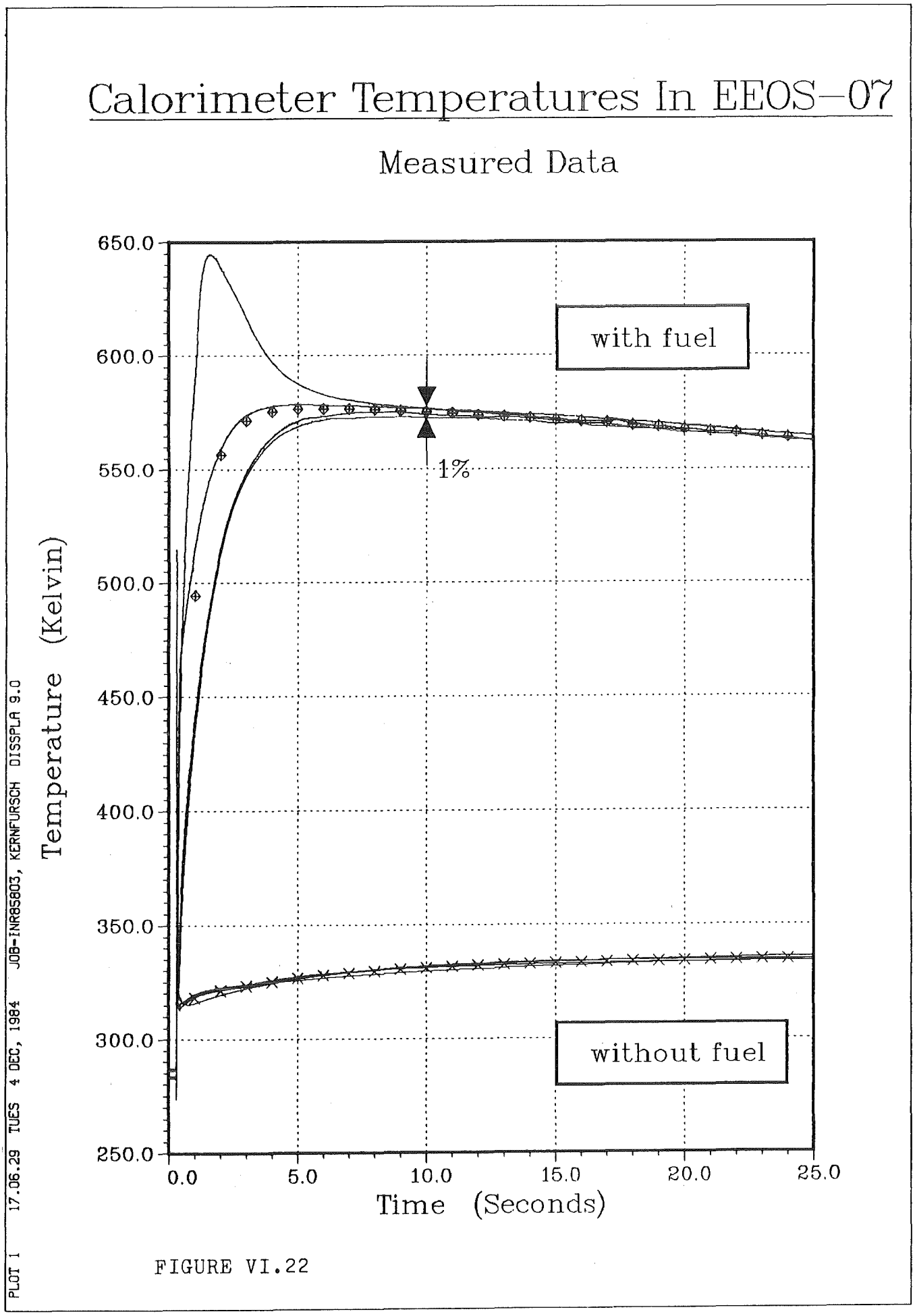
Calorimeter Temperatures In EEOS-07
Measured Data
650.0
600.0
550.0
500.0
450.0
400.0
350.0
300.0
250.0
Temperature (Kelvin)
with fuel
1%
without fuel
0.0
5.0
10.0
15.0
20.0
25.0
Time (Seconds)
PLOT 1 17.06.29 TUES 4 DEC, 1984 JOB-INR85803, KERNFURSCH DISSPLA 9.0

FIGURE VI.22

Calorimeter Temperatures In EEOS-07

Measured Average and Calculated Data

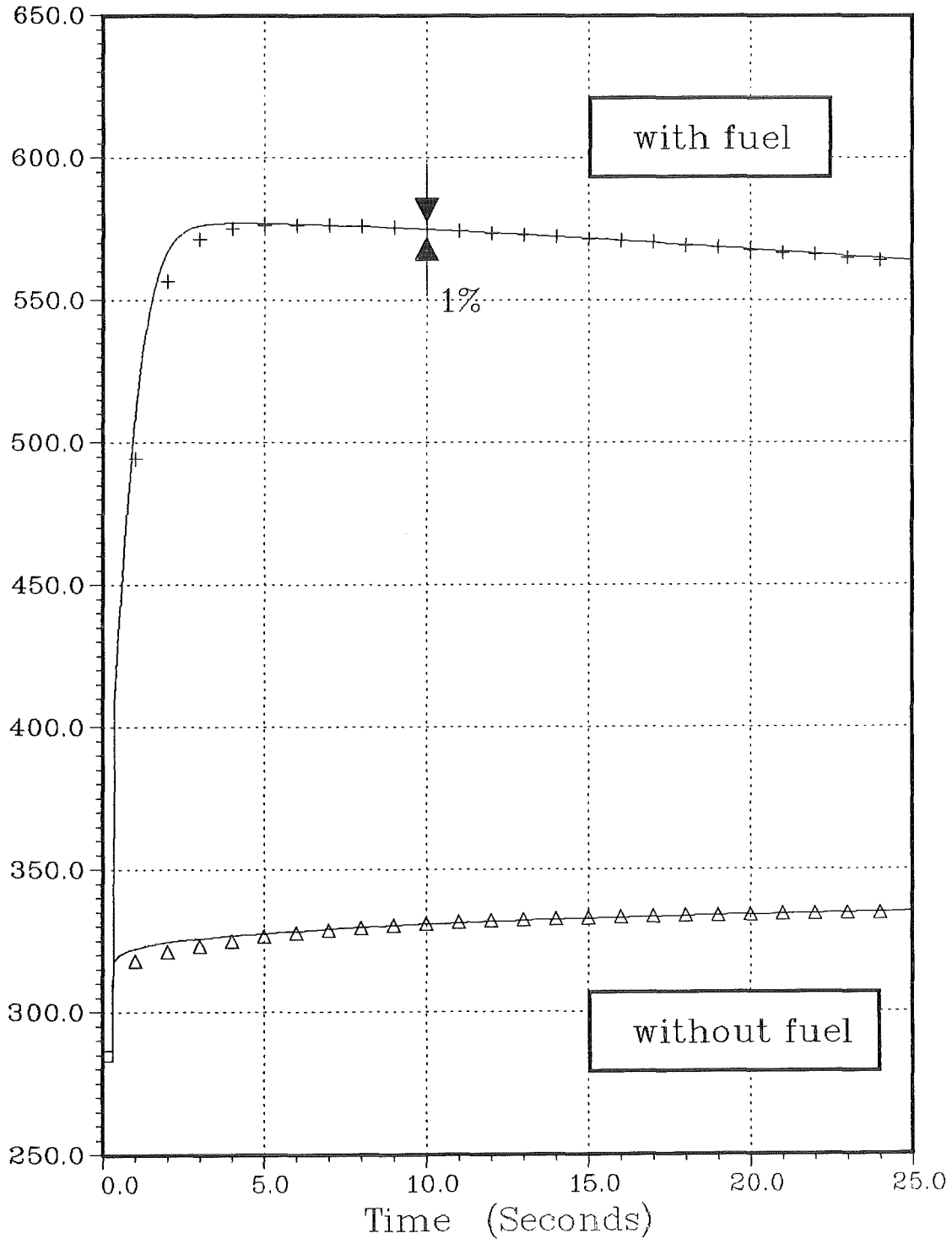

PLOT 1 11.33.37 WED 5 DEC, 1984 JOB-INR85805, KERNFURSCH DISSPLA 9.0

FIGURE VI.23

coupl. factor = $1.359*10^{7}$
cond. factor = 0.100
deviation (K) = 0.56

Fuel Enthalpy in EEOS-07

Data of Heat-up Phase

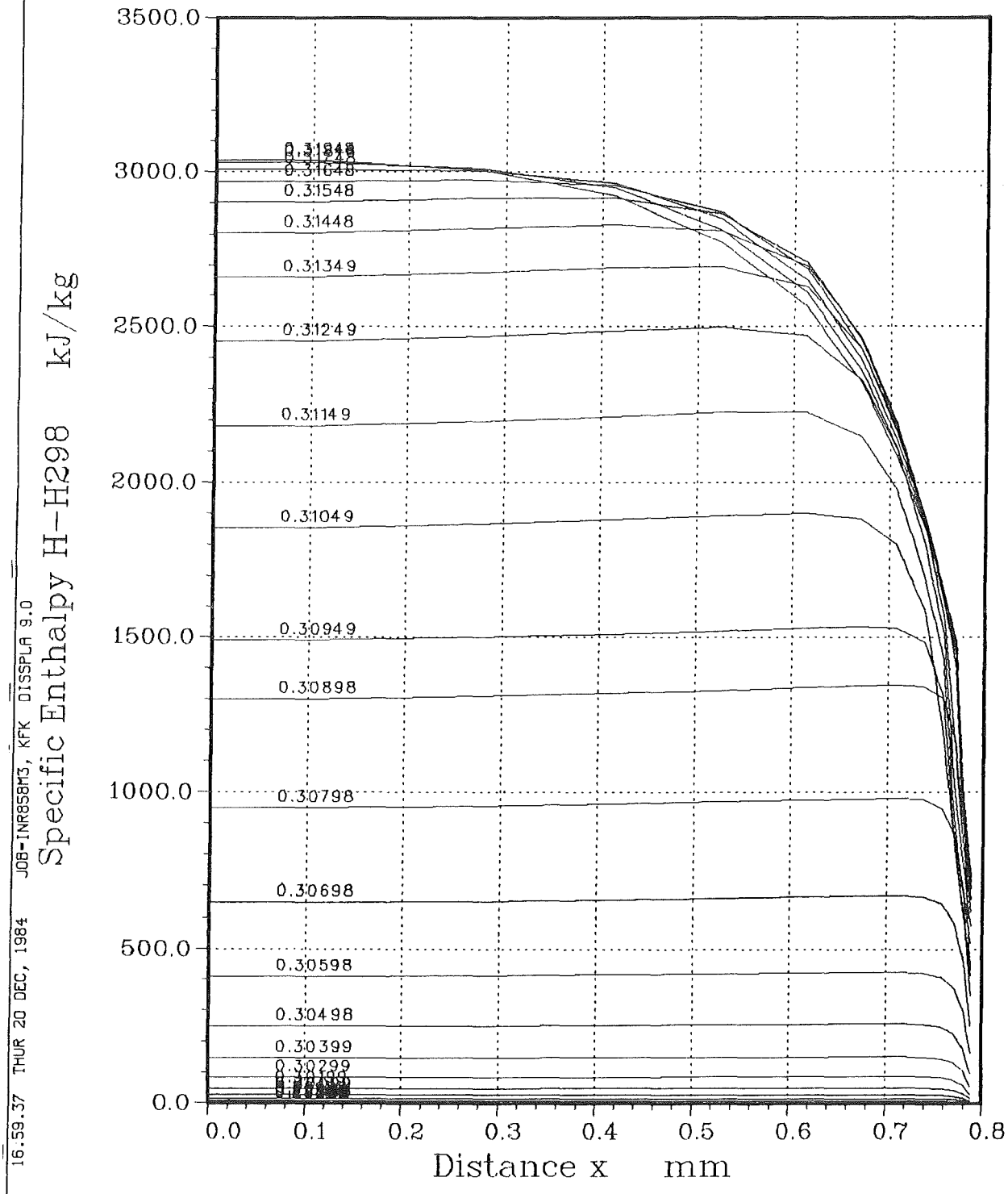

FIGURE VI.24

rpc= 1.4370
enmax=2404.0

Pressure Signals in EEOS-07

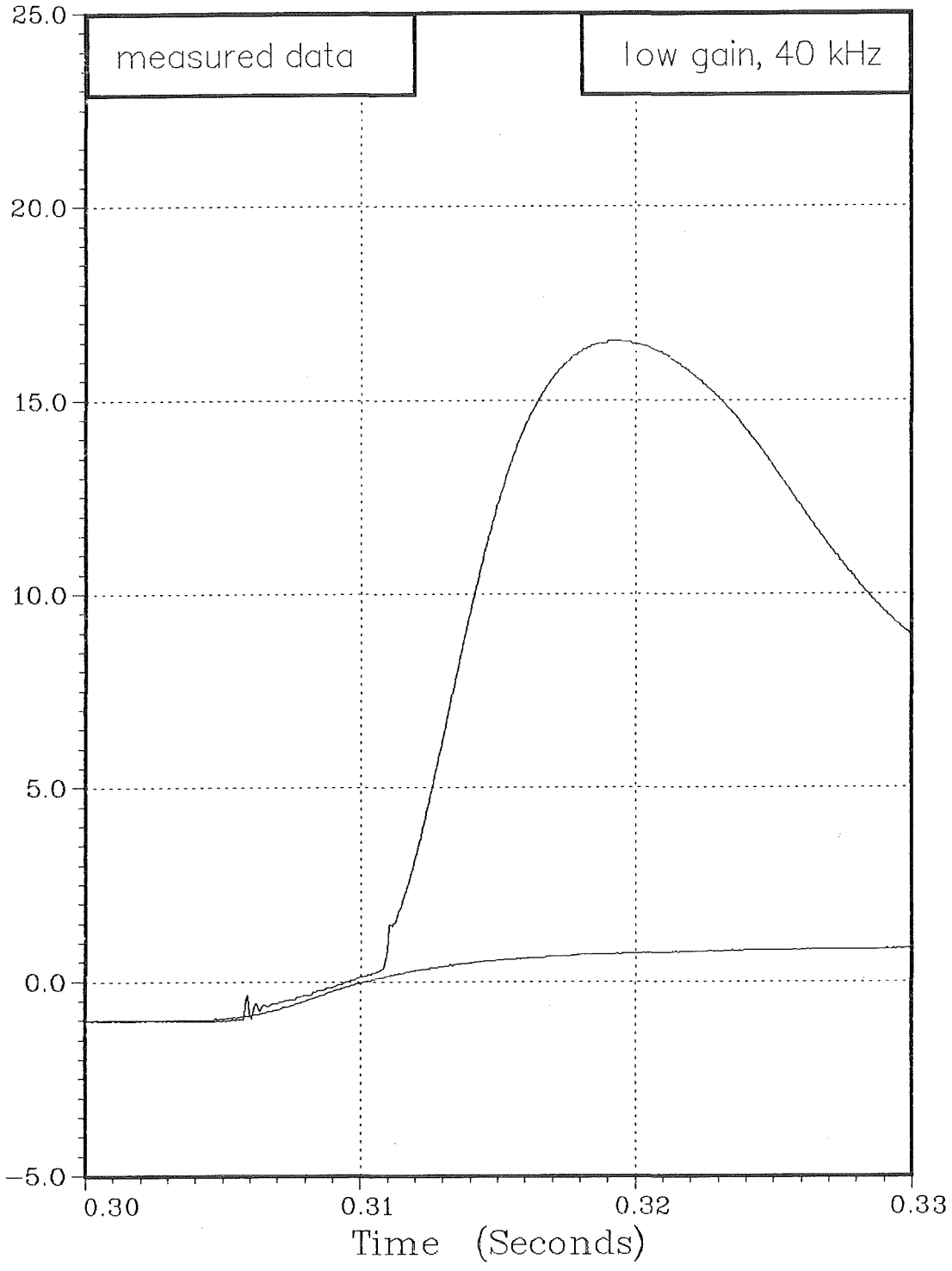

FIGURE VI.25

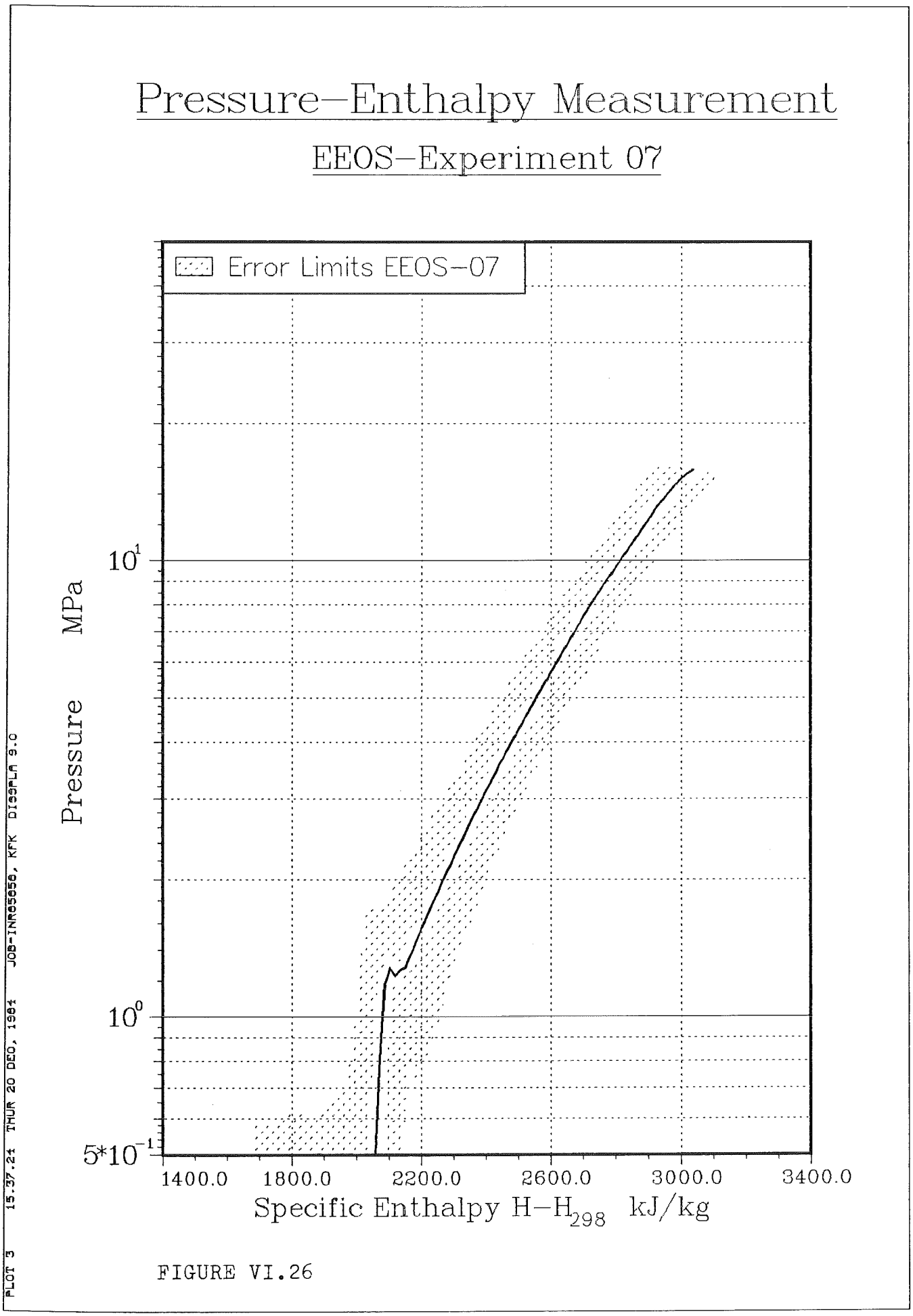
Pressure–Enthalpy Measurement
EEOS–Experiment 07
Error Limits EEOS–07
Pressure MPa
10^1
10^0
$5*10^{-1}$
1400.0
1800.0
2200.0
2600.0
3000.0
3400.0
Specific Enthalpy $H-H_{298}$ kJ/kg
PLOT 3 15.37.24 THUR 20 DEC, 1984 JOB-INR05050, KFK DISSPLA 9.0

FIGURE VI.26

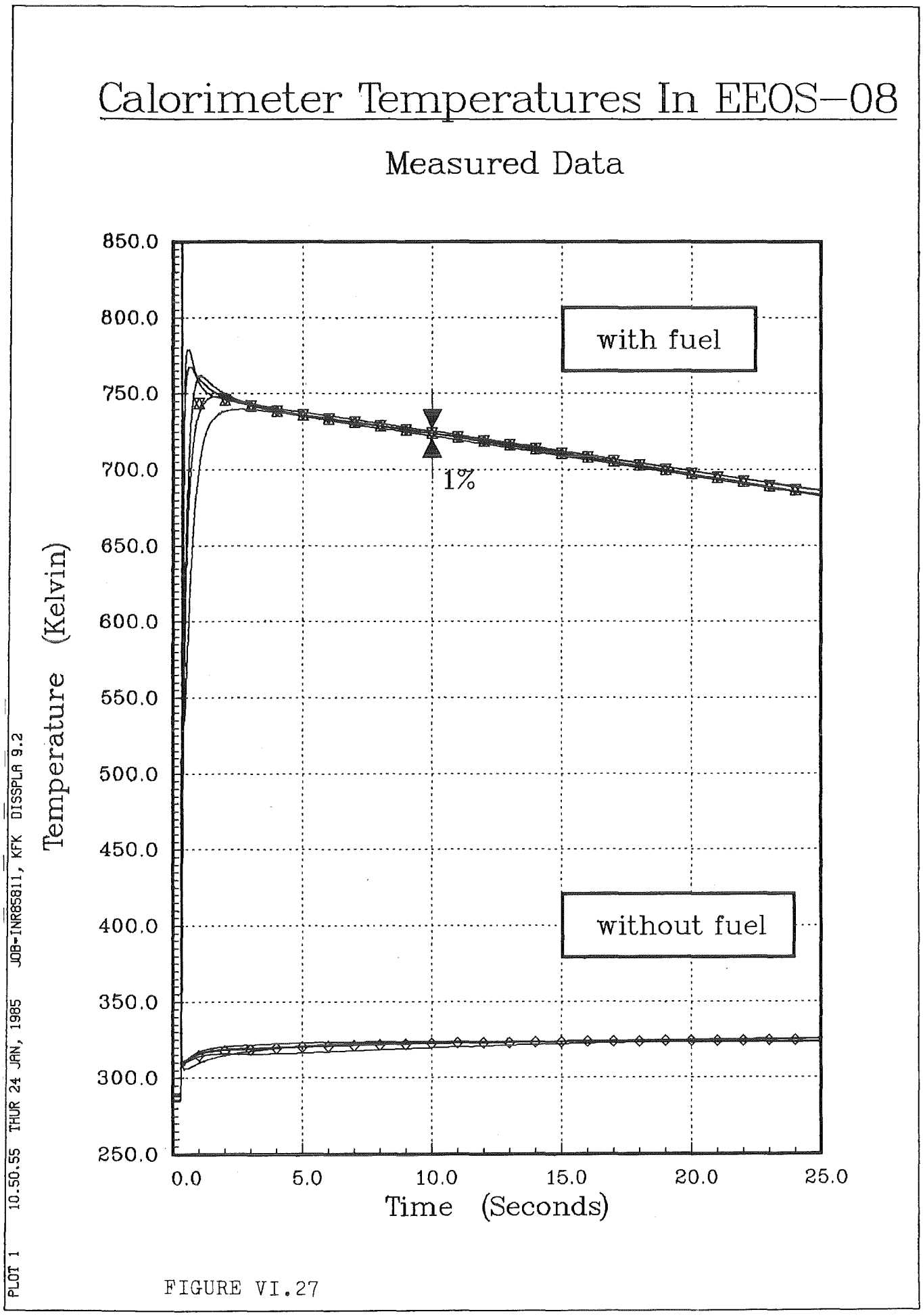
Calorimeter Temperatures In EEOS-08
Measured Data
850.0
800.0
750.0
700.0
650.0
600.0
550.0
500.0
450.0
400.0
350.0
300.0
250.0
Temperature (Kelvin)
with fuel
1%
without fuel
0.0
5.0
10.0
15.0
20.0
25.0
Time (Seconds)
PLOT 1 10.50.55 THUR 24 JAN, 1985 JOB-INR85811, KFK DISSPLA 9.2

FIGURE VI.27

Calorimeter Temperatures In EEOS-08

Measured Average and Calculated Data

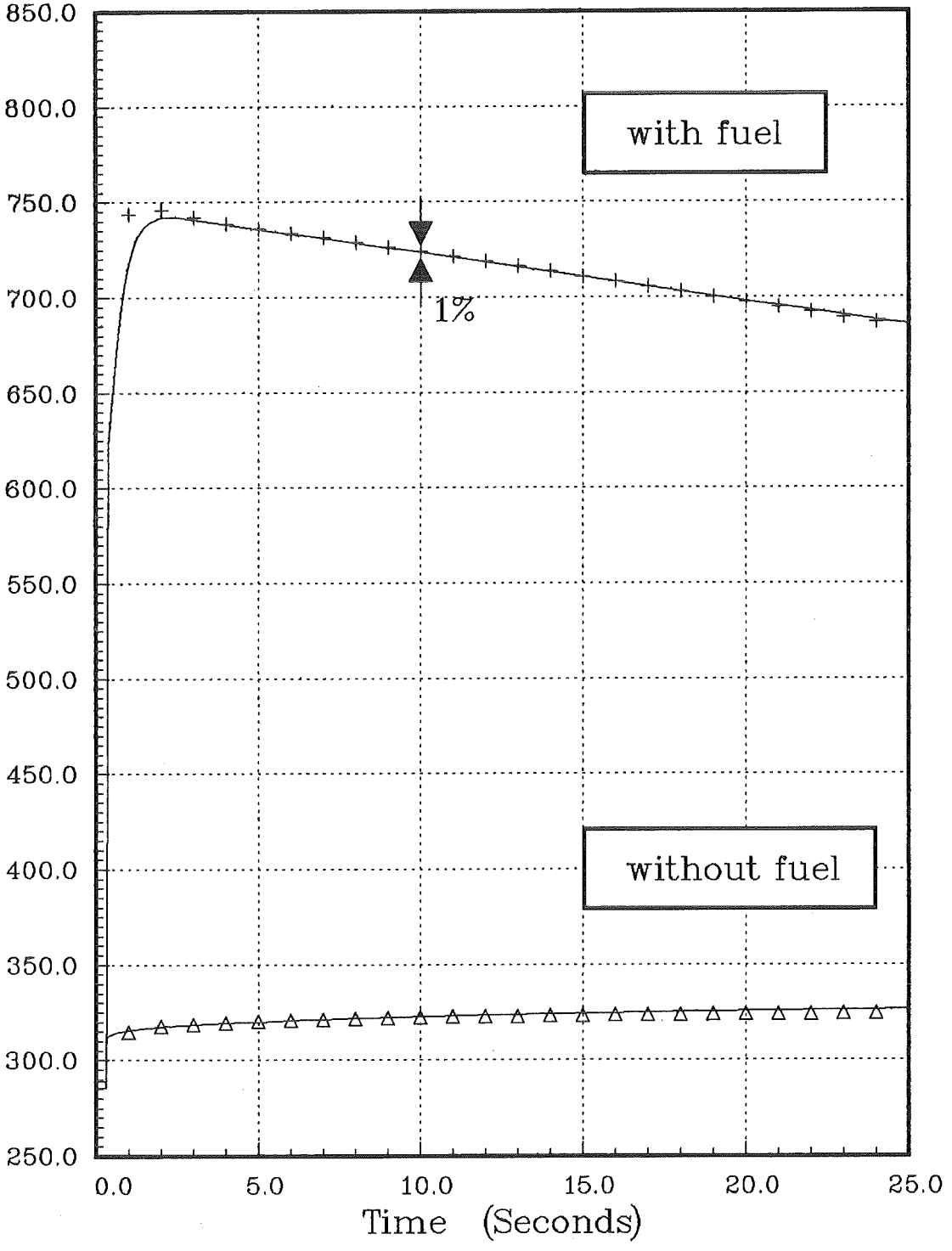

PLOT 1 13.48.26 THUR 24 JAN, 1985 JOB-INR858M2, KFK DISSPLA 9.2

FIGURE VI.28

coupl. factor = $3.160*10^{7}$
cond. factor = 0.180
deviation (K) = 0.65

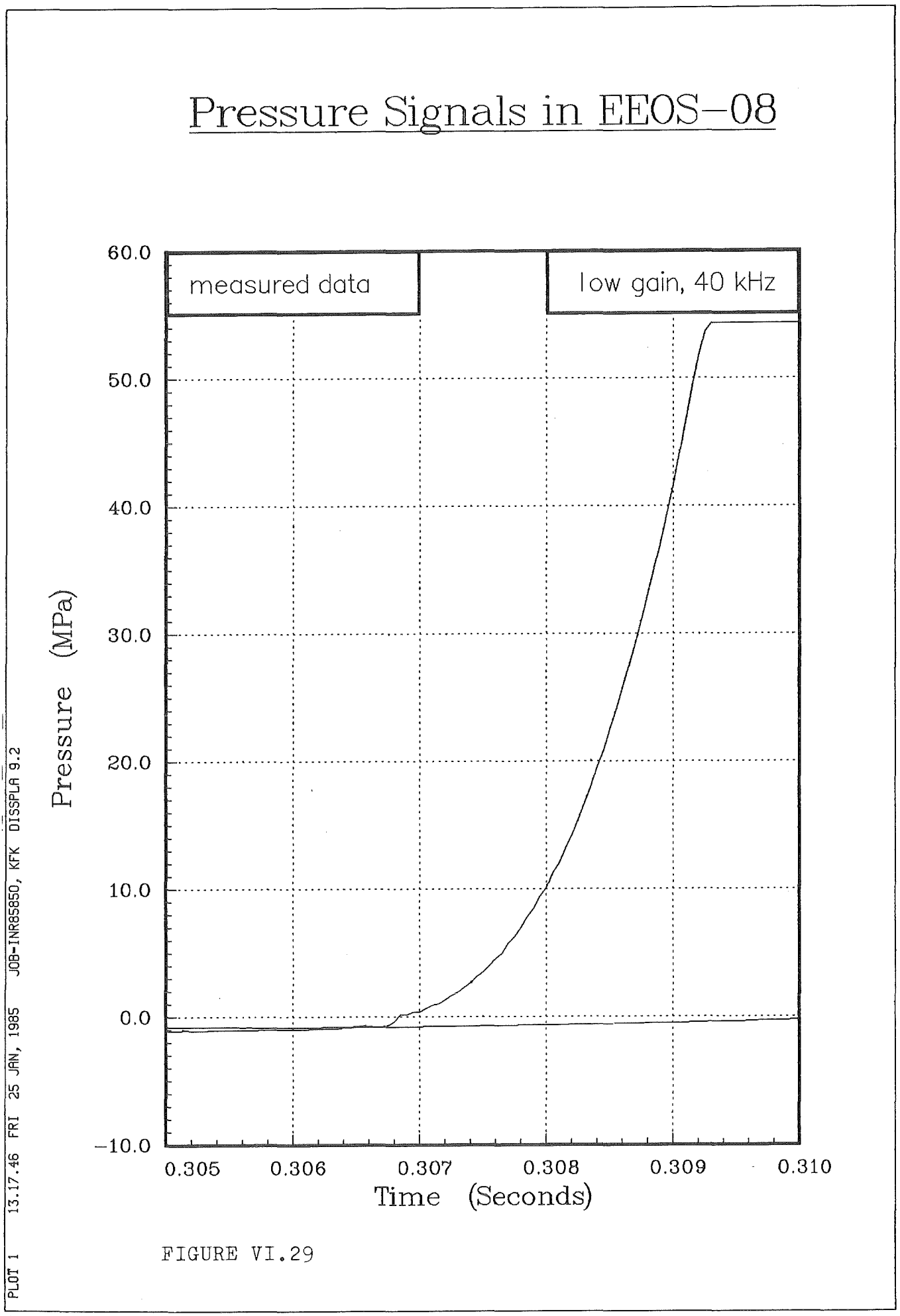
Pressure Signals in EEOS-08
measured data
low gain, 40 kHz
60.0
50.0
40.0
30.0
20.0
10.0
0.0
-10.0
Pressure (MPa)
0.305
0.306
0.307
0.308
0.309
0.310
Time (Seconds)
PLOT 1 13.17.46 FRI 25 JAN, 1985 JOB-INR85850, KFK DISSPLA 9.2

FIGURE VI.29

Pressure–Enthalpy Measurement

EEOS–Experiment 08 , (U,Pu)–Oxide

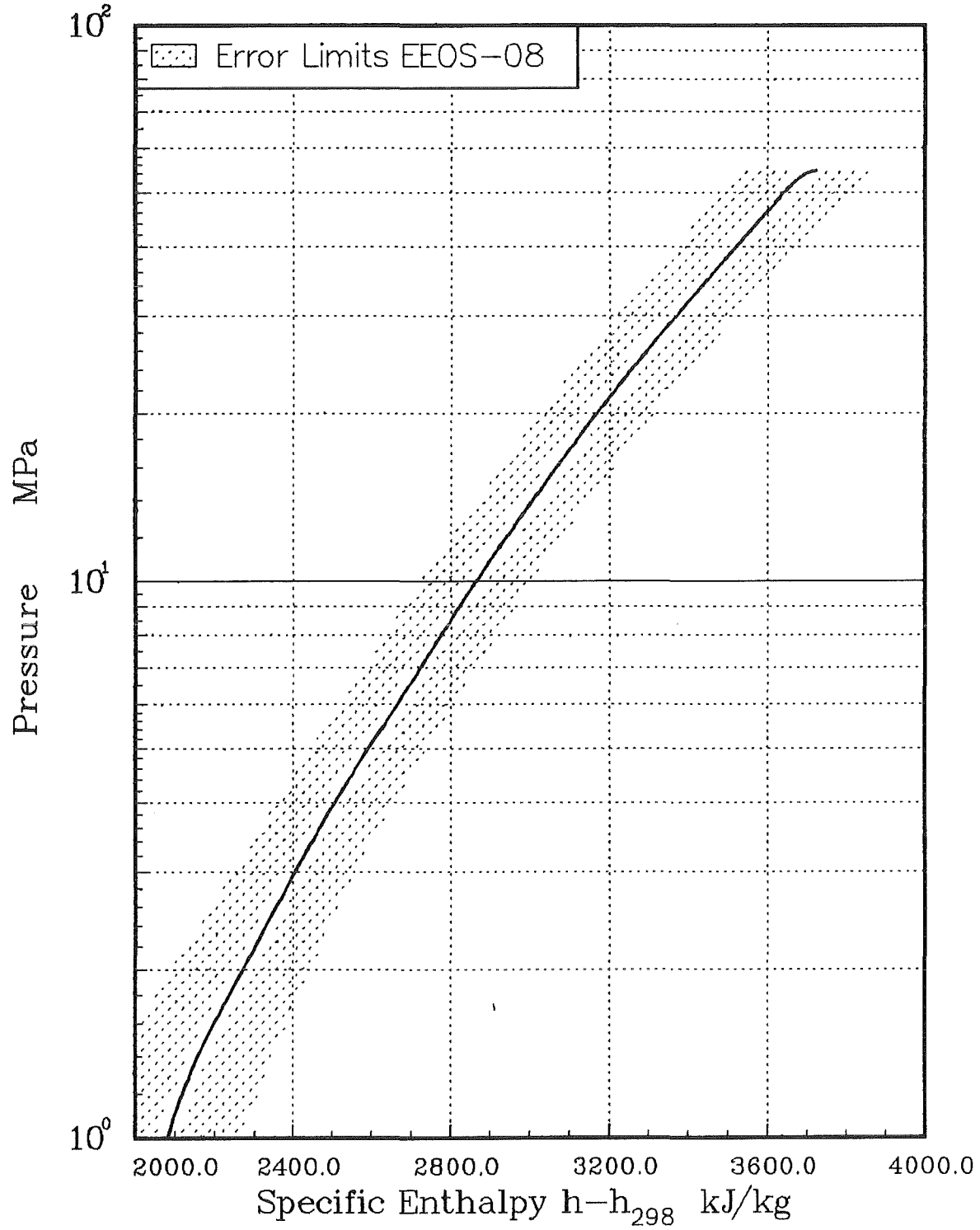

PLOT 3 11.19.09 THUR 31 JAN, 1985 JOB-INR85866, KFK DISSPLA 9.2

FIGURE VI.30

Calorimeter Temperatures In EEOS-09

Measured Data

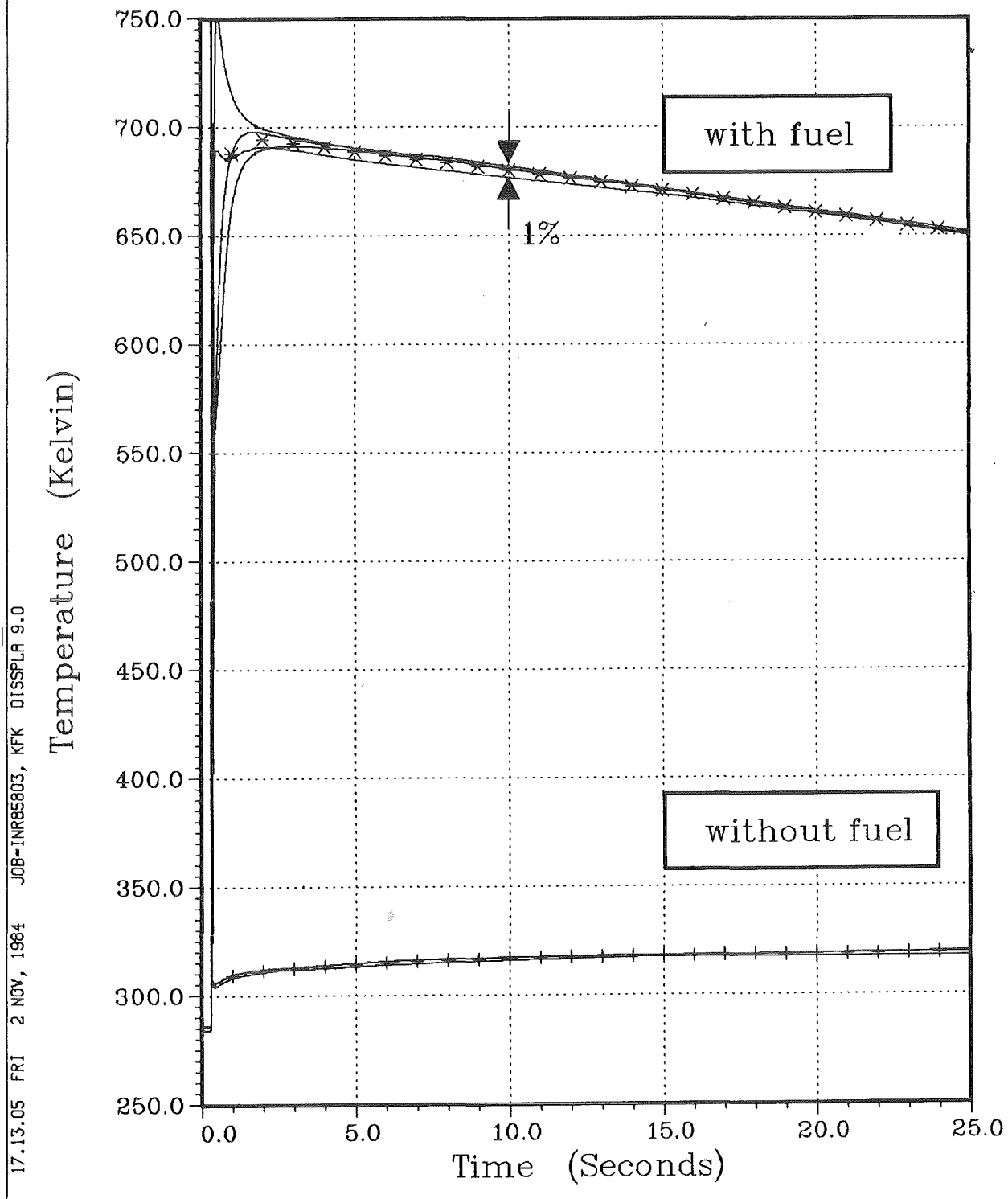

FIGURE VI.31

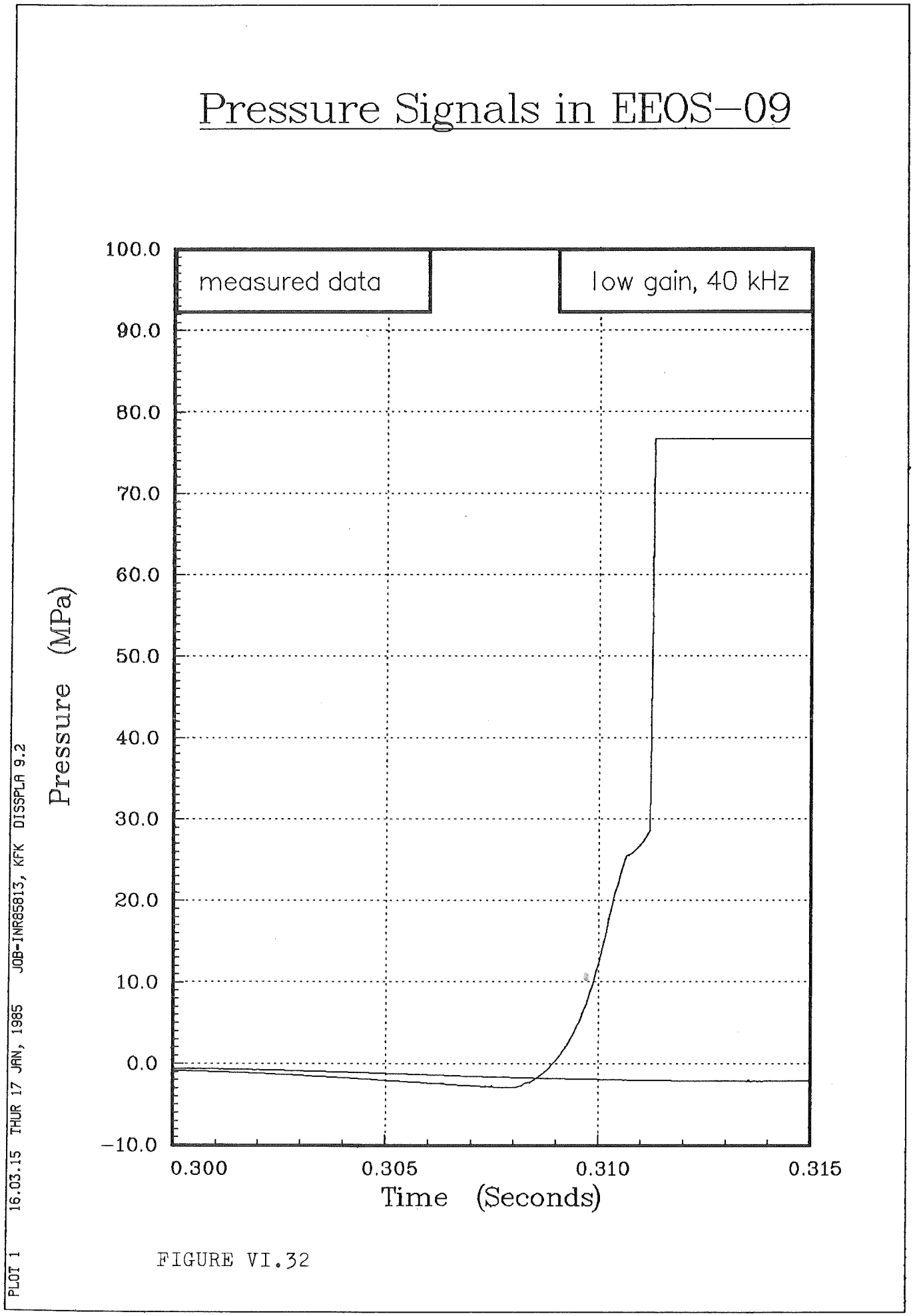
Pressure Signals in EEOS-09
measured data
low gain, 40 kHz
100.0
90.0
80.0
70.0
60.0
50.0
40.0
30.0
20.0
10.0
0.0
-10.0
Pressure (MPa)
0.300
0.305
0.310
0.315
Time (Seconds)
PLOT 1 16.03.15 THUR 17 JAN, 1985 JOB-INR85813, KFK DISSPLA 9.2

FIGURE VI.32

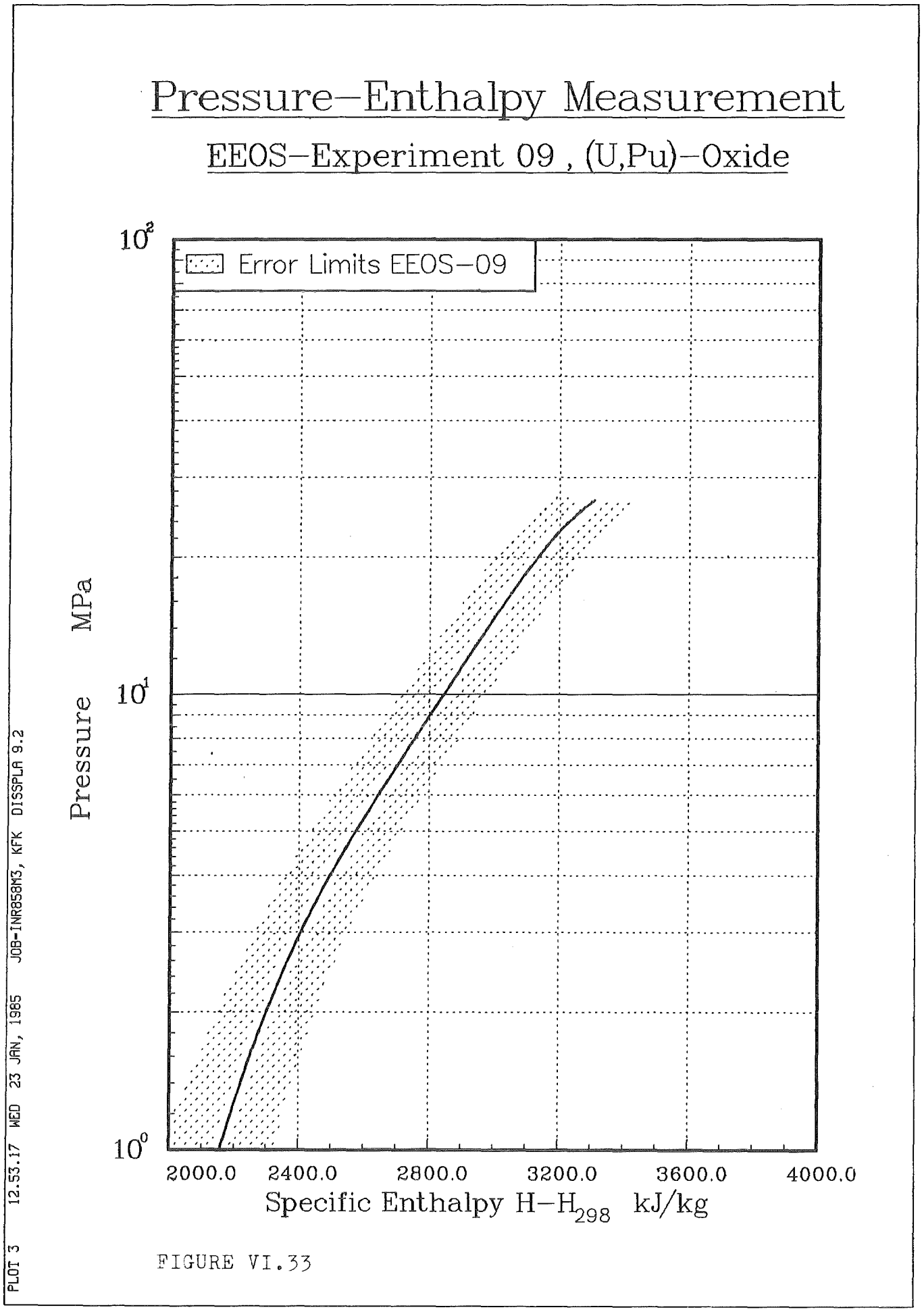
Pressure–Enthalpy Measurement
EEOS–Experiment 09 , (U,Pu)–Oxide
Error Limits EEOS–09
Pressure MPa
10²
10¹
10⁰
2000.0
2400.0
2800.0
3200.0
3600.0
4000.0
Specific Enthalpy H–H298 kJ/kg
PLOT 3 12.53.17 WED 23 JAN, 1985 JOB-INR858M3, KFK DISSPLA 9.2

FIGURE VI.33

VII. COMPARISON OF RESULTS

VII.1 EEOS-Tests

The results for uranium oxides are summarized in Figure VII.1, those for (U,Pu) mixed-oxide in Fig. VII.2, and all six EEOS tests in Fig. VII.3. The measured saturation vapor pressures agree within the experimental uncertainties, leading to the following conclusions:

1. The EEOS technique seems to yield reproducible results because the three experiment pairs 04/05, 06/07 and 08/09 gave practically identical p-h curves.

2. The pressures from pure and reactor grade UO_2 are not noticeably different under the present experiment conditions.

3. The plutonium content around 23% does not change noticeably the measured saturation vapor pressure from that of UO_2.

The first of the above points indicates, that the experimental method and the data evaluation adequately treats the physical phenomena which are important in closed-volume in-pile measurements of the saturation vapor pressure. The important processes are:

- motion of liquid fuel after melting of fuel,
- changes in neutronic energy deposition due to changing fuel distribution, and
- heat transfer to surrounding walls.

In EEOS experiments, motion of fuel was minimized by filling all of the test volume with fuel powder, possible changes in neutronic energy deposition were kept small through the use of cadmium filters (compare Figs. III.6 and III.7), and the heat transfer to the walls was evaluated from the measured pressure decay.

The second points is a not immediatly obvious experimental result since reactor grade UO_2 contains a number of fabrication impurities which should have a significant potential for additional pressures in EEOS experiments. The most prominent candidate is carbon which can be oxidized in liquid fuel to thermally very stable CO:

$$C + \frac{1}{2} O_2 \rightleftharpoons CO \qquad \text{(VII.1)}$$

Law-of-Mass-Action calculations yield for the CO-pressure in a fixed volume which is partly filled with carbon contaminated fuel:

$$p_{CO} = \frac{K \cdot x_c}{1/p_{ref} + K \cdot M_{UO_2} \left(\frac{1}{\rho_s} - \frac{1}{\rho_T}\right)/RT} \qquad \text{(VII.2)}$$

with

$$K = \exp\left[-\frac{\Delta G_f(CO) - \frac{1}{2}\Delta G_{O_2}}{RT}\right] \qquad \text{(VII.3)}$$

where

p_{CO} = equilibrium partial pressure of CO
x_c = initial carbon mol fraction in fuel (before CO formation)
= $6.75 \cdot 10^{-4}$ for 30 wppm C in UO_2
p_{ref} = reference pressure = 1 atm
M_{UO_2} = mole weight of UO_2 = .270 kg/mole
ρ_s = smear density of fuel in test volume = 5300 kg/m^3 in EEOS experiments
ρ_T = fuel density at temperature T
R = gas constant
T = temperature
$\Delta G_f(CO)$ = free enthalpy of formation of CO
ΔGo_2 = oxygen potential of fuel

The second term in the denominator of Eq. VII.2 describes the change of free volume in the fixed test volume due to the thermal expansion of the liquid fuel. Typical pressures calculated for EEOS conditions and a carbon impurity content of 30 wppm in the fuel are given in Table VII.1. The tendency in p_{CO} with increasing temperatures is towards even higher pressures. The addition of several MPa CO pressure to the fuel vapor pressure should have been easily detectable in the experiments, so that two possibilities remain:

a) the equilibrium in CO-formation was not attained because of kinetic restrictions, or
b) equilibrium was obtained but the CO molecules were not released from the liquid fuel to the vapor phase.

Table VII.1 Calculated equilibrium pressures in an EEOS pressure cell from 30 wppm carbon impurity in the test fuel

T(K)	$h-h_{298}$(kJ/kg)	p_{CO}(MPa)
3200	1437	.52
4000	1825	1.10
5000	2310	1.90

The first possibility appears quite unlikely because CO formation in the liquid fuel just requires electron transfer from a U-O bond into a C-O bond. This process is certainly much faster than the transfer of complete UO_x molecules from the liquid into the gas phase, a process which is obviously detected in the EEOS experiments as pressure increase. The formation of isolated CO molecules in the liquid fuel due to electron transfer does not by itself result in an additional pressure (CO is in solution). Only when the CO (or any other gaseous impurity) moves into the gas phase and in this way increases here the particle density above that of fuel vapor, can the transducer membrane sense an increase in the macroscopic pressure. There is information from experiments on fission gas release kinetics from molten fuel (VIPER, SILENE), indicating that this process requires milliseconds, which is of the same order of magnitude as the

time"at molten state" in EEOS experiments. It appears therefore, that in EEOS experiments a significant pressure contribution from impurities is supressed by the limited release kinetics of gases from the liquid fuel, or in other words by the velocity with which gaseous impurities like CO leave the state of solution in liquid fuel.

VII.2 Earlier p-h Measurements

The EEOS results for UO_2 are compared in Fig. VII.4 with three earlier pressure-enthalpy measurements.

1. Reil 1977:

The very first in-pile EEOS measurements on nuclear fuels were published in Ref. II.1. The theoretical analysis determined an upper and a lower bound for the pressure-enthalpy curve. The upper pressure bound was obtained by correlating the volumetric average energy of the fuel sample with the pressure-time signal and the lower pressure bound resulted from the use of the peak energy in the fuel. In the original data evaluation the necessary neutronic energy deposition profile was calculated for the solid disk geometry using a S-4 version of TWOTRAN. These constant energy deposition data of the disk sample were then used for analysis of the whole experiment.

Subsequent modeling efforts using an interactive system of the hydrodynamics code CSQ II and the neutron transport code TWOTRAN (in S-8 version) which allows recalculation of the neutronic energy deposition as the liquid fuel changes its geometry, showed however that the fuel probably attained a more compacted configuration after melting /VII.1/. In this case the peak energies would have been about 20% higher than in the original energy evaluation, shifting the right hand line in Fig. VII.4 to higher enthalpy values. Another insight from the above mentioned CSQ-TWOTRAN calculations was, that the peak energy is governing the vapor pressure in the test volume. Fuel regions with less energy are not boiling, they

exist in a compressed liquid state. In view of these results the band given in Fig. VII.2 is overly conservative. It is sufficient to restrict the energy analysis to evaluation of the peak energy in the fuel (right hand side bound in Fig. VII.4). If a compacted geometry was attained in the liquid state, as indicated by modeling calculations, this peak energy curve would have to be shifted to higher energies.

2. Benson 1977:

Also in 1977, pressures from electron-beam heated fuel samples were published /VII.2/.

Figure VII.5 gives a schematic sketch of the experimental setup. A 25 µm thick layer of $UO_{2.08}$ powder is confined between two moveable graphite pistons. After the sample is heated to a desired internal energy in about 1 µs, the evolving vapor accelerates the pistons in opposite directions. The piston motion is followed for the next 5 to 20 µs by recording the time dependent width of their shadows. A fast infrared pyrometer measures the total temperature rise in a graphite dosimeter plate.

The energy deposition in the liquid oxide sample is evaluated from the measured graphite temperature increase and a theoretical extrapolation to the UO_2 sample location with the help of an electron transport code. The total uncertainty associated with this energy evaluation was estimated to $\pm$ 5%.

For the vapor pressure evaluation, the expansion of the liquid-vapor fuel mixture is treated as isobaric. In an isobaric expansion, the internal pressure acting on the moveable piston can be evaluated from the measured piston location x(t), using the simple equation of motion:

$$p = \frac{m}{A} \ddot{x} \qquad \text{(VII.4)}$$

The acceleration $\ddot{x}$ is found as the slope of the approximately linear $\dot{x}(t)$-plot. The resulting pressure is then correlated to the calculated peak energy deposited in the condensed sample prior to its expansion. The p-U data obtained this way are plotted in Figure VII.4.

With respect to the isobaric pressure evaluation model the following comment is necessary. Volume expansion in the REBA experiments amounted to 25 to 70 times the initial volume V_o, depending on the specific experiment. For such large expansion ratios, noticeable cooling of the liquid phase should occur due to vapor production. This in turn would result in a vapor pressure drop and a non-isobaric expansion of the liquid-vapor mixture. The magnitude of this effect was estimated by calculating the liquid internal energy U_L as a function of the expansion ratio V/V_o. Figure VII.6 shows U_L (V/V_o) for initial internal energies U_o which were deposited in REBA experiments, if a Harwell EOS for UO_2 is used /VII.3/.

Quenching of the liquid phase during expansion becomes increasingly severe with increasing initial energy deposition U_o because the vapor density increases exponentially with liquid internal energy. The circles in Figure VII.6 indicate the V/V_o ratio up to which the expansion was followed in the respective REBA experiment. The pressure ratios of initial to final vapor pressure $p_o/p = p(U_o)/p(U_L)$ are given for these points. The dashed line for U_o=1860 J/g is obtained when the low vapor pressures of the Harwell EOS are replaced by the higher pressures evaluated in the REBA experiments themselves. The two lines for U_o=1860 J/g can be regarded as reasonable upper and lower bound for the true $U_L(V/V_o)$ curve.

Considering the large pressure drop ratios p_o/p, it is difficult to envision that the constant pressures seen in the REBA experiments are due to fuel vapor pressure alone. An additional unknown pressure source, which increased in time, should have balanced the decaying fuel vapor pressure. Therefore the measured pressures should be considered an upper pressure bound for the true saturation vapor pressure of UO_2.

3. Limon et al 1981:

In this in-pile technique, a thin UO_2 disk is fission heated in a tungsten tube containing Ar gas at a given pressure/ VII.4/. The tube contains a pressure transducer and a condenser plate, the temperature of which can be monitored with a fast thermocouple (Fig. VII.7). Typical heating times in the pulsed Silene reactor are 10 ms. For a p(h) measurement, the following data are taken: capsule pressure p(t), relative reactor power P(t), and after irradiation the total number of fissions in the sample. The data evaluation identifies the point in time where a sudden pressure rise indicates fuel boiling; at that time the fuel vapor pressure equals the Argon gas pressure as recorded by the transducer shortly before onset of boiling.

Evaluation of the corresponding fuel average energy follows in principle Eq. V.11. The total energy deposition (described by the first three terms in Eq. V.11) is in the CEA technique obtained by multiplying the measured total number of fissions in the sample with a previously determined value for the energy per fission of 170 MeV/ fission. The fission rate in the fuel is assumed to be proportional to the reactor power, which is equivalent with using a constant coupling factor C and fuel density ρ in Eq. V.11. C and ρ then cancel. The resulting data points are shown in Figure VII.4.

Evaluation of the boiling pressure is very precise since the small changes in the initial fill gas pressure due to gas heating are measured on-line. Evaluation of the corresponding boiling energy depends somewhat on the definition of "boiling-onset". Other uncertainties in the energy evaluation come from two assumptions namely

- equilization of the energy in the boiling fuel zone with the volumetric average energy, and
- use of a constant coupling factor over the whole duration of the experiment, although the sample can expand significantly after onset of fuel boiling, giving rise to increased energy deposition during the rest of the pulse.

It appears that the two assumptions are more appropriate at high than at low energy depositions. In high energy experiments, high temperatures and relatively long heating times cause the hottest fuel node, where boiling begins, to migrate inwards away from the cooled surface. The boiling node energy is then probably not much above the average fuel energy. Also in high energy experiments, boiling begins only late in the prompt pulse, so that most of the prompt energy is deposited in the fuel disk configuration and only the pulse tail in the dispersed fuel geometry.

However in low energy experiments both assumptions can lead to noticable deviations between actual and calculated boiling energy. Since the two assumptions have a canceling tendency, a precise estimate of the net energy deviation would require additional neutronic and heat-transfer calculations. If one decides to apply information from the ACRR experiments to include fuel dispersal and heat losses in the low energy CEA tests, it is found that the actual energy of the boiling zone may have been of the order of 10% higher than in the original energy evaluation (points at .18 and .61 MPa). For the high energy tests the deviations are expected to be significantly smaller because of the above given reasons and because the energy deposition profile was much flatter due to thinner and less enriched fuel samples.

The presented assessment of the existing p-h data shows, that despite the large data scatter in Fig. VII.4, there is quite some evidence that the saturation line of UO_2 is located in the vicinity of the CEA and SNL/KfK results.

VII.3 Earlier p-T Measurements

VII.3.1 Conversion of In-Pile Data

The p-h data measured in EEOS experiments, can be transformed into the p-T format using the relation

$$h_T - h_{298} = \int_{298}^{T} c_p(T)\, dT \qquad \text{(VII.5)}$$

where

h_T = specific enthalpy at temperature T, (kJ/kg)
h_{298} = specific enthalpy at reference temperature 298 K, (kJ/kg)
c_p = specific heat, (kJ/kg K)

Since in EEOS experiments the fuel state changes along the saturation line, Eq. VII.5 should actually contain $(\partial h/\partial T)_{sat}$ instead of $c_p = (\partial h/\partial T)_p$. However it was shown /II.1, VII.5/ that for UO_2 the heat capacity along the saturation line is practically identical with c_p up to temperatures well above 6000 K.

Heat capacity data for liquid UO_2 and gaseous U-O molecules are summarized in Fig. VII.8. The assessment by Fink, Chasanov and Leibowitz/ VII.5/ yielded a constant c_p value and the shaded 1-σ-uncertainty band. The data by Fischer/ VII.6/ result from Significant Liquid Structure modeling of liquid UO_2, and the curve by Hoch/ VII.7/ from a fit of measured liquid UO_2 enthalpies, using a specific heat expression which was able to describe high temperature heat capacity data of many liquid metals and of liquid Al_2O_3. Since one should expect that the heat capacity of liquid UO_2 approaches that of gaseous U-O molecules with increasing temperature, the c_p data of Green/ VII.8/ are also included in Fig. VII.8. The heavy dashed line was choosen as best estimate for the h-T conversion of the EEOS results.

In order to check the influence of the presently existing uncertainties in c_p on the h-T transformation, Eq. VII.5 was evaluated with a constant c_p of .485 kJ/kg K, with the increasing, and with the decreasing $c_p(T)$ function, marked "upper bound" and "lower bound" in Fig. VII.8. The corresponding p_{sat}-T curves from experiments EEOS-04 to -07 are plotted in Fig. VII.9 in the usual p-1/T format. The variation of c_p within the above given limits results very roughly in a shift of $\pm$ .1 units on the 10^4 K/T temperature scale.

For the comparison of the EEOS data with earlier pressure-temperature measurements, the EEOS results were transformed with the best-estimate-c_p shown in Fig. VII.8, which is given by

$$c_p(T) = .5533 - 2.189 \cdot 10^{-5} \cdot T \qquad \text{(VII.6)}$$

Also the CEA in-pile data were converted with this specific heat.

VII.3.2 Comparison of p-T Data

Figure VII.10 compares the converted in-pile results with previous $p_{sat}(T)$ measurements. The data can be divided into three subgroups:

1. Stationary measurements from the UO_2 melting temperature up to about 3500 K.
2. Transient laser heating experiments from about 3500 to 5000 K.
3. Transient in-pile tests above 5000 K.

In order to see if a consistent picture can be derived from the different experimental data, an assessment of the employed methods was attempted.

1. Stationary measurements (ANL 1972)

In the ANL transpiration technique/ VII.9/ a weighted amount of UO_2 is heated to the test temperature and an inert gas is passed over the sample (Fig. VII.11). This gas carries the vapor species into a cold tube were the uranium bearing molecules condense. After the experiment the total amount of uranium oxide collected in the tube is determined by wet chemistry. The total pressure of uranium bearing species in the carrier gas can then be calculated from the total UO_2 amount condensed and the number of moles of carrier gas passed through the system. Carrier gas saturation - which is the basic requirement in this technique - seems to be given in the ANL tests, because the results obtained for solid UO_2 agree with those of other techniques within the experimental uncertainties. The measurements cover temperatures from 2630 to 3450 K.

Although the transpiration data extend only a few hundred degrees into the liquid range, these results are considered very valuable for the following reasons:

- The transpiration method is the only technique which was used on solid and liquid UO_2, it is benchmarked against the extensive data base existing for solid UO_2 vapor pressures.
- The stationary evaporation conditions yield true equilibrium data which are needed for CDA calculations, that is the vaporization process is driven by energy transfer from phonons and electrons to surface atoms.
- The experimental uncertainties are very small, about $\pm$ 10% in p, $\pm$ 1% in T.

Since the transpiration method is not of transient nature, material problems limited the measurements to temperatures below about 3500 K.

Figure VII.10 shows that the linear extension of the transpiration data coincides quite nicely with the in-pile work above 5000 K. Since all three measurement methods (CEA in-pile, SNL-KfK in-pile and ANL transpiration) provided almost certainly conditions for pure equili-

brium evaporation, the slope of the line connecting transpiration data and in-pile results, should represent the true heat of vaporization of UO_2. It is obvious that all laser results (exept the LBL work) have significantly higher slopes.

2. Laser experiments, 1974-1985

Six different laser heating techniques were developed with the aim to measure the vapor pressure over liquid fuel samples. The data were published in References VII.10, VII.11, (KfK-INR 1974/76), VII.12, VII.13 (ITU 1974/77), VII.14 (LBL), VII.15 (KfK-INR 1978), VII.16 (ITU 1980), VII.17 (KfK-INR 1984) and VII.18 (ITU neutrals 1985). The different methods developed up to 1981 were discussed extensively in /I.3/, a brief review can be found in /VII.19/.

For the discussion of the overall situation the laser techniques should be divided into two classes:

1. methods in which the laser generated vapor expands into a low pressure environment (vacuum or kPa range), and
2. the boiling point technique (KfK-INR 1984 , Ref. VII.17) where vaporization proceeds against a high fill gas pressure in the test chamber.

In experiments of the first class (References VII.10 to 16 and 18) the pressure evaluation models have to describe complex gas dynamic expansion phenomena of vapor into a vacuum environment. The necessary theoretical basis is often only secured for simple atoms and important characteristics of UO_2 vapor have to be omitted, e.g. that UO_2 vapor is a multicomponent mixture of U, UO, UO_2, UO_3 and that the vapor molecules possess internal degrees of freedom in addition to the translational ones. The wide scatter among the various measurements demonstrates the difficulty of obtaining reliable pressure data.

All laser techniques use fast pyrometry for temperature measurement and in principle little uncertainty results from this, provided correct emissivities are used and optical absorption of the light emanating from the laser crater is indeed negligible as has been assumed in all pyrometer temperature measurements. Since this question was never addressed experimentally, e.g. by a transmission experiment on laser generated UO_2 vapor clouds, uncertainties also enter from this side. An absorption of e.g. 30% would result in an apparent temperature which is 10% too low.

Aside from experimental uncertainties, the more fundamental question arises if in a non-equilibrium experiment involving the rapid expansion of a laser generated vapor jet a true saturation vapor pressure can be determined at all. The saturation pressure is a thermodynamic equilibrium quantity which is defined in any given vapor-liquid system only for the conditions of absent macroscopic energy, momentum, mass or charge flow. However, a laser heating experiment involving the rapid expansion of a vapor jet is characterized by an intense flow in each of these quantities. There is always some kind of theoretical model required to convert the experimental non-equilibrium information into a saturation vapor pressure.

This problem appears less urgent in case of the boiling point technique (KfK-INR 1984). Here the temperature is determined at which a UO_2 vapor jet begins to develop against a preselected inert fill gas pressure /VII.17/. At this boiling temperature the UO_2 vapor pressure is taken to be the fill gas pressure. Since the onset of vaporization is probed rather than properties of the expanding vapor jet, the pressure evaluation does not require the modeling of non-equilibrium expansion processes.

The boiling point technique has also been successfully used to extend the existing vapor pressure data of a number of metals far into the liquid range /VII.20/. It is thus the only laser technique

which was benchmarked on other materials than UO_2. The above mentioned problems of the pyrometric temperature measurement were appearantly overcome in the metal vapor pressure measurements. All these facts lead to the conclusion that of all laser techniques the boiling point method provided the vapor pressure data which are most closely related to true saturation vapor pressures.

Another approach that can be taken in the assessment of laser work - instead of investigating details of the various laser techniques - is to look for systematic differences between the laser data and those from the equilibrium methods (ANL transpiration, CEA and EEOS in-pile techniques). The most obvious observation from Fig. VII.10 is the already mentioned difference in slope. The Clausius-Clapeyron Equation, which reads in the simple case of a one-component liquid/vapor equilibrium in the ideal gas approximation:

$$\frac{d(\ln p)}{d(1/T)} = - \frac{h_v - h_\ell}{R} \qquad \text{(VII.7)}$$

shows that the log p - 1/T - slope is proportional to the heat of vaporization $(h_v - h_\ell)$. R is the gas constant.
There is no obvious reason why the thermodynamic property h of liquid or gaseous UO_x molecules should undergo sudden changes, such that different slope factors result exactly in the temperatures region of the laser measurements. It appears more likely that the steep slope seen in all (except one) laser experiments results from either the optical absorption of thermal surface radiation in the vapor cloud or from the specific laser/liquid interaction. Laser evaporation appears to require more energy than equilibrium evaporation of UO_2. Olstad and Olander /VII.21/ who investigated the laser evaporation of iron - a substance of known vapor pressure- mention already in 1975 the emission of thermionic electrons and thermal ions. Once the electron and ion cloud in front of the surface becomes so dense that it absorbes incoming laser light, a plasma layer forms, giving rise to the emission of energetic, multiply charged particles from the laser crater.

Recently the ITU group presented similar results for the vaporization process in their vacuum evaporation technique /VII.18/. The vapor jet contained more ions than neutral particles, even UO_2^{2+} was observed, the ion velocities exceeded the molecular flow velocities by a factor of 2.5, and electron temperatures at least an order of magnitude higher than the substrate temperature were measured. When the total particle flux (ions plus neutral particles) was used in the original rate of evaporation pressure evaluation /VII.13/ very high apparent pressures were deduced (Fig. VII.10, ITU 1974/77). When only the neutral particles in the vapor jet were considered in the pressure evaluation the curve termed "ITU neutrals 1985" in Fig. VII.10 was obtained /VII.18/. Although this curve is of all laser results closest to the line connecting the equilibrium techniques (ANL, CEA, EEOS), the measured properties of the vapor jet show that the evaporation process is strongly influenced by plasma processes and far away from an equilibrium evaporation. It is difficult to see why the fraction of neutral particles in a laser generated plasma jet should correspond to the equilibrium saturation vapor pressure of the substrate.

The conclusion drawn from these considerations is that the boiling point data /VII.17/ represent the laser results which are most closely related to saturation vapor pressures.

3. In-pile experiments (1981, 1985)

Above 5000 K the two sets of measurements agree quite well, both in absolute magnitude and slope of the vapor pressure curve. As described above, there is reason to believe that the two CEA data points below 5000 K are too low in temperature.

For both sets of measurement the conversion from enthalpy to temperature introduces uncertainties into the data presentation of Fig. VII.10. The c_p influence can be estimated with the help of Fig.VII.9. Note that the 20 MPa pressure line intersects the EEOS-05 curve converted with the "lower bound for c_p" and with "c_p=.485 kJ/kg" at a reciprocal temperature value of 1.35 and 1.50, respectively. Since the c_p used for h-T conversion is reasonably bounded by these two c_p models (Fig. VII.8), c_p uncertainties should be restricted in Fig. VII.10 by the intervall $10^4/T$=1.35 to 1.50 at the 20 MPa pressure line.

VII.4 Conclusions

The above given discussion leads to the following best estimate for the p_{sat}-T saturation vapor pressure curve (T=3120-8500 K):

$$\log p_{sat} = 23.7989(\pm.1505) - 29605.5/T - 4.75783 \cdot \log T \qquad \text{(VII.8)}$$

This curve is shown in Fig. VII.12 together with an estimated uncertainty band of a factor of two. The curve unites the following experimental information:

- Its slope and magnitude is within the experimental uncertainties of the ANL transpiration data.
- The laser results most closely related to the saturation pressure of UO_2 (KfK-INR boiling point technique) are completely represented when the measuring uncertainties are included.
- The in-pile work above 5000 K is also well represented, especially the statistically well secured EEOS data between 3 and 20 MPa.
- Presently existing c_p uncertainties in the h-T transformation of the EEOS results do not cause shifts outside of the factor-of-2 band.

The corresponding p_{sat}-h saturation vapor pressure curve is obtained from Eq. VII.8 together with the following enthalpy-temperature equation:

$$h_T - h_{298} = -221.15 + .5533 \cdot T - 1.0945 \cdot 10^{-5} \cdot T^2 \qquad \text{(VII. 9)}$$

This relation follows from Eqs. VII.5 and VII.6, using the ANL value for the liquidus enthalpy of UO_2 /VII.5/:

$$h_{3120} - h_{298} = 1398.6 \text{ kJ/kg}$$

The p-h fit function including the factor-of-2 band is compared in Fig. VII.13 with the pressure-enthalpy measurements discussed before. The bulk of the EEOS results is represented quite well by the fit function. The factor-of-2 band appears to slightly over-

estimate the experimental EEOS uncertainties at high enthalpy values (compare e.g. to Fig. VI.12) but on the other hand it gains additional weight by inclusion of the high enthalpy CEA data points. At low enthalpy values the experimental errors are larger than the factor of two, but the validity of the proposed band appears defendable in light of the p-T measurements at low temperatures.

The recommended equations VII.8 and VII.9 give a consistent description of the most recent p_{sat}-h and p_{sat}-T measurements on liquid UO_2. The remaining uncertainty of about a factor of two in pressure can be considered sufficient for the purpose of CDA analysis (Chapter I).

Since no measurable vapor pressure differences could be detected between UO_2 and $(U_{.77}Pu_{.23})O_2$ in the EEOS tests, the same saturation vapor pressure curves are recommended for typical LMFBR mixed oxide fuels.

Equation VII.8 yields 3817 K for the normal boiling point T_{bp}, 415.4 kJ/mol for the corresponding heat of vaporization ΔH_{bp}, and 1.90 MPa for the vapor pressure at 5000 K. Trouton's Rule states that the normal entropy of vaporization $\Delta S_{bp}=\Delta H_{bp}/T_{bp}$ ranges between about 70 and 110 J/K mol for all liquids exept He and H_2. The above UO_2 values yield ΔS_{bp}=108.8 J/K mol, a rather high value. Two conclusions may be drawn from this:

1. Liquid UO_2 appears to have a relatively high degree of structure (clusters), comparable to that found in hydrogen-bonded liquids like water or methanol.
2. A steeper vapor pressure curve, as indicated by some of the laser data, would result in an even higher ΔS_{bp} (ΔH_{bp} increases, T_{bp} decreases). This would not be compatible with Trouton's Rule, i.e. the usually observed bonding in liquids. Therefore vapor pressure curves above the shaded band in Fig. VII.12 appear not likely.

Considering the experimental information which has become available since 1978, the IWGFR recommendation for the p_{sat}-T curve /VII.22/ appears somewhat high (about 6.4 MPa at 5000 K).

Pressure–Enthalpy Measurements

EEOS Experiments on Uranium Oxides

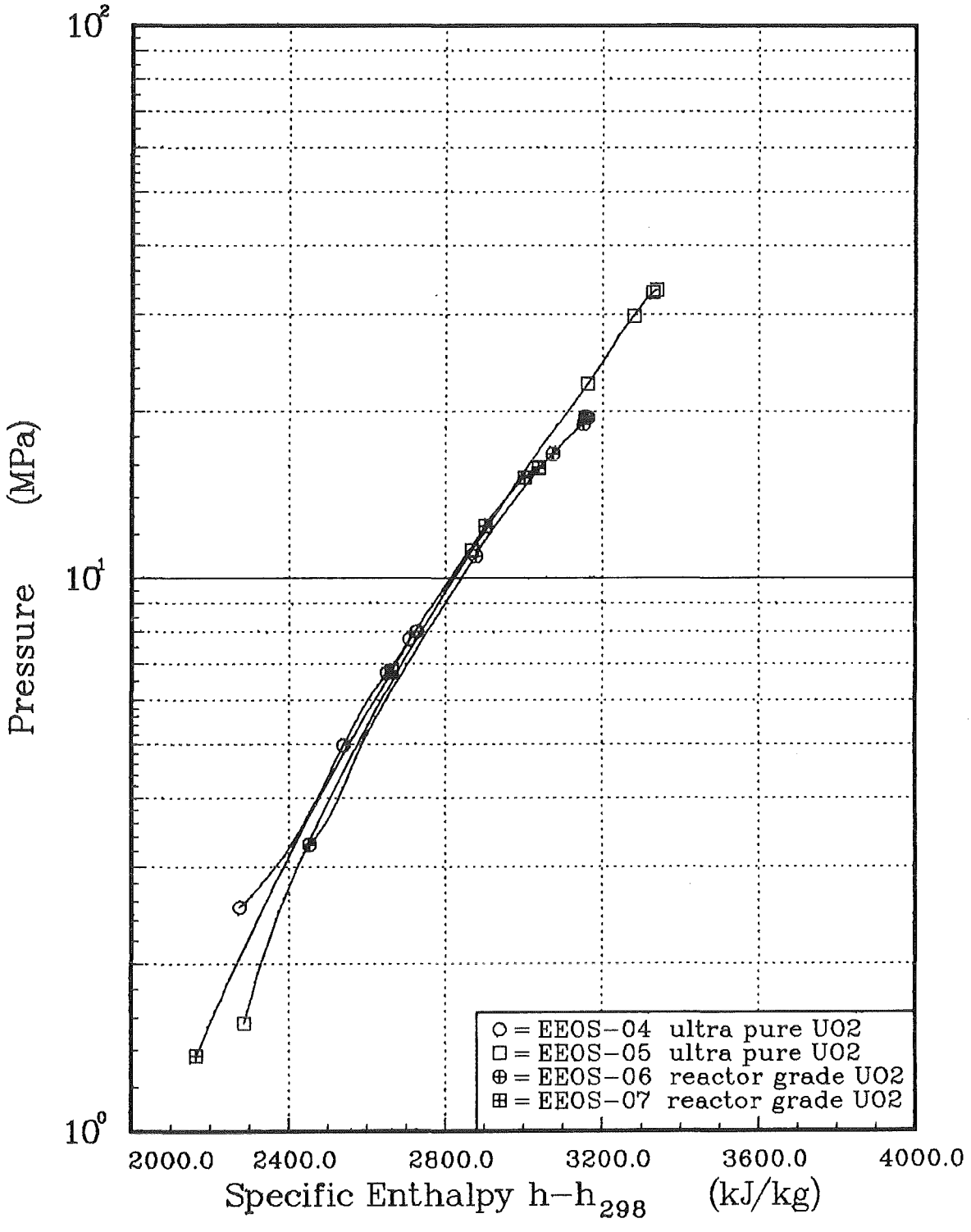

FIGURE VII.1

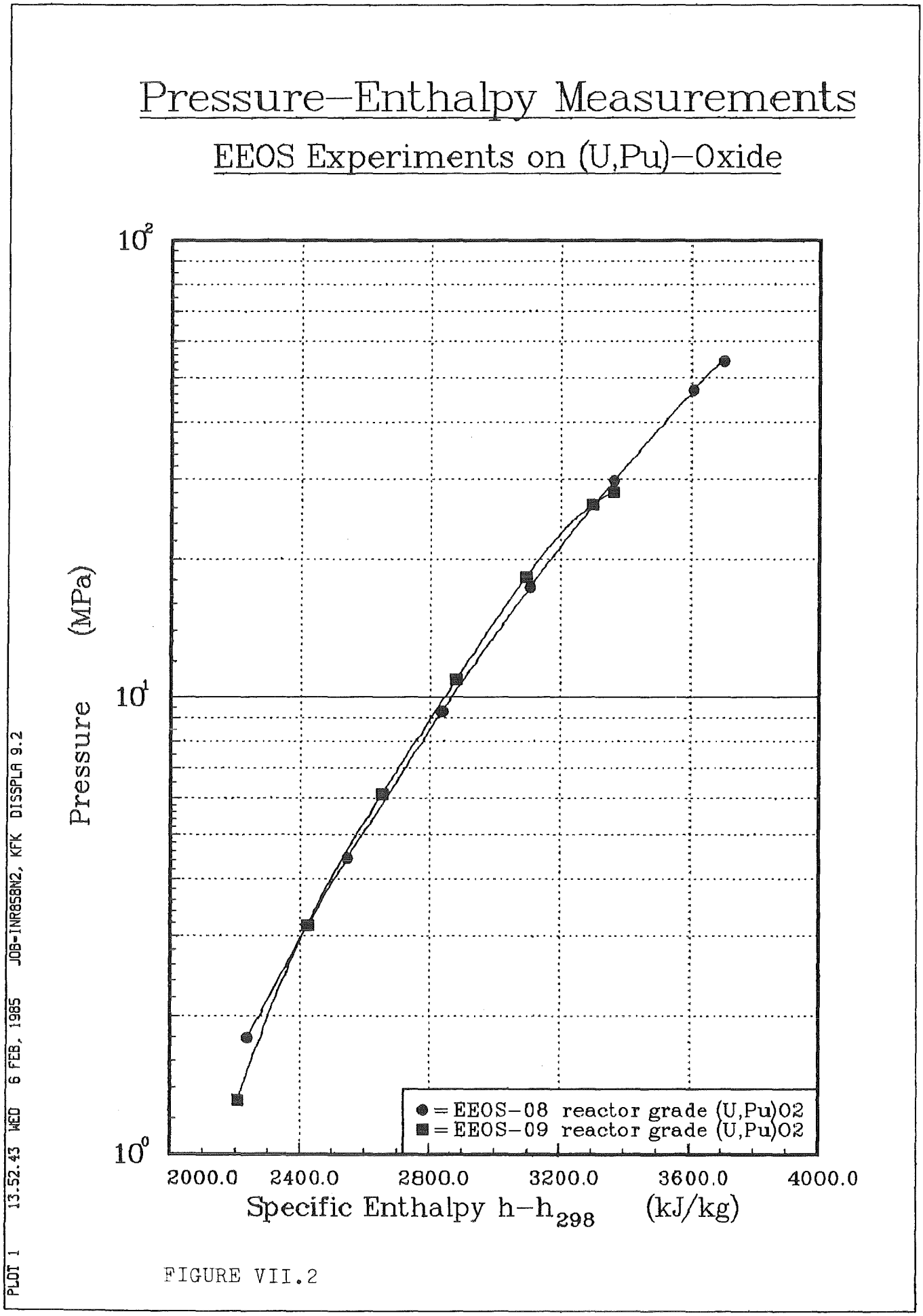
Pressure–Enthalpy Measurements
EEOS Experiments on (U,Pu)–Oxide
Pressure (MPa)
10²
10¹
10⁰
2000.0
2400.0
2800.0
3200.0
3600.0
4000.0
Specific Enthalpy h–h298 (kJ/kg)
● = EEOS–08 reactor grade (U,Pu)O2
■ = EEOS–09 reactor grade (U,Pu)O2
PLOT 1 13.52.43 WED 6 FEB, 1985 JOB=INR85N2, KFK DISSPLA 9.2

FIGURE VII.2

Pressure–Enthalpy Measurements

Experiments EEOS–04 to –09

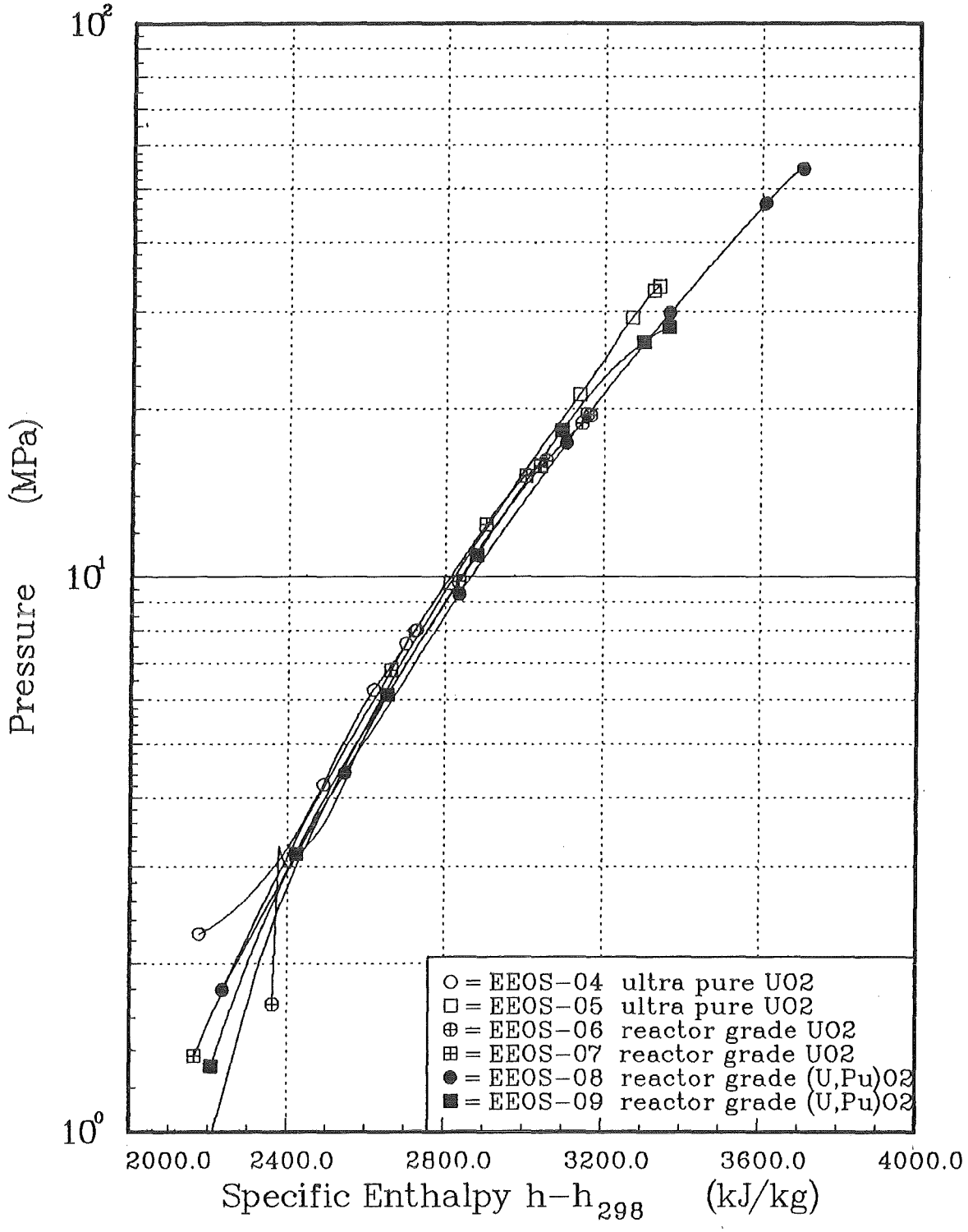

PLOT 1 11.59.27 MON 4 FEB, 1985 JOB-INR858N9, KFK DISSPLA 9.2

FIGURE VII.3

Pressure–Enthalpy Measurements

Liquid Uranium Oxides

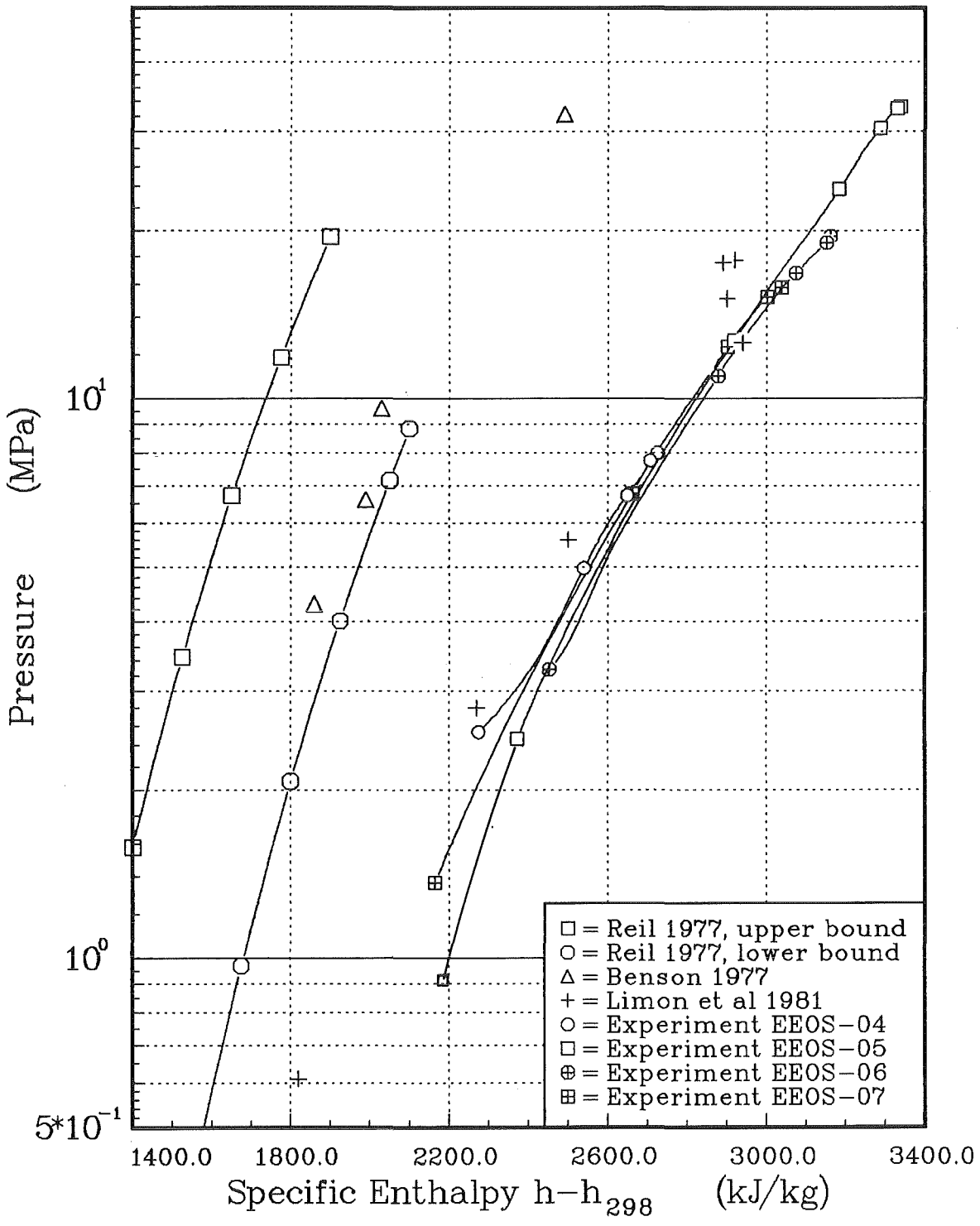

PLOT 1 09.06.11 TUES 5 FEB, 1985 JOB-INR85803, KFK DISSPLA 9.2

FIGURE VII.4

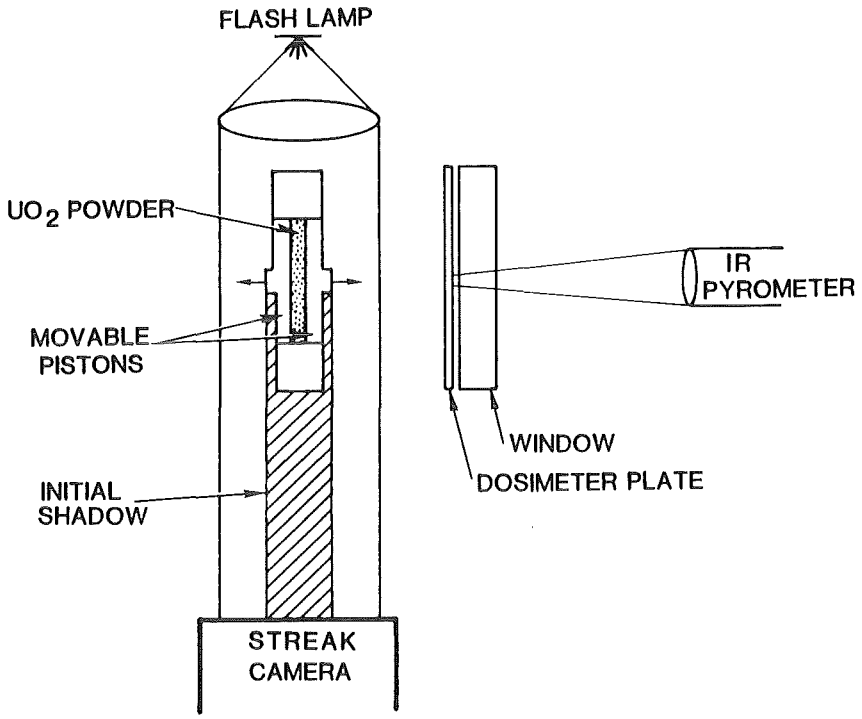

FIGURE VII.5 Electron Beam Heating Technique to Measure the Vapor Pressure of Uranium Oxide.

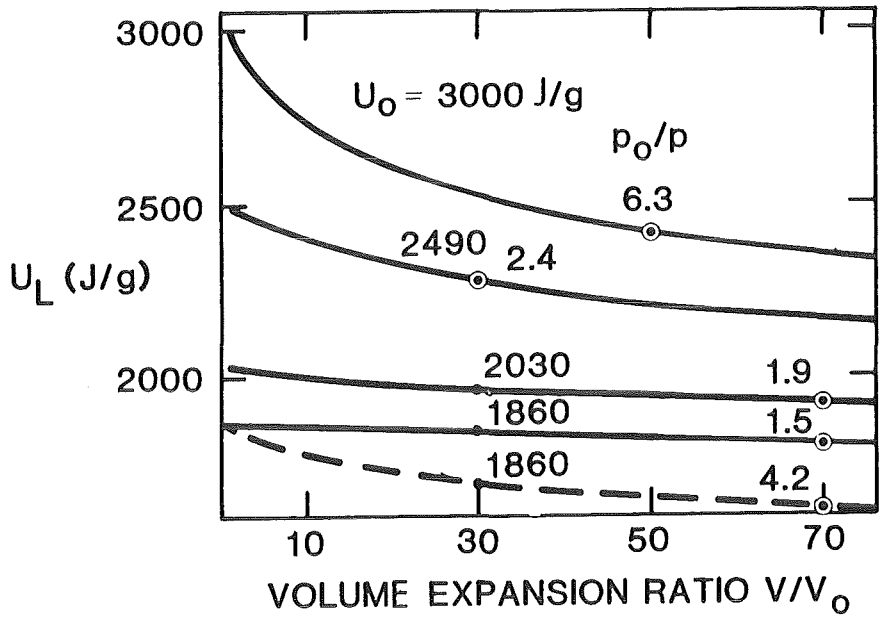

FIGURE VII.6 Calculated Internal Energy Decrease of Electron Heated Uranium Oxide Sample During Expansion of Container Volume for Various Initial Energy Depositions U_o.

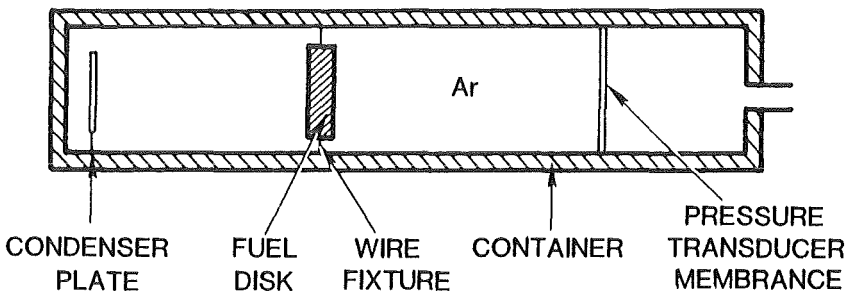

FIGURE VII.7 Pressure Cell of the CEA Fission Technique

Heat Capacity of Liquid UO2 And Gaseous U–O Molecules

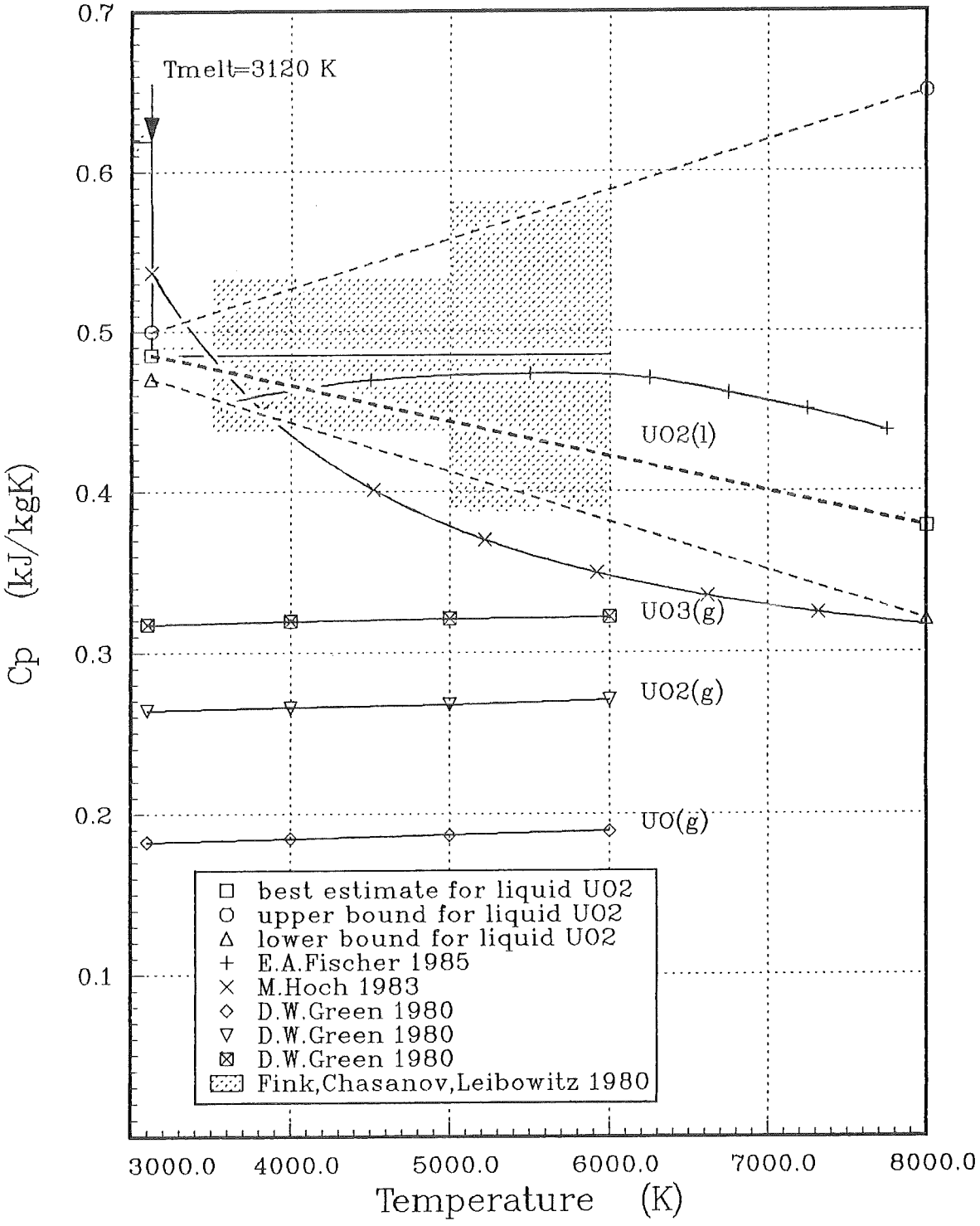

FIGURE VII.8

EEOS–Results in p–1/T–Format

Influence of Specific Heat

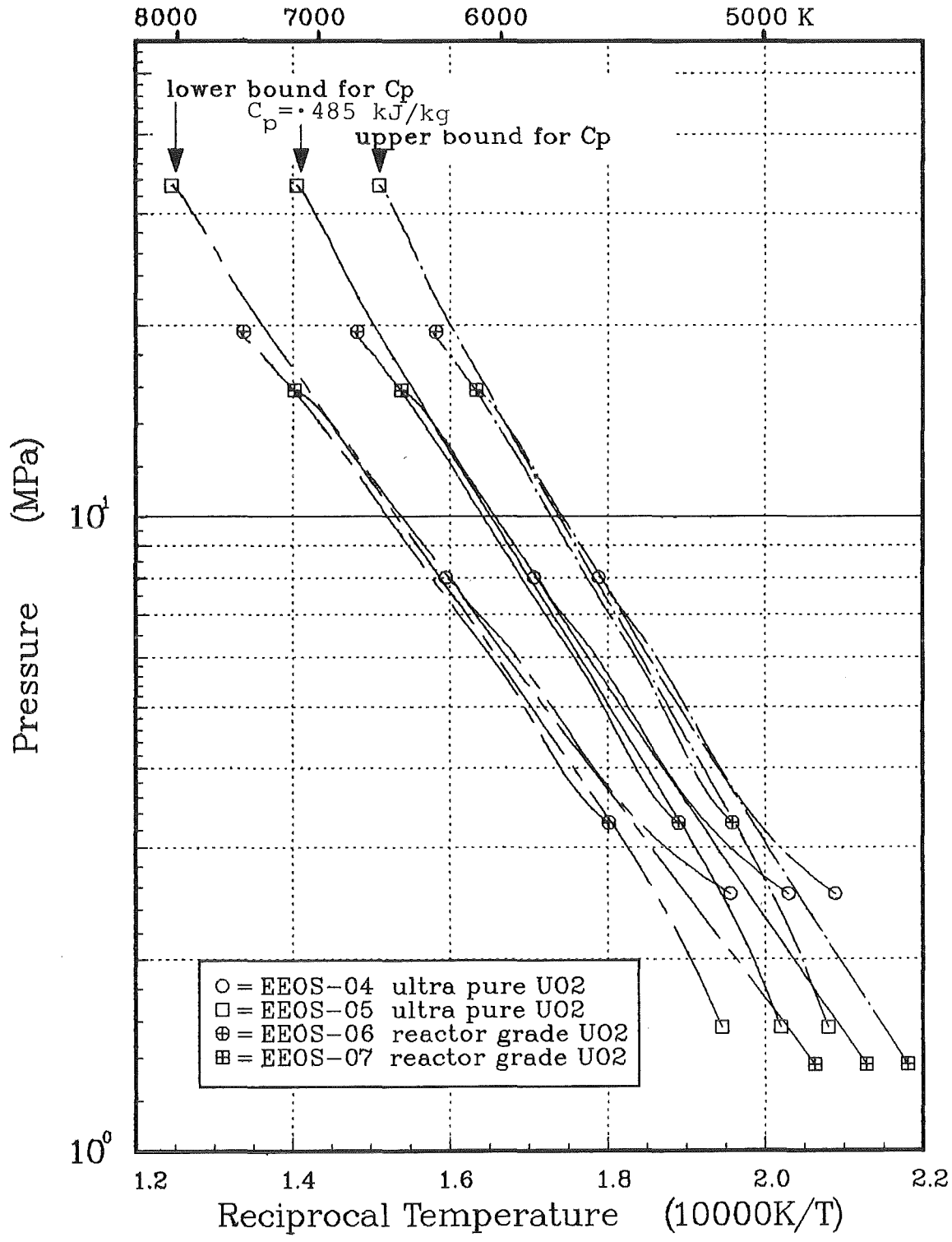

FIGURE VII.9

Pressure–Temperature Measurements

Liquid Uranium Oxide

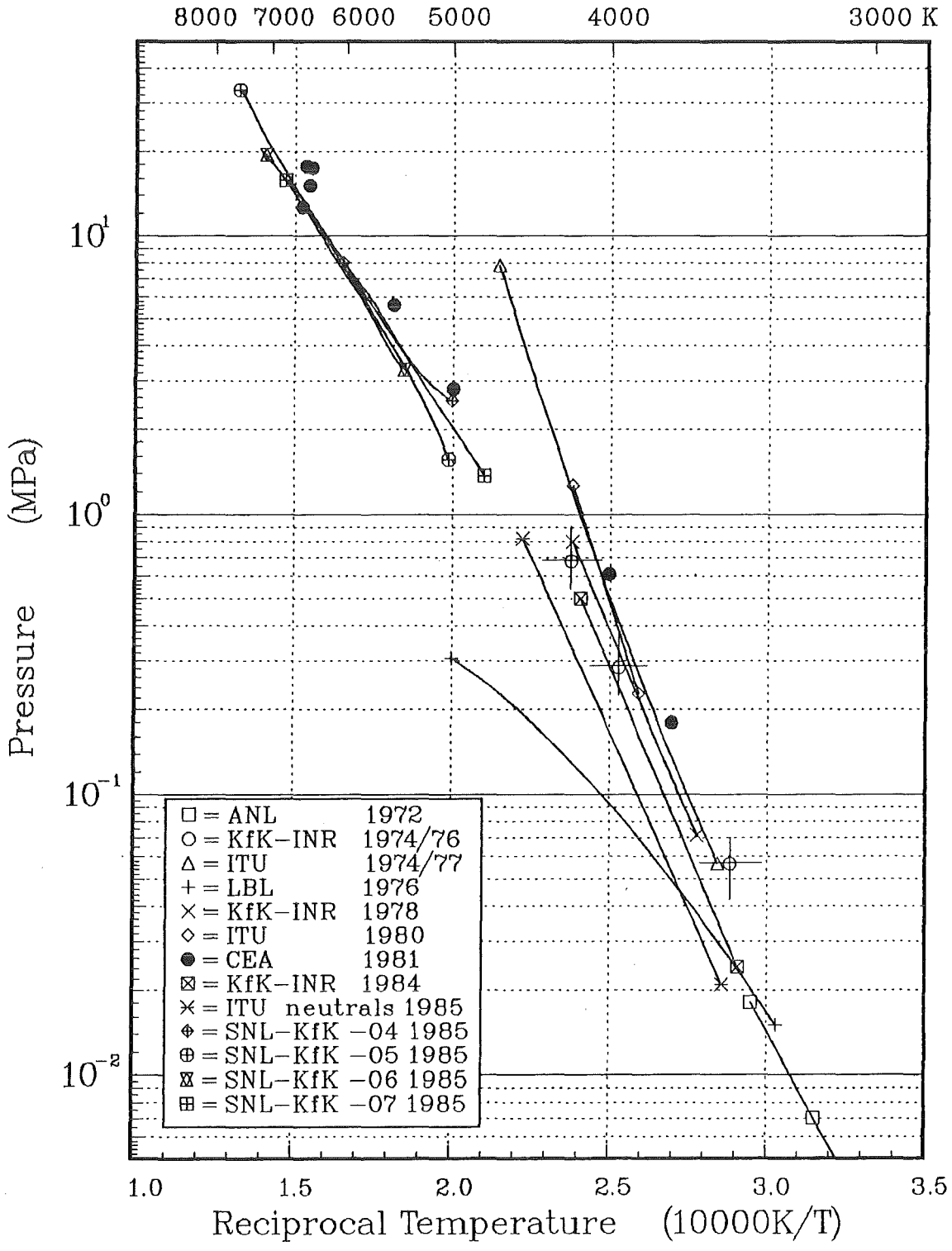

FIGURE VII.10

PLOT 1 11.41.02 TUES 26 MAR, 1985 JOB=INR858R2, KFK DISSPLA 9.2

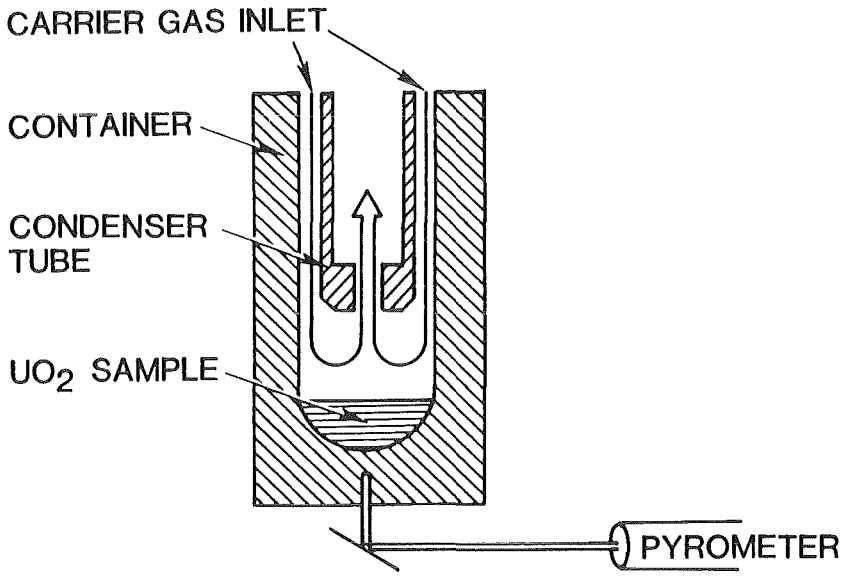

FIGURE VII.11 ANL Transpiration Technique

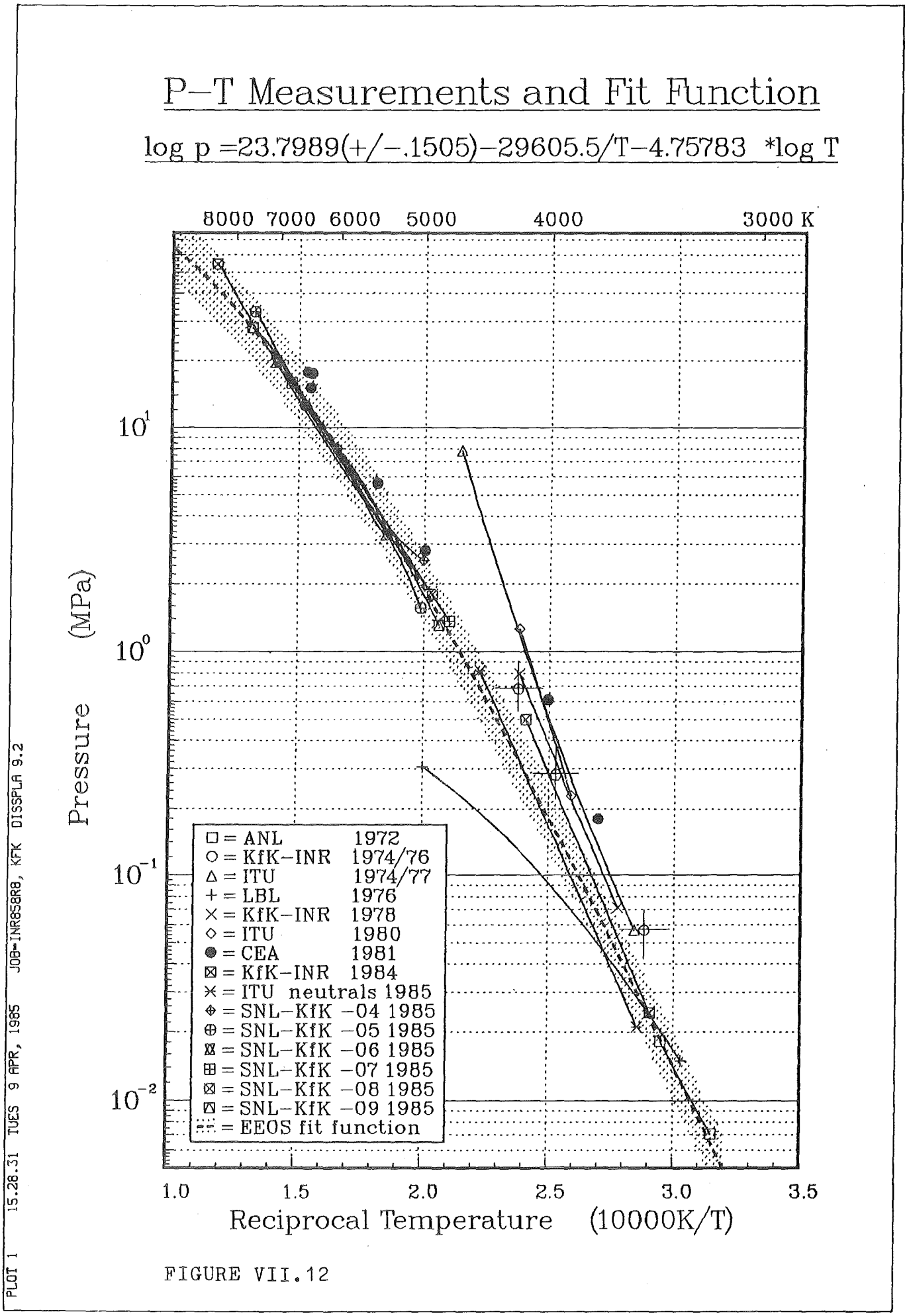

FIGURE VII.12

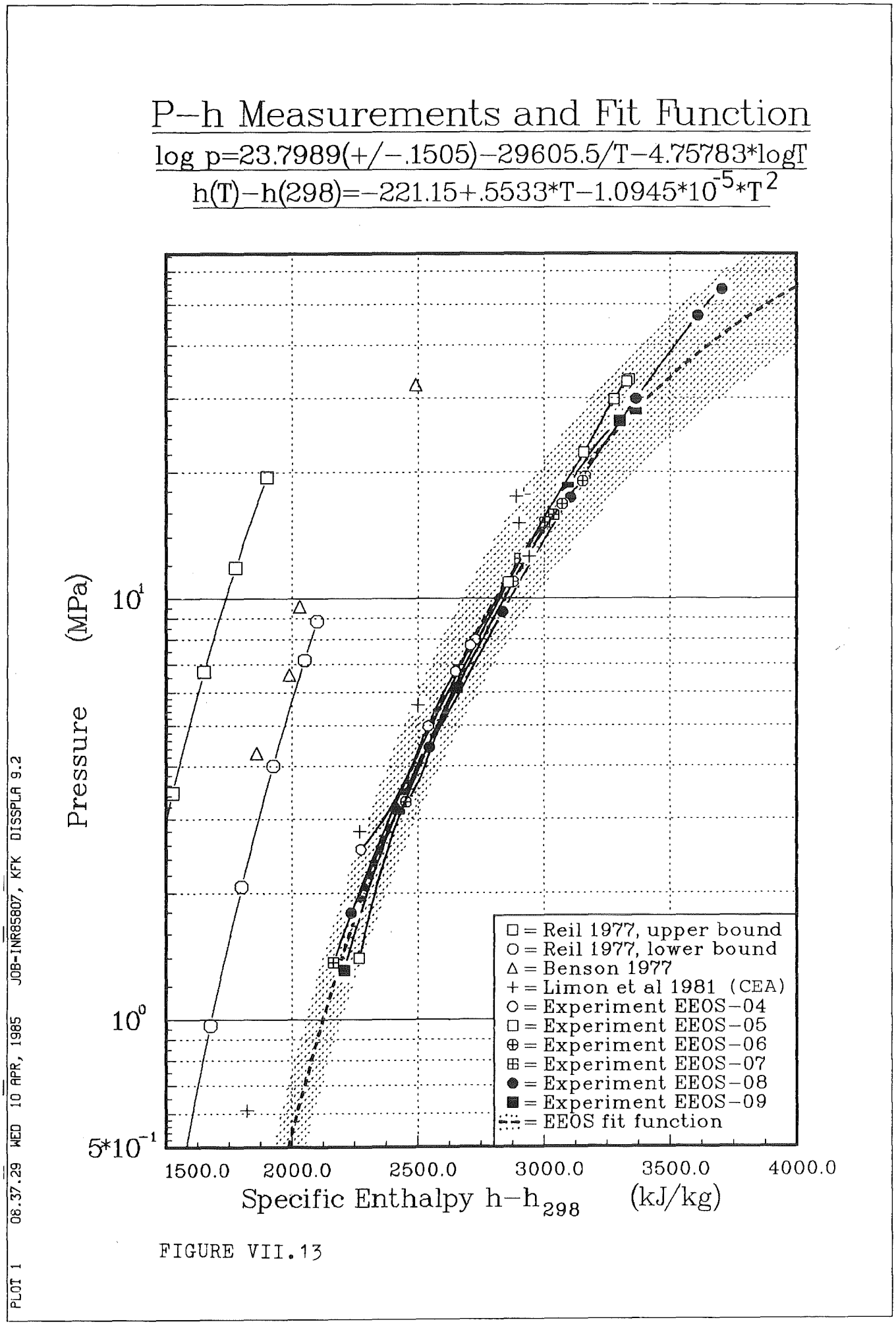

FIGURE VII.13

VIII. SUMMARY

1. The saturation vapor pressure of ultra-pure UO_2, reactor-grade UO_2 and reactor-grade $(U_{.77}\ Pu_{.23})O_2$ were investigated using newly developed in-pile heating techniques.

2. Emphasis was put on the precise determination of fuel enthalpy. Through the use of optimized cadmium filters, an in-pile calorimeter, and gamma counting techniques the remaining enthalpy uncertainty could be limited to about $\pm$ 3%.

3. To avoid contamination of the fuel sample or the fuel crucible during test preparation, appropriate cleaning procedures and facilities were designed for the EEOS experiments.

4. An analysis code called REAP (Reactor Energy Analysis Program) was written to evaluate measured raw data and to model energy transfer processes in the pressure cell and the calorimeter.

5. For the six experiments EEOS-04 to EEOS-09 examples of measured signals, results of the data analysis, and a discussion of special events were presented.

   For enthalpies between 2150 and 3700 kJ/kg, which corresponds roughly to 4700 and 8500 K, the measured vapor pressures varied from 1.3 to 54 MPa.

6. No difference could be detected in the vapor pressure curve of all three fuel types, suggesting the following conclusions:
   - Typical fabrication impurities of reactor oxide fuels, like e.g. carbon, do not contribute noticeably to the vapor pressure of pure UO_2. Apparently most of the gaseous impurities remain dissolved in liquid fuel and do not separate into the vapor space within about 10 milliseconds.

- Typical LMFBR mixed (U,Pu) oxides have the same saturation vapor pressure as UO_2 within the experimental uncertainties. Hence the extensive vapor pressure data base of UO_2 should be applicable to (U,Pu)-oxide fuels also.

7. The EEOS results for the pressure-enthalpy saturation curve were compared to earlier p-h measurements. Despite the rather large scatter in the data, the assessment provided evidence that the p-h saturation curve should be located in the vicinity of the EEOS results and the high-enthalpy CEA data points.

8. Using an estimate for the heat capacity of liquid UO_2, the EEOS and CEA p-h results were converted to pressure-temperature points. Comparison with the existing p-T measurements revealed the following:
   - The slope of the saturation curve in the log p-1/T representation, which is related to the heat of vaporization of liquid UO_2, is very similar for all three measurement techniques in which presumably true vapor/liquid equilibrium existed during the measurements (EEOS and CEA in-pile tests above 5000 K, ANL transpiration data below 3500 K).
   - The pressure curves from laser induced vaporization experiments, which cover the intermediate temperature range from 3500 to 5000 K, have slopes which are all (except one) noticeably higher than that of the equilibrium tests. This, together with recent experimental investigations on laser induced vaporization, suggests that the material removal processes under laser bombardment may differ from thermal equilibrium evaporation. The latter process governs fuel vaporization in Core Disruptive Accidents.
   - Of the various laser techniques, the boiling point method /VII.17/ appears to yield the pressure data which are most closely related to saturation vapor pressures.

9. The assessment of the pressure-temperature data showed that a functional fit, including a factor-of-2 uncertainty band, can be proposed for the p-T saturation vapor pressure curve of UO_2. This band covers the transpiration results up to 3500 K, the laser boiling point data up to 4200 K, and the in-pile measurements above 5000 K.

10. A temperature-enthalpy relation is presented which allows conversion of the p-T saturation curve to the corresponding p-h saturation curve. The p-h curve is also in good agreement with the EEOS and the high-enthalpy CEA data points.

11. The given equations represent the first proposal for a consistent description of measured p_{sat}-h as well as p_{sat}-T data of liquid UO_2. The relations cover the whole range of interest and are sufficiently precise for CDA analysis purposes.

12. Because no differences were detected in the saturation vapor pressure of UO_2 and $(U_{.77}\ Pu_{.23})O_2$ in the EEOS tests, the same p-h and p-T saturation lines are also proposed for typical LMFBR mixed oxide fuels.

13. No indications for critical point phenomena were observed over the investigated temperature range (about 4700 to 8500 K).

REFERENCES

Chapter I

I.1 Jackson, J.F., et al., "An Assessment of the Equation of State in the VENUS-II Disassembly Code", Report ANL/RAS 75-43 (November 1975), Argonne National Laboratory, USA.

I.2 Refling, J.G., Reynolds, A.B., Garner, P.L., Rao, S.P., "Nonequilibrium Evaporation And Condensation In Liquid-Metal Fast Breeder Reactor Fuel Expansion", Nuclear Technology 33(1977) 275

I.3 Breitung, W., "Vapor Pressures of Oxide Reactor Fuels Above 3000 K: Review and Perspective", SAND81-1383 (1981), Sandia National Laboratories, Albuquerque, NM, 87185, USA, also Report KfK-3276 (1982) Nucl. Res. Center Karlsruhe, FRG.

I.4 Ostensen, R.W., "A Sensitivity Study on the Damage Potential of a Liquid-Metal Fast Breeder Reactor Core Disassembly Nuclear Technology, 43 (1979) 301.

I.5 Buttery, N.E., "The Sensitivity of Excursion Yields to UO_2 Equation of State Unvertainties", Report RD/B/N4623 (1980) Central Electricity Generating Board, Res. Div., Berkely Nuclear Laboratories, Great Britain.

I.6 Nicholson, R.B., and Jackson, J.F., "A Sensitivity Study for Fast-Reactor Disassembly Calculations", Report ANL-7952 (1974), Argonne National Laboratory, USA.

I.7 Bott, T.F., and Jackson, J.F., "The Influence of Equation-of-State Uncertainties on Fuel Vapor Expansion Work-Energy Calculations", Trans. Amer. Nucl. Sci., 26 (1977) 367.

I.8 Carter, J.L., and Meyer, J.F., "The Vapor Pressure Equation-of-State in Core Disassembly Calculations", Trans. Amer. Nucl. Soc. 26 (1977) 368.

I.9 Buttery, N.E., Edwards, A.G., MacInnes, D.A., Findlay, J.R., Wood, M.H. and McTaggert, M.H., "Studies of the Effects of Fuel EOS Uncertainties on FBR Disassembly Energetics", Report SRD R 166 (1979), Safety and Reliability Directorate, UKAEA, Great Britain.

Chapter II

II.1 Reil, K.O., "Effective Equation of State Measurements on Uranium Dioxide" Dissertation, University of New Mexico, Albuquerque, NM, USA (May 1977).

II.2 Murata, K.K. Unpublished Report, Sandia Nat. Laboratories, (Jan. 1981).

II.3 Breitung, W., Gorham-Bergeron,E., Murata, K.K., "Analysis of Sandia In-Pile EOS Experiments", In Proc. Int. Meeting on Fast Reactor Safety Technology, Seattle, Washington, USA, August 19-23, 1979, p.1059.

II.4 Breitung, W., "In-Pile Calorimeter In The Joint SANDIA/KfK Equation-of-State Experiments on Nuclear Fuels", Report SAND80-2575, Sandia Nat. Laboratories, Albuquerque, NM 87185, USA (Febr. 1981).

II.5 Boldt, K.R., Schmidt, T.R., Estes, B.F., Reuscher, J.A., "Sandia Annular Core Research Reactor (ACRR). Safety Analysis Report", Report SAND-77-0208, Sandia Nat. Laboratories, Albuquerque, NM 87185, USA (Nov. 1981).

Chapter III

III.1 Breitung, W., Unpublished Report, Sandia Nat. Laboratories, Albuquerque, NM 87185, USA (Sept. 1980).

III.2 Clark, R.N., "Introduction to Automatic Control Systems", John Wiley and Sons Inc., New York, 1966.

III.3 Young, M.F., personal communication, Sandia Nat. Laboratories, Albuquerque, NM 87185, USA (Sept. 1980).

III.4 Murata, K.K. personal communication, Sandia Nat. Laboratories, Albuquerque, NM 87185, USA (Jan. 1980).

III.5 Herter, P., Unpublished Report, Sandia Nat. Laboratories, Albuquerque, NM 87185, USA (May 1982).

III.6 Reil, K.O., Breitung, W., Murata, K.K., "Total Vapor Pressure Measurements on Nuclear Fuels Using Fission Heating", In Proc. 8th Symp. on Thermophys. Prop., Nat. Bureau of Standards, Gaithersburg, MD, USA, June 15-18, 1981.

III.7 McKeon, D., personal communication, Sandia Nat. Laboratories, Albuquerque, NM 87185, USA (Sept. 1982)

Chapter IV

IV.1 Breitung, W., "Contamination Control in SANDIA Equation-of-State Experiments ", Report SAND80-1277 (Oct. 1980), Sandia Nat. Laboratories, Albuquerque, NM 87185, USA.

Chapter V

V.1 Sitharamayya, S., Subba Raju, K., "Heat Transfer Between an Axisymmetric Jet and A Plate Held Normal To The Flow", Canadian Journal of Chemical Engineering 47 (1969)365

Chapter VII

VII.1 Murata, K.K., private communication, Sandia Nat. Laboratories, Albuquerque, NM 87185, USA (1980)

VII.2 Benson, D.A., "Application of Pulsed Electron Beam Vaporization to Studies of UO_2", SAND77-0429, Sandia Nat. Laboratories, Albuquerque, NM 87185, USA (1977).

VII.3 Browning, P., Gillan, M.J., Potter, P.E., "The Equation of State of Uranium Dioxide: A Comparison of the Corresponding States and Significant Structures Theories", UKAEA Report AERE-R-8129 (1977)

VII.4 Limon, R., Sutren, G., Combette, P., Barbry, F., "Equation of State of Non Irradiated UO_2", in Proc. ANS/ENS Topical Meeting on Reactor Safety Aspects of Fuel Behavior, Sun Valley, Idaho, USA, August 2-6, 1981. CEA-CONF-5816

VII.5 Fink, J.K., Chasanov, M.G., Leibowitz, L., "Thermodynamic Properties of Uranium Dioxide", Report ANL-CEN-RSD-80-3 (April 81), Argonne Nat. Laboratory, Argonne, Ill., USA

VII.6 Fischer, E.A., private communication, Nucl. Research Center Karlsruhe, West Germany (1985).

VII.7 Hoch, M., "The Specific Heat of Refractory Metals And Oxides in The Solid And Liquid State", High Temp. High Press. 15 (1983) 165.

VII.8 Green, D.W., "Calculation Of The Thermodynamic Properties Of Fuel-Vapor Species From Spectroscopic Data", Report ANL-CEN-RSD-80-2 (Sept. 1980) Argonne Nat. Laboratory, Argonne, Ill., USA

VII.9 Reedy, G.T., Chasanov, M.G., "Total Pressure of Uranium-Bearing Species over Molten Urania", J. Nucl. Mat. 42 (1972) 341.

VII.10 Bober, M., Karow, H.U., and Schretzmann, K., "Evaporation Experiments to Determine the Vapor Pressure of UO_2 Fuel (3000-5000 K)", Thermodynam. of Nucl. Materials 1974, Vol. I. 295; IAEA Vienna (1975); also Nucl. Technology, 26 (1975) 237.

VII.11 Bober, M., Breitung, W., Karow, H.U., and Schretzmann, K., "Evaporation Studies of Liquid Oxide Fuel at Very High Temperatures Using Laser Beam Heating", Report KfK-2366, (1976), Karlsruhe Nuclear Research Center (KfK), FRG.

VII.12 Ohse, R.W., Berrie, P.G., Bogensberger, H.G., and Fischer, E.A., "Contribution of Uranium Plutonium Oxide Pressure, and Influence of Radial Fission Product Distributions on Pin Failure of Fast Breeder Fuels Under Accident Conditions", Thermodyn. of Nucl. Materials 1974, Vol. I, 307, IAEA, Vienna (1975).

VII.13 Babelot, J.F., Brumme, G.D., Kinsman, P.R. and Ohse, R.W., "Vapor Pressure Measurement over Liquid UO_2 and $(U,Pu)O_2$ by Laser Surface Heating Up to 5000 K", Atomwirtschaft-Atomtechnik 12 (1977) 387.

VII.14 Tsai, H.C., Covington, A., and Olander, D.R., "Laser Vaporization of UO_2", Report LBL-6016, Materials and Molecular Research Division Annual Report 1976, Lawrence Berkeley Laboratory, University of California, Berkeley, CA.

VII.15 Bober, M., Breitung, W., and Karow, H.U., "Thermodynamic Calculation and Experimental Determination of the Equation of State of Oxide Fuels up to 5000 K", Report KfK-2689 (1978), Karlsruhe Nuclear Research Center (KfK), FRG.

VII.16 Ohse, R.W., Babelot, J.F., Frezzotti, A., Long, K.A., and Magill, J., "Equation of State of Uranium Oxide: Mach Disk Investigation of Transient Laser Induced UO_2 Vaporization Up to 5000 K", High Temperatures-High Pressures 12 (1980), 537.

VII.17 Bober, M., Trapp, M., Unpublished Report 1984, (to be published 1985) Nuclear Research Center Karlsruhe, West Germany.

VII.18 Ohse, R.W., Babelot, J.-F., Cercignani, C., Hiernaut, J.-P., Hoch, M., Hyland, G.J., and Magill, J., "Equation Of State of Uranium Oxide", J. Nucl. Mat. 130 (1985) 165.

VII.19 Breitung, W., "Vapor Pressure of Liquid Uranium Oxide: A Review", Proc. 8th Symp. on Thermophys. Properties National Bureau of Standards, Gaithersburg, Maryland, USA (June 15-18, 1981).

VII.20 Bober, M. and Singer, J., "High Temperature Vapor Pressures of Stainless Steel Type 1.4970 And of Some Other Pure Metals From Laser Evaporation", Report KfK-3772 (1984), Karlsruhe Nuclear Research Center (KfK), FRG, to be published in High Temp. Science 19 (1985).

VII.21 Olstad, R.A. and Olander, D.R., "Evaporation of Solids By Laser Pulses, I.Iron", J. Appl. Phys. Vol.46 (1975) 1499.

VII.22 International Working Group on Fast Reactors, Specialists' Meeting on "Equation of State of Materials of Relevance to the Analysis of Hypothetical Fast Breeder Reactor Accidents," AERE Harwell, U.K., June 1978, Report IWGFR/26, IAEA, Vienna.

ACKNOWLEDGEMENTS

The authors are grateful to J. Garcia, SNL, for his help in the experiment preparation and performance, to P. Herter, CEA France, for providing the energy deposition code PATH, to D.C. Mc Keon, SNL, for providing the Monte Carlo code PABST, to C.W. Tucker, SNL, for assistance in the design of EEOS hardware, and to D.W. Vehar, SNL, for performing the fission product inventory analysis.

The authors further acknowledge the provision of funds and continuing interest in the program by the management at KfK (G. Heusener and G. Keßler), at NRC (R.W. Wright), and at SNL (P.S. Pickard, W.J. Camp, and J.V. Walker).